UNIVERSITY OF CALIFORNIA, SAN DIEGO

Synchrotron X-ray Scattering Studies of Rapidly Evolving Nanoscale Interfacial Systems

A dissertation submitted in partial satisfaction of the
requirements for the degree
Doctor of Philosophy

in

Physics

by

Yeling Dai

Committee in charge:

Professor Oleg Shpyrko, Chair
Professor Olga Dudko
Professor Eric Fullerton
Professor Shirley Meng
Professor Sunil Sinha

2013

The dissertation of Yeling Dai is approved, and it is acceptable in quality and form for publication on microfilm and electronically:

_____

_____

_____

_____

_____
Chair

University of California, San Diego

2013

TABLE OF CONTENTS

LIST OF FIGURES

ACKNOWLEDGEMENTS

First of all, I would like to express my sincere gratitude to my thesis advisor, Professor Oleg Shpyrko, for his encouraging and inspiring guidance, infinite patience and constant support during these past years. Oleg has provided me an excellent example as a successful young physicist and advisor. He gave me the freedom to pursue whatever I wanted to try as well as the insightful suggestions and encouragements. I hope I will be as passionate, optimistic and energetic as he is. I also gratefully acknowledge the members of my Ph.D. committee, Professor Sunil Sinha, Professor Olga Dudko, Professor Eric Fullerton and Professor Shirley Meng, for their time, support, valuable feedback and helpful advice in general.

This work is done in collaboration with many people. I thank all of those who have helped me and contributed to this work. Thanks to the Surface Scattering Group at Center for Advanced Radiation Sources (CARS), University of Chicago, especially Binhua Lin and Mati Meron. Besides her constant help and guidance, Binhua has been taking good care of me as a mentor, a friend and an "adoptive mom". Mati has been very helpful in providing scientific, technical supports and a lot of funny stories about the science. I will still believe that there is nothing Mati cannot do with IDL. I am very grateful to Kyle Alvine for fruitful collaborations. We worked together at the beamline and he taught me much at the time I just started my research with x-ray scattering. I would like to acknowledge the contribution from the beamline support at APS, sector 8-ID. Without the help from Alec Sandy, Suresh Narayanan and Zhang Jiang our experiments were impossible to complete. My thanks also go to the Electronics Materials Group at NIST, especially the group leader Christopher Soles, for important contributions and insightful discussions.

I thank all the former and present members of the Shpyrko Group. They are so helpful and friendly, making this group like a big family. I particularly want to thank my fellow students Jacob Stanley and Leandra Boucheron for their companionship and help, as well as useful discussions. They have spent days and nights together with me working at the beamlines and really brought a lot of fun to the work.

I gratefully acknowledge the funding sources that made my Ph.D. work possible. I was funded by NSF CAREER Award Grant 0956131. Most of the work was conducted on Sector 8-ID and Sector 15-ID at the Advanced Photon Source (APS), Argonne National Laboratory. The Advanced Photon Source is supported by the U.S. Department of Energy, Basic Energy Sciences, Office of Science, under Contract No. W-31-109-Eng-38.

I owe a big and deep thank you to my English tutor, Michael Miles, for his generous help and teaching. Mike began tutoring me in language, as a volunteer, the first month I came to the USA. In the past seven years, we have met weekly. In addition to correcting and perfecting my English, Mike introduced me the traditions and cultures of this country, shared with me his opinions and experiences, and listened to my thoughts and stories. He indeed made my life in the USA more colorful and enjoyable.

I will forever be thankful to my family for their endless love and unconditional support. I can never express enough thanks to my dear, supportive, patient husband San-wen Chen, who has been with me these years and made them the best years of my life.

The text of Chapter 3, in part, is a reprint of the material as it appears in:

Y. Dai, K. J. Alvine, H. Ro, C. L. Soles, S. Narayanan, A. R. Sandy and O. G. Shpyrko, "Capillary Wave Dynamics of Laterally Confined Liquid Polystyrene Films", in preparation,(2013).

The text of Chapter 4, in full, is a reprint of the material as it appears in:

K. J. Alvine, Y. Dai, H. Ro, C. L. Soles, S. Narayanan, A. R. Sandy and O. G. Shpyrko, "Capillary wave dynamics of thin polymer films over submerged nanostructures", *Phys. Rev. Lett.*, 109, 2012. Copyright(2012) by the American Physical Society.

The text of Chapter 5, in part, is a reprint of the material as it appears in:

Y. Dai, K. J. Alvine, H. Ro, C. L. Soles, J. Strzalka, O.G. Shpyrko, "De-

velopment of a Zig-Zag Capillary Instability in Nanoimprinted Polymer Gratings: A Time-Resolved GISAXS Study", in preparation,(2013).

The text of Chapter 6, in full, is a reprint of the material as it appears in: Y. Dai, B. Lin, M. Meron, K. Kim, B. D. Leahy and O. G. Shpyrko, "A comparative study of Langmuir Surfactant Films: Grazing Incidence X-ray Off-Specular Scattering vs. X-ray Specular Reflectivity", *J. Appl. Phys.*, 110, 2011. Copyright(2011) by the American Institute of Physics.

The text of Chapter 7, in part, is a reprint of the material as it appears in: Y. Dai, B. Lin, M. Meron, K. Kim, B. D. Leahy and O. G. Shpyrko, "Synchrotron X-ray studies of Rapidly Evolving Morphology of Self-assembled Nanoparticle Films under Lateral Compression", submitted to *Langmuir*, 2013. Copyright(2013) by the American Chemical Society.

VITA

2006	B. S. in Physics, University of Science and Technology of China, Hefei, China
2008	M. S. in Physics, University of California, San Diego
2008	National School on Neutron and X-ray Scattering, Argonne National Laboratory, Chicago, Illinois
2013	Ph. D. in Physics, University of California, San Diego

PUBLICATIONS

Y. Dai, K. J. Alvine, H. Ro, C. L. Soles, J. Strzalka, O.G. Shpyrko, "Development of a Zig-Zag Capillary Instability in Nanoimprinted Polymer Gratings: A Time-Resolved GISAXS Study", in preparation.

Y. Dai, K. J. Alvine, H. Ro, C. L. Soles, S. Narayanan, A. R. Sandy and O. G. Shpyrko, "Capillary Wave Dynamics of Laterally Confined Liquid Polystyrene Films", in preparation

Y. Dai, B. Lin, M. Meron, K. Kim, B. D. Leahy and O. G. Shpyrko, "Synchrotron X-ray studies of Rapidly Evolving Morphology of Self-assembled Nanoparticle Films under Lateral Compression", submitted to *Langmuir*, 2013.

K. J. Alvine, Y. Dai, H. Ro, C. L. Soles, S. Narayanan, A. R. Sandy and O. G. Shpyrko, "Capillary wave dynamics of thin polymer films over submerged nanostructures", *Phys. Rev. Lett.*, 109, 2012.

Y. Dai, B. Lin, M. Meron, K. Kim, B. D. Leahy and O. G. Shpyrko, "A comparative study of Langmuir Surfactant Films: Grazing Incidence X-ray Off-Specular Scattering vs. X-ray Specular Reflectivity", *J. Appl. Phys.*, 110, 2011.

K. Kim, B. D. Leahy, Y. Dai, O. G. Shpyrko, J. S. Soltau, M. Pelton, M. Meron, B. Lin, "Governing Factors in Stress Response of Nanoparticle Films on Water Surface", *J. Appl. Phys.*, 110, 2011.

ABSTRACT OF THE DISSERTATION

Synchrotron X-ray Scattering Studies of Rapidly Evolving Nanoscale Interfacial Systems

by

Yeling Dai

Doctor of Philosophy in Physics

University of California, San Diego, 2013

Professor Oleg Shpyrko, Chair

In light of the development of third-generation synchrotron sources which deliver extremely bright radiation beam over a board energy band, tremendous progress has been made in x-ray science and the diverse range of disciplines that can be studied with x-ray. The special properties of synchrotron-produced x-ray such as coherence, polarization, etc., combined with different extreme experimental conditions, can meet almost any requirement of the research for material characterization, imaging, molecular dynamics, surface/interface physics and so on. In this work we will demonstrate how outstanding properties of synchrotron x-ray can be use to study the structural and dynamic properties of rapidly evolving nanoscale interfacial systems. A large part of this thesis is devoted to the investigation of

the surface capillary fluctuations of laterally confined supported polystyrene films using x-ray photon correlation spectroscopy (XPCS), a young coherent scattering technique that can probes the dynamics of matter. The structural evolution of interfacial/surface system, such as the self-assembled nanoparticle film at water-air interface and the nano-imprinted polystyrene pattern, can be studied by different time-resolved x-ray small angle scattering techniques in grazing incidence geometry (GISAXS,GIXOS,GID), as well as the conventional specular reflectivity (XR) measurement. Particularly in the case of the liquid surface research, special efforts have been made to improve a recently developed diffuse scattering technique Grazing incidence off-specular x-ray scattering (GIXOS) for probing the structure at liquid interface with much better temporal resolution compared with that of XR. In this work We will present all the experimental results together with conclusive data analysis from the studies of these evolving systems with x-ray scattering techniques. In comparison to the reciprocal space studies with x-ray scattering tools, part of this thesis is devoted to the experiments using real space probes such as optical microscope and Atomic force microscope (AFM).

1 Introduction

The structure and dynamics of liquid surfaces have been of great interest to both the experimental and theoretical communities since the pioneering work of van der Waals more than one century ago. In his simple version of the density functional theory [1], he considered a liquid-vapor interface as a finite region whose density smoothly changes from that of the liquid phase to that of the vapor phase. In the real world, even in the absence of externally induced vibrations, the liquid surfaces are never absolutely smooth, and the height of the surface always fluctuates in space and in time. Therefore, an alternative approach for describing a liquid surface proposed by Buff, Lovett, and Stillinger [2] treated the surface as a sharp step-like profile decorated with the thermal-induced height fluctuations, which are called thermally excited capillary waves [3].

The emergence of high-brilliance third-generation synchrotron radiation sources in recent years enables a direct investigation of the liquid surface properties. It turns out that the capillary wave model gives a very accurate description of the in-plane structures and also predicts the interfacial roughness much better than van der Waals's theory. These capillary wave dynamics of have been extensively studied for both bulk liquids and thin films and can be described by capillary and the hydrodynamic theories down to nanometer lengthscales.

This work describes how we applied x-ray surface techniques to study surface phenomena such as surface capillary fluctuation on laterally confined molten polymer film, the capillary instability of nano-imprinted polymer patterns, as well as the morphological evolution of self-assembled nano-particle Langmuir film under lateral compression.

This thesis is structured as follows: Chapter 2 includes a brief review of

the scientific background of various surface x-ray scattering techniques used in this work, such as x-ray reflectivity (XR), x-ray photon correlation spectroscopy (XPCS), and small angle scattering such as grazing incidence small angle x-ray scattering (GISAXS) and grazing incidence x-ray off-specular scattering (GIXOS), discussed in combination with the surface capillary theory. Chapter 3 presents the XPCS measurements of the capillary wave dynamics of thin molten polystyrene (PS) films confined laterally in Si grooves. The size dependence and the directional dependence of the confinement effects has been observed. Chapter 4 reviews the XPCS results of the capillary wave dynamics of thin molten PS films over submerged nanostructures. A cutoff length-scale in the dynamics perpendicular to the grooves, which links to the transition from standard over-damped capillary wave behavior to suppressed dynamics due to substrate interactions, was observed and interpreted. Chapter 5 covers the studies of the zig-zag capillary instability development in nano-imprinted polymer pattern using time-resolved GISAXS. Chapter 6 and 7 focus our new approach, GIXOS, for studying the self-assembled surfactant or nano-particle Langmiur films at liquid-air interfaces. Details about how we develop and validate the GIXOS analysis method are discussed. In Chapter 8, the main findings of this work are summarized, and possible prospective directions of future research extended from this work are briefly discussed.

Bibliography

[1] J. D. van der Waals. The thermodynamic theory of capillarity under the hypothesis of a continuous variation of density. *Journal of Statistical Physics*, 20(2):200–244, February 1979.

[2] F. P. Buff, R. A. Lovett, and F. H. Stillinger. Interfacial density profile for fluids in the critical region. *Physical Review Letters*, 15(15):621–623, October 1965.

[3] A. Braslau, P. S. Pershan, G. Swislow, B. M. Ocko, and J. Als-Nielsen. Capillary waves on the surface of simple liquids measured by x-ray reflectivity. *Physical Review A*, 38(5):2457–2470, 1988.

2 Principles of Surface X-ray Scattering

In this chapter, the principles of x-ray surface scattering will be reviewed. The story will begin with the properties of x-ray radiations and the interactions of x-ray photons with matter. Different x-ray scattering techniques will be covered and then we will discuss about how height-height correlation function enters the scattering cross section for describing diffuse scattering from the interfacial structures and how x-ray photon correlation spectroscope can be applied to study the thermal excited capillary fluctuations at liquid surfaces. Finally we will include some experimental details of x-ray experiments on liquid surfaces.

2.1 X-ray and X-ray's Interaction with Matter

Almost one century ago, x-ray was discovered by Wilhelm C. Röntgen. Since that time, X-ray has been established as an invaluable tool of probing the structure of matter. In the last several decades, the rapid development of synchrotron facilities started a new era in x-ray science and markedly increased the pace of innovation in x-ray research. As a result, more properties of x-ray have been exploited and tailored to meet the any requirement of the research for chemical and material science, physics and engineering, and more recent molecular and bio-science.

2.1.1 X-ray - Waves and Photons

X-rays are electromagnetic waves with wavelengths in the region of an Ångström (10^{-10} m) that match the atomic spacing therefore interact with both structure and dynamics of matter. From a quantum mechanical perspective, a monochromatic x-ray beam is viewed as a group of photons, each carrying energy and momentum and interacting with electrons in matter. The numerical relation [1] between wavelength λ in Å and photon energy E in kev is:

$$\lambda[\mathring{A}] = \frac{hc}{E} = \frac{12.398}{E[keV]} \tag{2.1}$$

2.1.2 Refractive Index and Critical Angle

One should expect refraction phenomena at interfaces between media since x-rays are electromagnetic waves. By definition, the refractive index for vacuum is one. In general for x-rays, the refractive index n is always slightly smaller than the unity and it can be expressed as:

$$n = 1 - \delta + i\beta \tag{2.2}$$

where δ and β is related to the scattering and absorption properties of the refracting medium, respectively. They are defined as:

$$\delta = \frac{r_e}{2\pi}\lambda^2 \sum_k \frac{Z_k + f'_k}{V_m} \tag{2.3}$$

and

$$\beta = \frac{r_e}{2\pi}\lambda^2 \sum_k \frac{f''_k}{V_m} = \frac{\lambda}{4\pi}\mu \tag{2.4}$$

where $r_e = 2.813 \times 10^{-5}\mathring{A}$ is the classical radius of the electron,Z_k is the number of electrons of atom k in the unit cell, V_m is the volume of the unit cell, f and f are the anomalous scattering coefficients, and μ is the absorption length. δ is of the order of 10^{-5} in solid materials and only 10^{-8} in the air, the imaginary part β is usually much smaller than δ. For example, the refractive index of 10keV x-ray in bulk gold is $\delta = 2.99 \times 10^{-5}$ and $\beta = 2.21 \times 10^{-6}$. The phase velocity of x-ray in the material is c/n.

Given the fact that n is smaller than unity, x-ray incident at the material surface from vacuum will be refracted towards the surface, therefore, when the incidence angle is below a certain incident grazing angle called the critical angle, α_c,x-ray will undergo total external reflection. The expression of the critical angle can be derived with Snell's law and approximated as:

$$\alpha_c \approx \sqrt{2\delta} \tag{2.5}$$

where for simplicity we have taken $\beta = 0$. With δ being typically around 10^{-5}, α_c is of the order of a milli-radian.

Total external reflection results much-reduced penetration of x-rays into the materials, which increases the surface sensitivity and allows the scattering from the near surface or near interface region to be studied. This makes x-ray a valuable tool for the investigations of surface and interface properties.

2.1.3 Scattering Cross-section and Born Approximation

To evaluate the scattering from matter, we start with a scattering event in which an x-ray beam of intensity I_0 photons per second is incident on a sample, then the number of photons, I_{sc} scattered per second into a detector mounted downstream that subtends a solid angle $\Delta\Omega$, will be proportional to $\Delta\Omega$, to I_0 and to N, where N is the number of particles in the sample per unit area. Most importantly it will depend on how efficiently the particles in the sample scatter x-ray, which can be quantitatively described with the differential cross section, $d\sigma \setminus d\Omega$. So that we can get:

$$I_{sc} = I_0 N \Delta\Omega \frac{d\sigma}{d\Omega} \tag{2.6}$$

Thus, as the meeting point of experiment and theory, the differential cross section is defined by:

$$\frac{d\sigma}{d\Omega} = \frac{\text{No. of X-ray photons scattered per second into } \Delta\Omega}{\text{Incident flux} \times \Delta\Omega} \tag{2.7}$$

Note that incident flux is given by $I_0 N$.

When the scattering is weak, where multiple scattering effects can be neglected for simplicity, the sample can be considered as only a perturbation on the incident radiation beam, therefore the Born approximation, also known as the kinematical approximation, is valid. Under the first order Born approximation, we can derive the expression of the differential cross section as:

$$\frac{d\sigma}{d\Omega} = {r_e}^2 \left| \int d\mathbf{r}\rho(\mathbf{r})e^{-i\mathbf{q}\cdot\mathbf{r}} \right|^2 \tag{2.8}$$

Where r is the location in the sample and q is the wave vector transfer, which is difined as the difference between the wave vectors of outgoing and incident beams. Therefore, the differential cross section is simply the square modulus of the Fourier transform of the electron density function $\rho(\mathbf{r})$. This formula provides a simple view about how x-ray interacts with matter and a clear relation between the scattered x-ray radiation and the measured sample structure in the form of the electron density distribution.

2.2 X-ray Scattering from Surface Structures

2.2.1 Structure of Liquid Surfaces

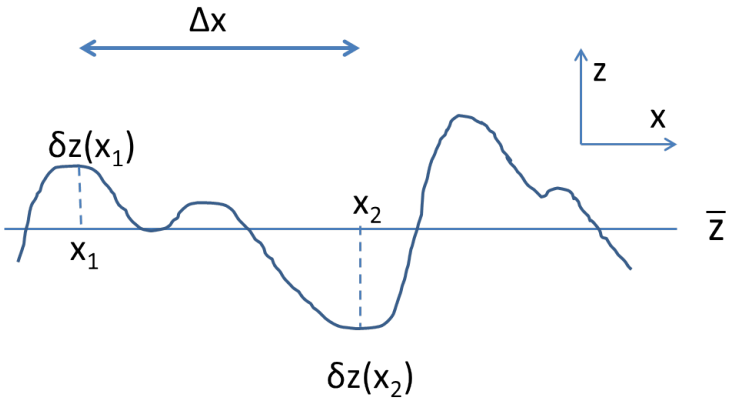

Figure 2.1: Schematic of a rough surface

Unlike the atomic-scale flat solid surface, liquid surfaces are subject to thermal excited capillary fluctuations, even in the absence of externally induced

vibrations. The surface height fluctuations can be described with a height contour function

$$z(\mathbf{r}_{||}) = \bar{z} + \delta z(\mathbf{r}_{||}) \tag{2.9}$$

where $\delta z(\mathbf{r}_{||})$ denotes the height variation at an in-plane position $r_{||}$ with respect to the averaged surface height $\bar{z} = \langle z(\mathbf{r}_{||})\rangle_{r_{||}}$, as shown in Figure 2.1.

2.2.2 Scattering from Liquid Surfaces

The height fluctuations of surface can be characterized by their statistical averages and, for the case of thermal excited capillary fluctuations, Sinha et al. [2] have shown that integration over these height fluctuations yields the following dependence of the scattering on the in-plane and surface-normal components of the wavevector transfer $q_{||}$ and q_z (scattering geometry shown in Fig 2.2):

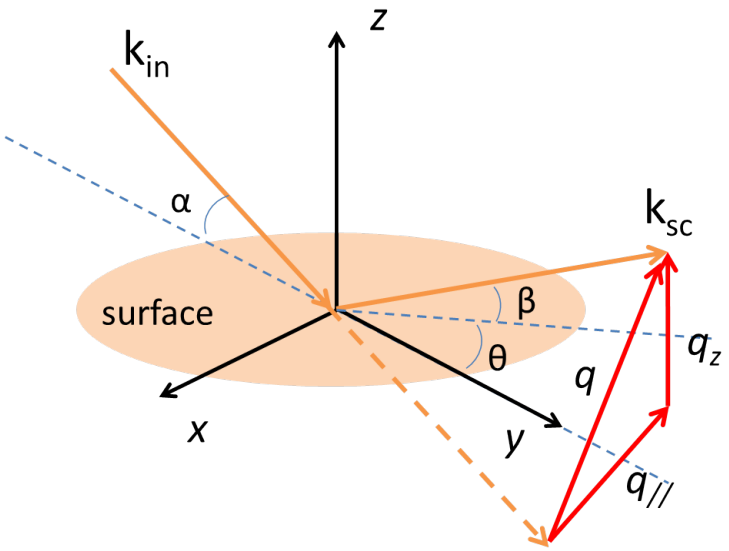

Figure 2.2: Schematic of scattering geometry

$$\int_{|\mathbf{r}_{||}|>a} d^2\mathbf{r}_{||} exp\{\frac{{q_z}^2}{2}\langle[z(\mathbf{r}_{||}) - z(0)]^2\rangle\} exp[i\mathbf{q}_{||}\cdot\mathbf{r}_{||}] = \frac{1}{{q_{max}}^{\eta}}\frac{4\pi^2}{{\mathbf{q}_{||}}^{2-\eta}} \tag{2.10}$$

where $\eta = \frac{k_B T}{2\pi\gamma}{q_z}^2$ is the capillary exponent and q_{max} is the upper wavevector cutoff related to atomic size a ($q_{max} = \pi/a$). Therefore equation 2.10 leads us to

the expression of the scattering differential cross-section: the intensity measured at a specific scattering vector $\mathbf{q}$ is obtained by integrating the differential cross-section over the solid angle $d\Omega$ defined by the detector acceptance of the measurement:

$$\frac{I}{I_0} = \frac{1}{A_0}\int_{res}\frac{d\sigma}{d\Omega}d\Omega = \frac{1}{k^2\sin\alpha\sin\beta}(\frac{q_c}{2q_z})^4\frac{\eta {q_z}^2}{8\pi}|\Phi(q_z)|^2|t^{in}|^2|t^{sc}|^2\int_{res}\frac{1}{{\mathbf{q}_{||}}^2}(\frac{\mathbf{q}_{||}}{q_{max}})^{\eta}d^2\mathbf{q}_{||} \tag{2.11}$$

where wavevector transfer $k = 2\pi/\lambda$, I_0 and A_0 are the intensity and the illumination area of the incident x-ray beam, α and β is the incident and scattering angle, q_c and q_{max} are the critical wavevector and upper wavevector cutoff, γ is the surface tension of the sample, while t^{in} and t^{sc} are the Fresnel transmission coefficient between air and water, t^{sc} is responsible for the low angle scattering peak (the so-called Yoneda peak). The structure factor $|\Phi(q_z)|^2$ is defined by the in-plane average of the intrinsic electron ρ density along the surface normal:

$$|\Phi(q_z)|^2 = \frac{1}{\rho_\infty}\int dz\frac{\rho(z)}{dz}exp(iq_z z) \tag{2.12}$$

One approach to analysis of x-ray surface scattering data is to not separate the capillary contributions from the specular reflection, producing effectively smeared out interfacial electron density profiles due to thermal capillary fluctuations. However, since the degree of the thermal roughening depends on the experimental resolution function, measurements on identical samples using different resolution settings are bound to produce different density profiles. If the effect of thermal capillary wave fluctuation is considered separately, as is done in this work, the resulting electron density profile is the intrinsic property of the sample, independent of experimental details such as detector resolution. The measured x-ray scattering intensity at a specific value of scattering wavevector transfer $\mathbf{q}$ is then proportional to the integration of differential cross-section over resolution function. The calculation of the experimental resolution effects will be discussed in Chapter 6.

2.3 X-ray Photon Correlation Spectroscope

The development of third generation synchrotron sources opened up the range of new possibilities in x-ray research and technology that have already produced very important results. The sufficient coherent flux facilitates the slow dynamics studies of various equilibrium and non-equlibrium process in condensed matter systems by a young techniques called x-ray photon correlation spectroscopy (XPCS).

2.3.1 Coherent Scattering - Speckles

When a coherent light is scattered off a rough surface, a speckle pattern is formed as a result of the interference between waves with same frequency but different phase and amplitude after being scattered by different parts of the surface. Therefore, the speckle pattern can provide unique information about the exact structure of the surface.

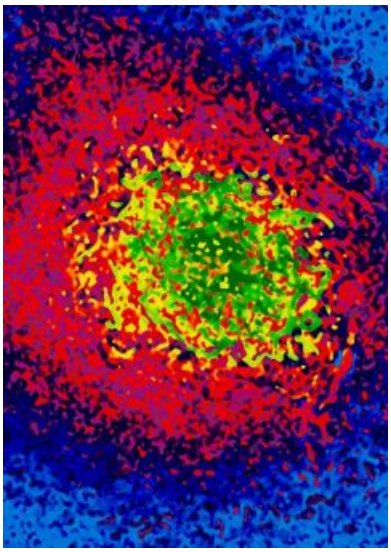

Figure 2.3: X-ray speckle pattern.(picture from Shpyrko group's webpage)

The coherent optical light has been available since the invention of laser in the 1960s and speckle related techniques such as dynamical light scattering (DLS) have been wildly applied to the studies of the particle diffusion in fluids within the

visible light regime. The first observation of x-ray speckles was reported by M. Sutton[3] in 1991. In the last decade, the development of the third generation synchrotron and the improvement of x-ray detection efficiency enabled the application of XPCS[4], the x-ray version of DLS technique.

2.3.2 X-ray Photon Correlation Spectroscopy

The XPCS technique bases on the fact that a particular arrangement of atoms/electrons in a material produces a characteristic "speckle" pattern when it scatters a coherent x-ray beam. If the atomic arrangement changes with time, the speckles would also change accordingly, thus by studying the time dependence of the changes in speckle pattern, one can probe the atomic dynamics at various wave vector transfer, corresponding to different length scales.

In a typical XPCS experiment, speckle patterns are recorded with an x-ray area detector at a constant time interval Δt as the sample undergoes dynamics. Then the normalized intensity-intensity time auto-correlation function is calculated as:

$$g_2(q_{||}, \tau) = \frac{\langle I(q_{||}, t) I(q_{||}, t+\tau) \rangle}{\langle I(q_{||}, t) \rangle^2} \tag{2.13}$$

where $I(q_{||}, t)$ is the scattering intensity at in-plane wave vector transfer $q_{||}$ at time t, τ is the delay time. The angular brackets denotes the averages over time t. For a specific $q_{||}$, the value of $g_2(q_{||}, \tau)$ decays as the time delay τ increasing. The g_2 function can be fitted to a single- exponential decay function as:

$$g_2(\tau) = 1 + \beta exp(-2\tau/\tau_0) \tag{2.14}$$

Where the fitting parameter β is the speckle contract and τ_0 gives the relaxation time constant. By fitting the auto-correlation function $g_2(\tau)$ to a single-exponential decay function, one can extract the relaxation time constant of the measured dynamics. This procedure has been discussed in details in Ref [4, 5].

2.4 Experimental Details

Several practical considerations about the experiments will be discussed in this section.

2.4.1 Synchrotron Radiation Sources

Synchrotron radiation is having a great impact on many area of science ranging from condensed matter physics, chemistry, biology, material science and so on, and has been tremendously successful with the arrival of third generation synchrotron photon sources [6]. Even though the new x-ray Free Electron Laser (FEL) is currently under construction and will bring us further into the future, the 3rd generation shycrontron sources are mainly serving x-ray research of the inter-disciplinary science. To date there are more than twenty 3rd generation synchrotron radiation facilities operating over the world. Among them, the Advanced Photon Source (APS) [7], shown in Fig 2.4 at Argonne National Laboratory provides the most brightest storage ring-generated x-ray beams in the western hemisphere for research in almost all the scientific disciplines.

The experiments discussed in this work were carried on at APS beamline 8-ID-I and 15-ID-C,since the dynamics studies of surface capillary fluctuations require coherent monochromatic radiations and studying liquids requires liquid surface spectrometer.

2.4.2 Grazing Incidence Scattering

When the x-ray incident angle α is near or below the critical angle α_c for total external reflection, the incident x-ray beam is evanescent and penetrates only the tens of Ångströms into the surface (shown in Fig 2.5), resulting an enhancement of intensities at the surface. Thus the scattering can be made surface or interface roughness sensitive with grazing incidence geometry. Additionally, the use of the grazing incidence geometry minimizes the x-ray induced sample damage effect. The grazing incidence scattering techniques, such as Grazing Incidence Diffraction (GID) and Grazing Incidence Small Angle Scattering (GISAXS), have been fre-

Figure 2.4: A photograph of Advanced Photon Source

quently applied to characterize the nano-scale structure or dynamics of surfaces, buried interfaces and thin films for various classes of materials including polymer, semiconductor or so. These techniques provide an excellent complement to more conventional nano-scale surface probes such as Atomic Force Microscope (AFM) and Scanning Electron Microscope (SEM) with comparable spacial resolution and usually better temporal resolution. Whereas both are operated in real space and giving information about local scanned area, grazing incidence scattering provides the global statistical average of structures over the entire x-ray illuminated area (usually several orders of magnitude larger) in reciprocal space. Most of the measurements included in this work were performed in grazing incidence geometry for the surface sensitivity. Specifically, we used GISAXS, Grazing Incidence X-ray Off-Specular scattering (GIXOS), as well as the XPCS with grazing incidence geometry.

GISAXS measurement was first performed in 1989 by Joanna Levine and Jerry Cohen using a rotating anode x-ray source [8] and was introduced into the

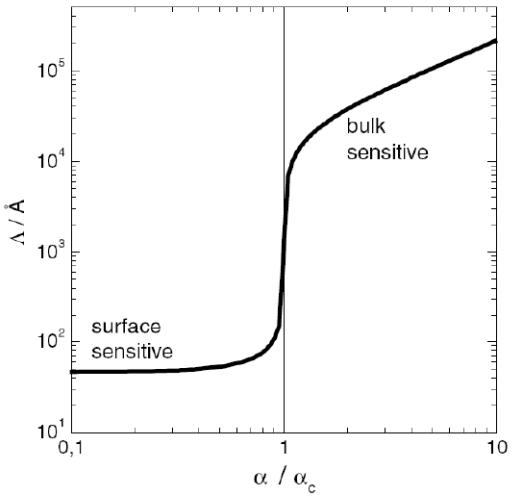

Figure 2.5: Penetration depth vs. normalized incident angle

field of soft matter and polymer in 1997 by Peter Muller-Buschbaum and co-workers [9]. This technique has been wildly used to study the nano-structured systems and extended with the new coherence and high-resolution features [10, 11].

Unlike the well-developed GISAXS technique, GIXOS [12, 13] is a young technique, which has been recently proposed as an attractive alternative to XR for structural characterization of interfaces along surface-normal with sub-nanometer resolution. In contrast to the complex motions of sample, steering crystal and detector arms required for XR scan, GIXOS data can be collected during a single exposure with an area detector in a fixed geometry, with no motion of steering crystal, sample or detector required. Additionally, the use of the grazing incidence geometry minimizes the x-ray induced sample damage effect. This makes GIXOS an ideal technique for in-situ studies of the structural and dynamic properties of liquid-air interfaces during, for example, adsorption isotherms or other phase transitions.

2.4.3 Langmuir-Blodgett Techniques

The concept of using nanoparticles, bio-molecules as elementary building blocks to develop self-assembled super-structures opened a new way of growing

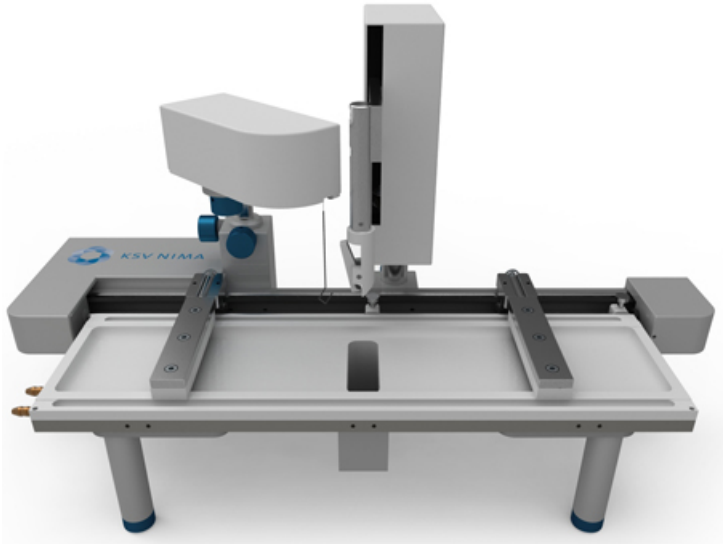

Figure 2.6: A photograph of a Langmiut-Blodgett trough system (picture from KSV NIMA)

functional nano-scale materials. Langmuir-Blodgett (LB) technique allows building up of mono-layer and multi-layer of lipids or nano-particles with an accurate control of thickness and molecular organization also with the capability of transferring the formed layer to a solid substrate. Figure 2.6 shows a typical LB trough system.

LB films are formed when amphiphilic molecules like surfactants or ligand-coated nano-particles interact with air at an airwater interface. Since the ligand tails are hydrophobic, their exposure to air is more favorable than that to water. Due to the interaction between liqands, the surfactant molecules or nano-particles arrange themselves at water surface as shown in Figure 2.7 below. This tendency can be explained by the minimization of water surface-energy. Then by changing the surface area with one or two motorized barriers, one can control the surface pressure (measured in-situ with a Wilhelmy plate) and therefore the phase of the LB film to study its rich mechanical and elastic properties.

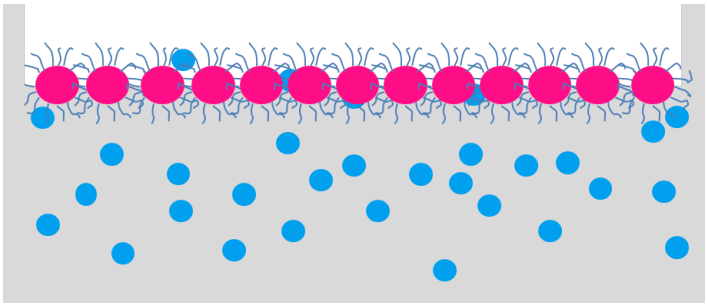

Figure 2.7: ligand-coated nanopaticles arranged at an air-water interface

2.4.4 Sample Preparations

Confined Polymer Films

Samples were prepared by spin-coating solutions of monodisperse Polystyrene (PS) dispersed in toluene on top of etched line-space silicon diffraction gratings. Immediately prior to spin-coating, gratings were cleaned with RCA1 and RCA2 processes according to a standard procedure. Spun-cast films on these gratings were then annealed in a vacuum oven to remove any residual toluene or stress from the spin-casting process. AFM of the post-annealed spun-cast sample shows that the PS is a continuous film without rupture or de-wetting over the nanoscale channels.

Nano-imprinted Polymer Patterns

Polystyrene (PS) films with a fluorosurfactant (FS) were spun-cast from toluene solutions onto UV ozone cleaned Si wafers. Line-space gratings with a pitch (period) of 424 nm were then formed by thermally embossing the polymer films with a hard silicon oxide mold 40^oC above the T_g of the PS and at elevated pressure of 500psi, followed by demolding at 55^oC. AFM and Scanning Electron Microscopy (SEM) confirmed the high quality transfer of one-dimensional periodic line-space grating patterns approximately 360 nm in height with nearly one to one line-to-space ratio.

Self-assembled Langmuir films

The self-assembled monolayers were formed by spreading a solution of phospholipid 1,2-dipalmitoyl-phosphatidyl-choline $C_{40}H_{80}NO_8P$ (DPPC) or thiolated Au nanoparticles (Ocean Nanotech) in chloroform onto the ultra-pure water surface in a Langmuir trough; then the monolayers were compressed with the motorized barrier to a target surface pressure to form multilayers. Observed under an optical microscope, the resulting monolayer film was reasonably isotropic and homogeneous across the entire sample.

Bibliography

[1] Jens Als-Nielsen and Des McMorrow. *Elements of Modern X-ray Physics*. John Wiley & Sons, April 2011.

[2] S. K. Sinha, E. B. Sirota, S. Garoff, and H. B. Stanley. X-ray and neutron scattering from rough surfaces. *Physical Review B*, 38(4):2297–2311, August 1988.

[3] M. Sutton, S. G. J. Mochrie, T. Greytak, S. E. Nagler, L. E. Berman, G. A. Held, and G. B. Stephenson. Observation of speckle by diffraction with coherent x-rays. *Nature*, 352(6336):608–610, August 1991.

[4] D. Lumma, L. B. Lurio, S. G. J. Mochrie, and M. Sutton. Area detector based photon correlation in the regime of short data batches: Data reduction for dynamic x-ray scattering. *Review of Scientific Instruments*, 71(9):3274–3289, September 2000.

[5] Hyunjung Kim, A. Rhm, L. B. Lurio, J. K. Basu, J. Lal, D. Lumma, S. G. J. Mochrie, and S. K. Sinha. Surface dynamics of polymer films. *Physical Review Letters*, 90(6):068302, February 2003.

[6] Donald H. Bilderback, Pascal Elleaume, and Edgar Weckert. Review of third and next generation synchrotron light sources. *Journal of Physics B: Atomic, Molecular and Optical Physics*, 38(9):S773, May 2005.

[7] Advanced photon sourse website. `http://aps.anl.gov`.

[8] J. R. Levine, J. B. Cohen, Y. W. Chung, and P. Georgopoulos. Grazing-incidence small-angle x-ray scattering: new tool for studying thin film growth. *Journal of Applied Crystallography*, 22(6):528–532, December 1989.

[9] P. Müller-Buschbaum, P. Vanhoorne, V. Scheumann, and M. Stamm. Observation of nano-dewetting structures. *EPL (Europhysics Letters)*, 40(6):655, December 1997.

[10] I.A. Vartanyants, D. Grigoriev, and A.V. Zozulya. Coherent x-ray imaging of individual islands in GISAXS geometry. *Thin Solid Films*, 515(14):5546–5552, May 2007.

[11] P. Müller-Buschbaum, E. Bauer, E. Maurer, S. V. Roth, R. Gehrke, M. Burghammer, and C. Riekel. Large-scale and local-scale structures in polymer-blend films: a grazing-incidence ultra-small-angle x-ray scattering and sub-microbeam grazing-incidence small-angle x-ray scattering investigation. *Journal of Applied Crystallography*, 40(s1):341, Apr 2007.

[12] Sen M. O'Flaherty, Lutz Wiegart, Oleg Konovalov, and Bernd Struth. Observation of zinc phthalocyanine aggregates on a water surface using grazing incidence x-ray scattering. *Langmuir*, 21(24):11161–11166, November 2005.

[13] L. Wiegart, S. M. O'Flaherty, P. Terech, and B. Struth. Observation of the desorption of mineral nanoparticles from a hybrid langmuir monolayer: an in situ grazing incidence x-ray (GIXOS) study. *Soft Matter*, 2(1):54, 2006.

3 Capillary Wave Dynamics of Laterally Confined Liquid Polystyrene Films

We have investigated the capillary dynamics of molten polymer films laterally confined within narrow (140 nm to 300 μm) channels using X-ray Photon Correlation Spectroscopy. For channels narrower than approximately 30 μm surface capillary fluctuations were found to be quenched in the observable range. Capillary fluctuations in channels wider than approximately 30 μm exhibit suppressed dynamics with strong channel-width dependence and directional anisotropy relative to the long axis of the channels. These confinement effects on the surface fluctuations are discussed in context of wall-pinning and meniscus effects.

3.1 Introduction

Even in the absence of externally induced vibrations, liquid surfaces are subject to thermal excited capillary fluctuations or waves. These capillary wave dynamics [1, 2] have been extensively studied in both bulk liquids and thin films with good agreement down to nanometer length-scales with capillary and hydrodynamic theories [3, 4]. The time-scale of the surface wave relaxation dynamics for a flat, isotropic molten polymer film without confinement, and with thickness h, viscosity η and surface tension γ follows the relation [3, 4]:

$$\tau[q] = \frac{2\eta[\cosh(qh)^2 + q^2h^2]}{\gamma q[\sinh(qh)\cosh(qh) - qh]} \tag{3.1}$$

Several confining geometries, e.g. planar thin films and cylindrical pores [5, 4, 6], have been reported to affect the liquid surface dynamics [4, 7, 8, 9] as well as other fluid properties, including the shear rate dependence of the viscosity and polymer chain entanglement density [10, 6, 11, 12, 13]. The length-scale at which geometrical confinement has a dramatic effect on polymer properties is typically on the order to the gyration radius of the polymer, R_g. The effects of vertical confinement on molten polymer films with flat geometry have been well studied [14, 15, 13, 4, 7, 8]. Previous X-ray Photon Correlation Spectroscopy (XPCS) studies [16, 15, 4] of capillary dynamics in polystyrene (PS) thin flat films found them to be in good agreement with the theory of over-damped thermal capillary waves [3, 4]. For ultra-thin molten polymer films, where the film thickness approaches R_g, viscoelastic effects strongly suppress the surface fluctuations [14]. In more complex geometries with a thin molten polymer over a submerged nanostructured grating, the surface dynamics behavior exhibits an anisotropic dependence on the capillary wave relaxation depending on the alignment of the waves to the underlying structure [9]. In contrast to vertical confinement, the effects of lateral confinement on the surface dynamics and effective viscoelastic properties of molten polymer films have not been studied and not well understood. Indeed, if similar suppression or "quenching" of dynamics present in vertical confinement exists as well for lateral confinement, then it may be possible to create "frozen" lines of molten polymer in channels of appropriate width [17, 18]. Since the surface dynamics are tightly linked to issues of de-wetting, this may add new understanding on patterned de-wetting in lateral confinement [19, 20, 9, 21]. Here we present a series of XPCS dynamics measurements on the surface capillary fluctuation behavior of molten polymer films confined latterly within nanoscale and micron-scale channels. Surface dynamics in the channels were significantly suppressed within observable ranges depending on channel width and anisotropic dynamics behavior relative to the channel direction was also observed. Possible mechanisms based on surface energy and meniscus effect to explain the dynamics suppression and

anisotropic behavior as a function of lateral confinement are discussed.

3.2 Experimental

Latterly confined polymer film samples were prepared by the spin-coating of solutions of PS with $M_w = 18,000 g/mol$ and polydispersity index 1.15 (Scientific Polymer Products Inc.) dispersed in toluene over etched line-space silicon diffraction gratings of various periodicity and channel width from roughly 50 nm, up to 300 microns [22]. The PS mass loading in solution, which varied between 0.5 and 2%, dependent on sample, was set to target near complete filling of the nanostructures without substantial overfilling. Immediately prior to spin-coating, gratings were cleaned to remove organic contaminants with standard RCA1 and RCA2 processes [23]. Spun-cast samples were then rapidly annealed under vacuum at 180 $^{\circ}C$, a temperature substantially above the glass transition temperature T_g, for a 24 hour period to remove residual solvent and any latent stress from the spin-coating process. More importantly, this annealing process induces the low molecular mass PS to de-wet into droplets on the tops of the line-space grating as confirmed with AFM, leaving only polymer filled channels after annealing and isolated droplets of PS on the tops of the Si lines. AFM measurements confirm that the polymer in the channels does not de-wet due to the stabilizing effect of the walls. This is likely linked to our XPCS findings on the suppression of the surface dynamics and will be discussed later.

Multiple different width and period line-space gratings were used for these surface dynamics in lateral confinement experiments. The finest gratings were etched Si structures with approximate channel widths of 140 nm, 208 nm, 416 nm (LightSmyth) and 1.3 μm, 7.5 μm (MicroMasch TGZ series AFM calibration gratings). In addition, 50 μm, 100 μm, 150 μm, and 300 μm were fabricated in-house at NIST via standard photolithographical methods. While channel depth varied significantly with the channel width due to differences in fabrication, in all cases, the channel depth was many times the radius of gyration, ($R_g \sim 5$ nm) of the polymer used [4]. This indicated that vertical confinement effects should not have been

present. The smallest (widths of 140 nm, 208 nm, 416 nm) channels had depths of 110 nm, 125 nm and 218 nm respectively. The 1.3 μm, 7.5 μm channels had depths of 1 μm and 1.5 μm. The largest channels (50 μm 300 μm) had a depth of 300nm. The thickness of the PS films were 80 $\sim$ 100 nm, dependent on channel width and depth, as measured with X-ray Reflectivity (XRR) measurements [22]. Again, this indicates that vertical confinement effects observed in ultrathin films [4] are expected to be negligible here thus we are only probing issues of geometrical lateral confinement due to the meniscus and contact line pinning at the channel walls.

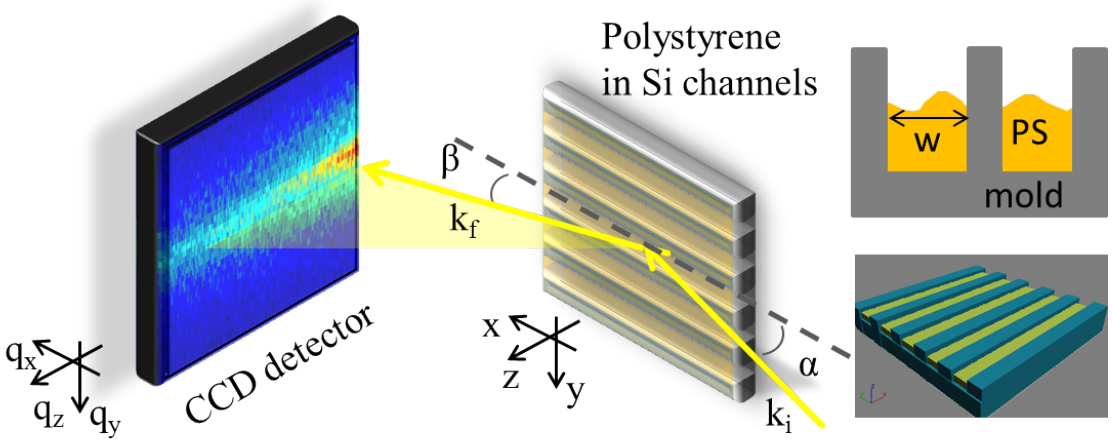

Figure 3.1: The schematic of the XPCS experiment setting and Cross-section illustration of the sample configurations of the PS film and grating.

XPCS experiments to measure the capillary wave dynamics relaxation behavior in the channels were carried out at beamline 8-ID-I at the Advanced Photon Source (APS) using a monochromatic x-ray of energy of 7.35 keV. The dimensions of the beam were defined by two sets of slits to be 20 $\mu m \times 20$ μm, comparable to the x-ray coherent lengths of 7 μm and 90 μm in the horizontal and vertical direction, respectively. The partially coherent x-ray beam was scattered by the instantaneous arrangement of spontaneous surface capillary fluctuations and produced a "speckle" in the far-field. By calculating the time autocorrelation function of the speckle intensities as a function of the wave vector transfer q, we extract the q-dependent relaxation of the capillary wave fluctuations. The experimental ge-

ometry is illustrated in Figure 3.1. The x-ray incidence angle α, was set to below the critical angle [24] (grazing incidence) of the PS for total external reflection, thus only surface fluctuations were probed by the x-ray beam and the scattering from the film-substrate interface was negligible. The grazing incident x-ray beam was carefully aligned parallel to the channels to avoid shadowing of liquid surface [22]. XPCS speckle patterns over the in-plane wave-vector transfer q range of 1×10^{-4} to $1 \times 10^{-3} \mathring{A}^{-1}$ were collected with a charge-couple device (CCD) area detector, located about 3.5 m downstream from the sample. X-ray speckle patterns were correlated over relative time delays ranging from 0.1 s to 1000 s. XPCS data were collected at multiple specific sample temperatures between 110 $^{\circ}C$ and 180 $^{\circ}C$ - all well above the glass transition temperature of PS $T_g = 100\ ^{\circ}C$. At these temperatures, the polymer is expected to behave as a viscoelastic liquid with temperature dependent surface dynamics. In addition, XRR measurements were performed concurrently with XPCS to determine the polymer thickness within the channels.

Given the lateral extent of the x-ray beam as 20 μm, for the samples with the channel width $w \leq 7.5\ \mu m$ the x-ray footprint covered many channels regardless of lateral positioning. Because the de-wetted polymer droplets on top of the Si lines have a high curvature meaning that any surface fluctuations cost very high energy, thus the contribution from these polymer droplets to the dynamic scattering is negligible due to the geometry, as well as the static scattering from the top surfaces of the Si lines. For the larger channel samples ($w \geq 50\ \mu m$), the lateral positions of the samples were carefully adjusted to ensure that the incident x-ray beam illuminated only the polymer at the central area in a channel, as was verified by simultaneous XRR measurements.

3.3 Results and Discussion

From the polymer surface confined within small channels ($140\ nm \sim 7.5\ \mu m$), we observed static x-ray speckle patterns over the timescales up to several hours indicating that the surface fluctuation dynamics were quenched when confined in

channels with width up to 7.5 μm. Fig 3.2(a) shows the profiles of a line cut of the speckle pattern for the polymer surface confined in 140 nm channels at 170°C. Each line is the intensity distribution in the selected area (yellow area in left inset) averaged over every 50 frames ($\sim 10 minutes$). The persistence of the line profile at all times indicates that the speckle pattern is static during the sampling period thus surface fluctuations are quenched in the observable range. In contrary, Fig 3.2(b) shows the same analysis for the data from the surface of thin polymer film over submerged Si channels with same width (140 nm) at the same temperature (170°C) [11]. This configuration is referred to as "overfilled" as it is the identical underlying silicon gratings with the polymer overfilling the channels. Note that this overfilled sample was found to have surface dynamics with characteristic relaxation timescale around 10 seconds. The intensity distribution curves in Fig 3.2 (b) are the average results over only 5 frames ($\sim 1 minute$). The dramatic change in the line profile indicates the speckles are fluctuating and the dynamics of the system is comparable to the sampling time. This analysis suggests that the polymer surface revives the capillary fluctuations when the contact lines of polymer to the Si walls are absent as the nanoscale channels are submerged by the polymer film [22]. Together with the fact that the surface quenching effect appears to extend far beyond a few R_g, these lead to a possible mechanism of the surface quenching in the laterally confined case, namely, the pinning effect of the polymer contact lines to the Si channel walls, which will be discussed later in this letter.

However, as the channel width (in the laterally confined case) is increased to be greater than 50 μm, the XPCS measurements again show measurable surface capillary dynamics within the observable length scale range. Such a transition from quenched dynamics to the standard capillary wave dynamics behavior is expected, as one must eventually recover the flat film geometry in some limit. What is surprising is the length scale (~ 10 μm) at which this transition back to standard fluctuations occur, since in comparison vertical confinement is occurring only when length scales approach $2 \sim 4R_g$. This difference of three orders of magnitude strongly suggests that dynamics suppression in the lateral geometry is governed

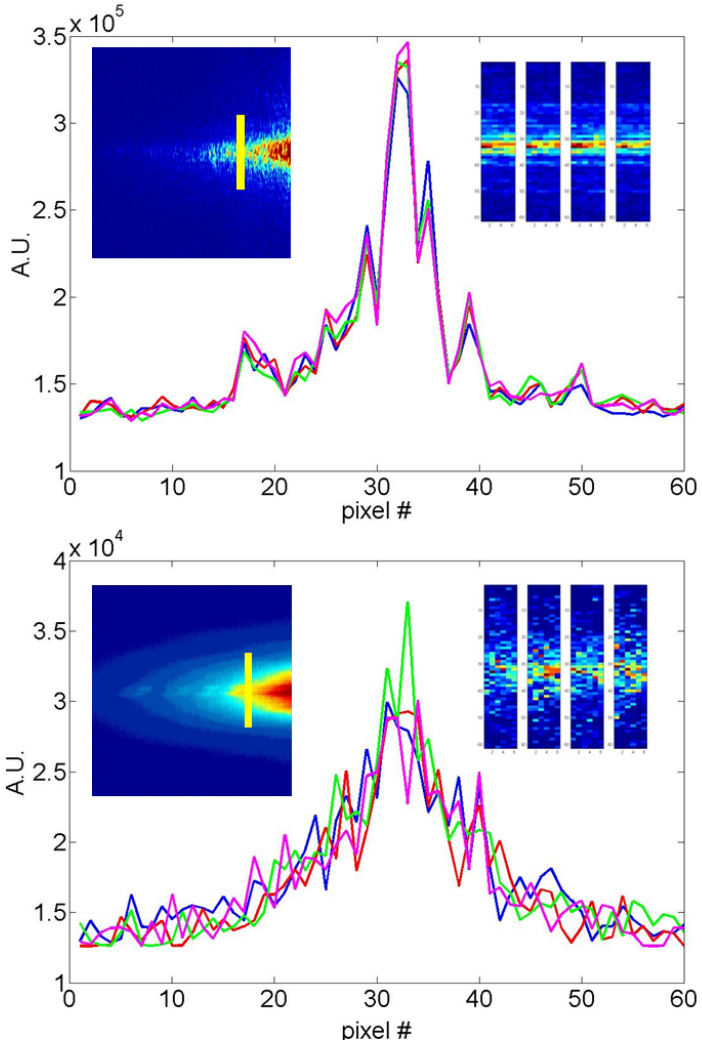

Figure 3.2: (a): the horizontally-integrated intensity vs. vertical pixel index for four segments in the right inset of speckle. Four segments are the selected areas (shown as yellow) of the speckle patterns from the polymer surface confined in 140 nm channels at 170°C. Each segment is averaged result of 50 frames. (b): the horizontally-integrated intensity vs. vertical pixel number for four segments of speckle patterns from the surfaces of overfilled polymer in 140 nm channels at 170°C. Each segment is the average of 5 frames.

by a significantly different physical mechanism.

To quantitatively analyze the change in speckle pattern as a function of time, the intensity-intensity time autocorrelation function is calculated as

$$_2(q,\tau) = \frac{< I(q,t)I(q,t+\tau) >}{< I(q,t) >^2} \tag{3.2}$$

where $I(q,t)$ is the scattering intensity at wave vector transfer q at time t and τ is the delay time. The averaging is performed over time t. For a given q, the value of $g_2(q,\tau)$ decays as the time delay τ increases. The $g_2(\tau)$ function can then be fit to a single-exponential decay function as:

$$_2(\tau) = 1 + \beta exp(-2\tau/\tau_0) \tag{3.3}$$

Where the fitting parameter β is the Siegert factor [25] related to speckle contrast and τ_0 is the relaxation time constant of the measured dynamics. This procedure has been discussed in detail in Ref [16]. The representative $g_2(\tau)$ functions for four different wave vector transfer q values obtained from the polymer surface confined in 100 m wide Si channels at $130°C$ are shown in top panel of Fig 3.3.

The relaxation dynamics for flat films (Eq 3.1) suggests that τ/h should be solely a function of qh, to make the comparison between different channel sizes thickness-independent, Fig 3.3 shows the quantity τ/h versus qh for the polymer film in the larger channels (50 $\mu m \sim$ 300 μm) at $130°C$. The dashed lines are fits [4] of the relaxation time as a function of q for unconfined/flat polymer films with the same film thickness, and molecular mass at the given temperature. The fits to Eq 3.1 give the "effective" viscosity of the polymer films for varying lateral confinement (specifically channel width). As the channel width decreases from 300 m, the "effective" viscosity of the confined polymer film deviates from the bulk value $\eta = 1 \times 10^5 Pa \cdot s$ [26](dashed line in inset).

As noted above, the transition length-scale where we observed the lateral confinement effect is several orders of magnitude larger than the PS R_g. This is possibly due to the fact that the polymer contact lines are fixed to the surfaces of Si channel walls. The pinning of the edges of the polymer melt in the channel creates a meniscus with a Laplace pressure defined as:

$$\Delta P = 2\gamma/R \tag{3.4}$$

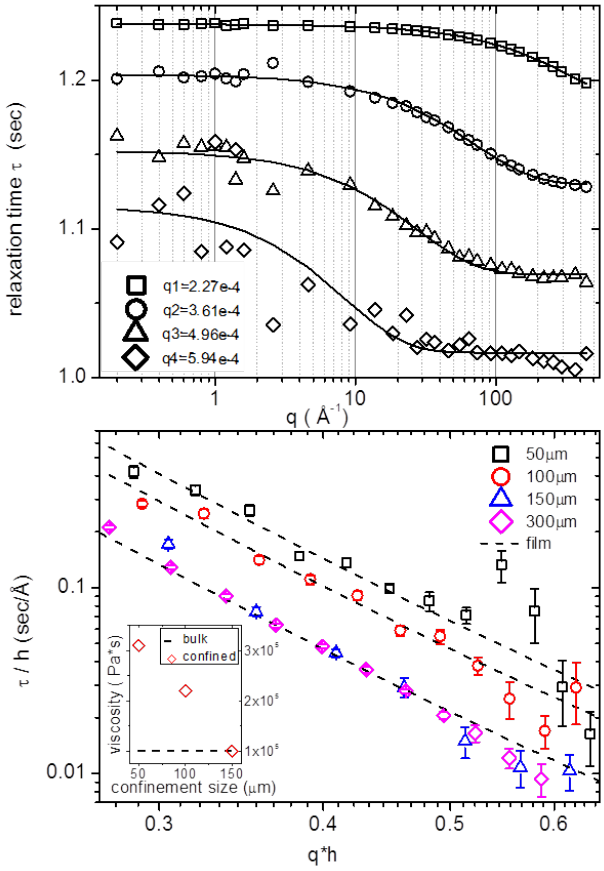

Figure 3.3: (a): the Intensity-intensity time autocorrelation function $g_2(\tau)$ acquired from the polymer surface confined in 100 μm channels at 130°C for four different wave vector transfer q values. Lines are fits to single exponential decay function. Data and fits were offset vertically for clarity. (b): the thickness-renormalized τ/h vs. qh plot for the surface capillary dynamics of polymer surface confined in Silicon channels of different width. Dashed lines are fits to Eq 3.1. The inset shows the "effective" viscosity for the polymer films confined in different size channels.

Where γ is the surface tension and R is the curvature radius. Any perturbations to the meniscus would have to be driven by a pressure greater than this Laplace pressure. Thus only the fluctuations with wavelengths smaller than the radius of the static meniscus would be excited at the polymer surface. Our

XPCS measurement covers the q range of $2 \times 10^{-4} \sim 6 \times 10^{-4} \mathring{A}^{-1}$ or lengthscale of $1 \sim 3\ \mu m$. For channel widths less than $\sim 1\ \mu m$, the excited surface fluctuations are out of the XPCS window therefore not measureable. When the channel width or meniscus radius increases above the max measurable wavelength ($\sim 3\ microns$), the static meniscus starts to get overpowered by the natural thermal fluctuations that are in the XPCS window, and one starts to see dynamics. A cutoff fluctuation wavelength λ_c given by the balance between Laplace pressure and thermal energy would be a fraction of the channel width, approximately $w/10$ for the first order approximation, which is agreed by the experimental results. For example, the cut-off wavelengths are approximately 140 nm, 750 nm, 5 μm and 30 μm for channels with width 418 nm, 7.5 μm, 50 μm and 300 μm, respectively. Based on this assessment, one would expect to see a suppressing effect for surface fluctuations for molten polymer in channels with widths less than approximately 30 μm. This cut-off channel width falls right between our two channel widths, the maximum width of 7.5 μm with which we observed no surface dynamics and the minimum width 50 μm with which we observed suppressed surface dynamics. Since the channels of width 300 μm are roughly one order magnitude wider than the channel with cut-off width, the polymer surfaces confined in between can be considered as unaffected surfaces for the measurable q range, which agrees with the measured dynamics from polymer surface confined in 300 μm channels. This simple model predicts what we see with the molten polymer laterally confined in channels of various widths, also holds promise to explain the surface behaviors with different lateral confinement geometry. Additionally, since the lateral confinement provided by Si channels is quasi-1D and thus highly anisotropic, one might expect that the surface capillary dynamics are significantly different in the orthogonal directions along the channel (the long axis of the channels) or across the channel. The directional dependence of the dynamics was also studied by examining the azimuthal dependence of the correlation-decay time constants. Because of channel shadowing effects that limit the range of accessible azimuths and mixing of q_x and q_y capillary fluctuation terms, our analysis is qualitative, but general trends in the behavior of the dynamics can be observed. Specifically, for larger azimuth angles with respect

to the long axis of the channels, the surface dynamics become slower. The dynamics derived from this analysis are shown in Fig 3.4. Ideally the XPCS analysis of the data taken on an isotropic polymer surface (i.e. a flat film) should give exactly same relaxation time for a constant $|q_{xy}|$ ($q_{xy}^2 = q_x^2 + q_y^2$) with no dependence on the azimuth angle. The relaxation time analyzed from three azimuthally-different segments (shown as CCD sections of speckle pattern in Fig 3.4,corresponding to 0, 40.86, 59.94, respectively) of 150 μm channels data collapse to form a single curve indicating the surface is isotropic which agrees with the channel size dependence result. In contrast, the relaxation time of the 3-segment XPCS analysis from the polymer surface confined in the 50 μm channels dont collapse into one single curve. The capillary fluctuations at larger azimuth angle become slower as we expected. This indicates that the surface capillary dynamics across the channel is significantly slower than that along the channel, which demonstrates the anisotropy of the confinement effect to the polymer surface dynamics due to the highly anisotropic nature of the confinement. The effective viscosity along different azimuthal angles on the confined polymer surface is $2.8 \times 10^5 Pa \cdot s$, $3.1 \times 10^5 Pa \cdot s$, $4.5 \times 10^5 Pa \cdot s$ for segment 1, 2, 3 respectively, given by the fits of relaxation time to Eq 3.1 (shown as dashed lines in Fig 3.4), all of which are greater than the bulk viscosity of $1 \times 10^5 Pa \cdot s$ [26].

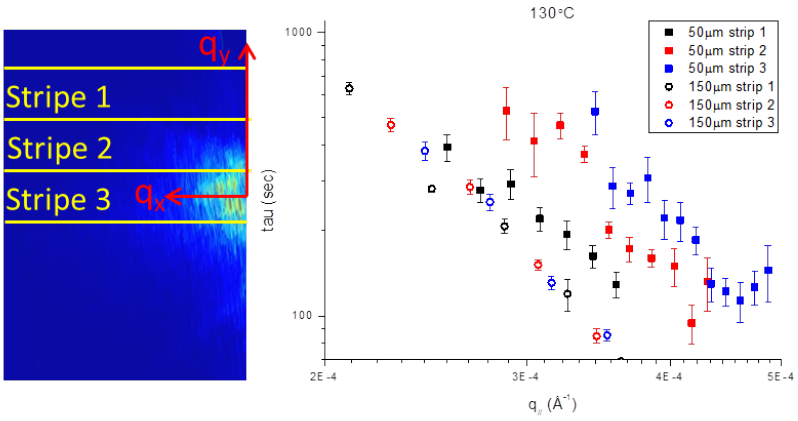

Figure 3.4: The sketch of the 3-segment approach (left) and the result from XPCS data for 50 μm (squares) and 150 μm (open dots) channel samples. Black, red and blue symbols represent results for segment1, segment2, segment3, respectively.

3.4 Conclusions

We have reported XPCS studies on the surface capillary wave dynamics of polymer films with highly anisotropic lateral confinement. We have found three distinct regimes of dynamics behavior. First, if the polymer is confined in channels of width smaller than $\sim 30\ \mu m$, the dynamics are surprisingly completely suppressed within our observable range. Second, when the channels are wider than 150 μm, the surface dynamics are indistinguishable from the surface dynamics of bulk thin films. Third, in channels with widths $50\ \mu m \leq w < 150\ \mu m$, a confinement size dependence of the surface capillary dynamics was observed. Specifically, the molten polymer films confined in larger channels were found to exhibit surface capillary fluctuations with shorter relaxation time, implying faster surface dynamics in the larger channels. In addition, we find that the measured surface capillary wave dynamics is dramatically different in the two orthogonal directions relative to the channels suggesting an anisotropic effect. The cut-off lengthscale of the confinement effect is remarkably well represented by a roughly $1/10^{th}$ of the channel width using a simple first order effect approximation. Its worth noting that this cut-off lengthscale could is multiple orders of magnitude larger than the gyration radius of the polymer R_g. This suggests that this lateral confinement effect is a pure surface tension and contact line pinning effect rather than a finite size/entanglement issue as with the previously reported vertical confinement effects [4, 7, 8]. This finding may have an important impact on the study of nanoscale patterned polymer structures, on the design of polymer-based nanoscale fabrications and on the understanding of the physics of surface fluctuations.

3.5 Acknowledgements

The text of this chapter, in part, is a reprint of the material as it appears in:

Y. Dai, K. J. Alvine, H. Ro, C. L. Soles, S. Narayanan, A. R. Sandy and O. G. Shpyrko, "Capillary Wave Dynamics of Laterally Confined Liquid Polystyrene Films", in preparation,(2013)

Bibliography

[1] A. Braslau, P. S. Pershan, G. Swislow, B. M. Ocko, and J. Als-Nielsen. Capillary waves on the surface of simple liquids measured by x-ray reflectivity. *Physical Review A*, 38(5):2457–2470, 1988.

[2] Oleg Shpyrko, Patrick Huber, Alexei Grigoriev, Peter Pershan, Ben Ocko, Holger Tostmann, and Moshe Deutsch. X-ray study of the liquid potassium surface:structure and capillary wave excitations. *Physical Review B*, 67(11):115405, March 2003.

[3] Josef Jäckle. The spectrum of surface waves on viscoelastic liquids of arbitrary depth. *Journal of Physics: Condensed Matter*, 10(32):7121–7131, August 1998.

[4] Hyunjung Kim, A. Rhm, L. B. Lurio, J. K. Basu, J. Lal, D. Lumma, S. G. J. Mochrie, and S. K. Sinha. Surface dynamics of polymer films. *Physical Review Letters*, 90(6):068302, February 2003.

[5] Gustavo Luengo, Franz-Josef Schmitt, Robert Hill, and Jacob Israelachvili. Thin film rheology and tribology of confined polymer melts: contrasts with bulk properties. *Macromolecules*, 30(8):2482–2494, 1997.

[6] Kyusoon Shin, Sergei Obukhov, Jiun-Tai Chen, June Huh, Yoontae Hwang, Soonchun Mok, Priyanka Dobriyal, Pappannan Thiyagarajan, and Thomas P. Russell. Enhanced mobility of confined polymers. *Nature Materials*, 6(12):961–965, 2007.

[7] Hyunjung Kim, A Rhm, L.B Lurio, J.K Basu, J Lal, S.G.J Mochrie, and S.K Sinha. X-ray photon correlation spectroscopy on polymer films with molecular weight dependence. *Physica B: Condensed Matter*, 336(12):211–215, 2003.

[8] Hyunjung Kim, A Rhm, L.B Lurio, J.K Basu, J Lal, S.G.J Mochrie, and S.K Sinha. Polymer film dynamics using x-ray photon correlation spectroscopy. *Materials Science and Engineering: C*, 24(12):11 – 14, 2004. ¡ce:title¿14th Molecular Electronics and Devices Symposium¡/ce:title¿.

[9] Kyle J. Alvine, Oleg G. Shpyrko, Peter S. Pershan, Kyusoon Shin, and Thomas P. Russell. Capillary filling of anodized alumina nanopore arrays. *Phys. Rev. Lett.*, 97:175503, Oct 2006.

[10] Rajesh Khare, Juan J. de Pablo, and Arun Yethiraj. Rheology of confined polymer melts. *Macromolecules*, 29(24):7910–7918, January 1996.

[11] Kahp Y. Suh, Pilnam Kim, Hoon Eui Jeong, and Jae Kwan Kim. Measurement of viscosity of confined polymer melt using capillary kinetics. *Nanoscale and Microscale Thermophysical Engineering*, 10(3):263–274, 2006.

[12] J. Wang, M. Tolan, O. H. Seeck, S. K. Sinha, O. Bahr, M. H. Rafailovich, and J. Sokolov. Surfaces of strongly confined polymer thin films studied by x-ray scattering. *Physical Review Letters*, 83(3):564–567, July 1999.

[13] Zhang Jiang, Mrinmay K. Mukhopadhyay, Sanghoon Song, Suresh Narayanan, L. B. Lurio, Hyunjung Kim, and Sunil K. Sinha. Entanglement effects in capillary waves on liquid polymer films. *Phys. Rev. Lett.*, 101:246104, Dec 2008.

[14] Zhang Jiang, Hyunjung Kim, Heeju Lee, Young Joo Lee, Xuesong Jiao, Chunhua Li, Laurence B. Lurio, Xuesong Hu, Jyotsana Lal, Suresh Narayanan, Alec Sandy, Miriam Rafailovich, and Sunil K. Sinha. Structure and dynamics of thin polymer films using synchrotron X-ray scattering. *Journal of Applied Crystallography*, 40(s1):s18–s22, Apr 2007.

[15] Zhang Jiang, Hyunjung Kim, Simon G. J. Mochrie, L. B. Lurio, and Sunil K. Sinha. Surface and interfacial dynamics of polymeric bilayer films. *Physical Review E*, 74(1):011603, July 2006.

[16] D. Lumma, L. B. Lurio, S. G. J. Mochrie, and M. Sutton. Area detector based photon correlation in the regime of short data batches: Data reduction for dynamic x-ray scattering. *Review of Scientific Instruments*, 71(9):3274–3289, September 2000.

[17] A. Levent Demirel and Steve Granick. Origins of solidification when a simple molecular fluid is confined between two plates. *The Journal of Chemical Physics*, 115(3):1498, 2001.

[18] A. Levent Demirel and Steve Granick. Glasslike transition of a confined simple fluid. *Physical Review Letters*, 77(11):2261–2264, September 1996.

[19] K. Y. Suh and Hong H. Lee. Anistropic hole formation in thin polymer films confined by walls. *The Journal of Chemical Physics*, 115(17):8204–8208, 2001.

[20] K. Y. Suh, Joonhyung Park, and Hong H. Lee. Controlled polymer dewetting by physical confinement. *The Journal of Chemical Physics*, 116(17):7714–7718, 2002.

[21] Kyle J. Alvine, Yifu Ding, Jack F. Douglas, Hyun Wook Ro, Brian C. Okerberg, Alamgir Karim, Kristopher A. Lavery, Sheng Lin-Gibson, and Christopher L. Soles. Effect of fluorosurfactant on capillary instabilities in nanoimprinted polymer patterns. *Journal of Polymer Science Part B: Polymer Physics*, 47(24):2591–2600, 2009.

[22] K. J. Alvine, Y. Dai, H. W. Ro, S. Narayanan, A. R. Sandy, C. L. Soles, and O. G. Shpyrko. Capillary wave dynamics of thin polymer films over submerged nanostructures. *Phys. Rev. Lett.*, 109:207801, Nov 2012.

[23] W. Kern. *Handbook of Semiconductor Wafer Cleaning Technology - Science, Technology, and Applications*.

[24] Jens Als-Nielsen and Des McMorrow. *Elements of Modern X-ray Physics*. John Wiley & Sons, April 2011.

[25] D. L. Abernathy, G. Grbel, S. Brauer, I. McNulty, G. B. Stephenson, S. G. J. Mochrie, A. R. Sandy, N. Mulders, and M. Sutton. Small-angle x-ray scattering using coherent undulator radiation at the ESRF. *Journal of Synchrotron Radiation*, 5(1):37–47, January 1998.

[26] Donald J. Plazek and V. Michael O'Rourke. Viscoelastic behavior of low molecular weight polystyrene. *Journal of Polymer Science Part A-2: Polymer Physics*, 9(2):209243, 1971.

4 Capillary Wave Dynamics of Thin Molten Polystyrene films over Submerged Nanostructures

The surface dynamics of thin molten polystyrene films supported by nanoscale periodic silicon line- space gratings were investigated with x-ray photon correlation spectroscopy. Surface dynamics over these nanostructures exhibit high directional anisotropy above certain length scales, as compared to surface dynamics over flat substrates. A cutoff length scale in the dynamics perpendicular to the grooves is observed. This marks a transition from standard over-damped capillary wave behavior to suppressed dynamics due to substrate interactions.

4.1 Introduction

The behavior of soft matter and liquids over surfaces with nanoscale topography is an important area of active investigation in condensed matter physics and biology, with relevance to wetting phenomena [1, 2], dewetting [3, 4], self-assembly [5, 6], and cellular adhesion [7, 8]. The nanoscale surface topography strongly influences thin film wetting and morphology due to a confluence of van der Waals (vdW) interactions and surface tension effects. Examples include the wetting on complete [9] or partial nanoscale capillaries [1]. Furthermore, thermal liquid surface fluctuations (capillary waves) [10, 11] can lead to film rupture and dewetting with unique patterns and morphologies [3, 4, 12, 13]. The physics of liquid surface dynamics are of special interest in ultrathin polymer melts under

vertical confinement where thicknesses approach the radius of gyration, R_g, of the macromolecule and suppression (slowing) of dynamics due to viscoelastic effects occurs [14]. Such confinement can alter film wetting behavior.

Surface dynamics of molten flat, uniform-thickness supported polymer films above the glass-transition temperature, T_g, have been extensively studied [14, 15, 16]. For molten polymer films, thick compared to the polymer radius of gyration R_g, the isotropic surface dynamics agree well with over-damped thermal capillary wave theory [15, 17]. For ultrathin molten polymer films, with thickness $1 \sim 3$ times R_g, viscoelastic effects suppress surface dynamics; when the thickness reaches R_g, no dynamics are observed. In the present study, we investigate surface dynamics in a more complex thin polymer film system with laterally anisotropic thickness defined by a nearly flat polymer-air interface and a Si nanoscale line-space grating substrate (see Figure 4.1). To the authors knowledge, this is the first time surface dynamics have been investigated in such a system, though wetting in similar systems has been previously studied [1, 2, 18, 19]. This novel system makes possible investigation of dynamics across ultrathin regions where viscoelastic effects are paramount. Our system includes ultrathin regions ($3R_g$) over the grating lines, where one expects viscoelastic and confinement effects, and thicker, bulklike (well above $4R_g$) regions, where confinement effects are expected to be negligible, and vdW substrate interactions and surface tension forces together induce an intrinsic periodic curvature to the polymer film that is quasiconformal to the underlying nanoscale grating [2, 18]. X-ray photon correlation spectroscopy (XPCS) [20] was used to measure the wave vector dependence of the relaxation time for the capillary wave surface dynamics, quantifying dynamics in directions parallel and perpendicular to the long axis of the grating substructures over a range of temperatures well above the PS T_g. The resulting capillary wave dynamics are dramatically different in the two orthogonal directions. Parallel to the channel direction, our results can be described by the simple capillary wave model for flat isotropic films [15, 17] using an effective film thickness as described below. In the perpendicular direction, however, we observed a characteristic length scale above which surface dynamics are strongly suppressed. This cutoff appears to be related to the capillary cutoff

wave vector where the surface tension and vdW components balance [11] and is remarkably larger than the periodicity of the underlying grating. This suggests that capillary waves may propagate through ultrathin regions, which show complete suppression in the flat film of the same thickness.

4.2 Sample preparation

Samples were prepared by spin-coating solutions of 3.7% by mass loading of PS with $M_w = 97000\ g/mol$ and polydispersity index 1.05 (Scientific Polymer Products Inc.) dispersed in toluene over etched line-space silicon diffraction gratings (Light Smyth) at 2000 rpm, 1620 rpm/s for 60 s. The corresponding PS R_g is 8.4 nm [14]. Immediately prior to spin-coating, gratings were cleaned with standard RCA1 and RCA2 processes [21]. AFM of the bare gratings reveal 112 nm tall lines with periodicity of 278 nm, a line-width of 129 nm, and a duty cycle of one. Spun-cast films on these gratings were then annealed under vacuum at $180°C$ (well above the PS $T_g = 100\ °C$) for 20 hours to remove residual toluene and stress from the spin-casting process. AFM of the post-annealed sample [Figure 4.1(a)] shows that the PS forms a continuous film without rupture over the nanoscale channels. Periodic height fluctuations of amplitude 12 nm in the PS film correlate with the periodicity of the underlying nanostructure and reflect a balance of vdW and surface tension forces [18]. A cross section is illustrated (with exaggerated curvature) in Figure 4.1(b).

4.3 AFM and XRR measurements

Room temperature x-ray reflectivity (XRR) measurements to extract the polymer film thickness profiles were performed at the 8-ID-I beam line of the Advanced Photon Source (APS), Argonne National Laboratory in the perpendicular configuration as shown in Figure 4.1(c). The x-ray energy was 7.35 keV and a representative XRR profile from the sample is shown in Fig.2(a). XRR is well suited for measuring nanoscale patterns [22] and buried interfaces providing the

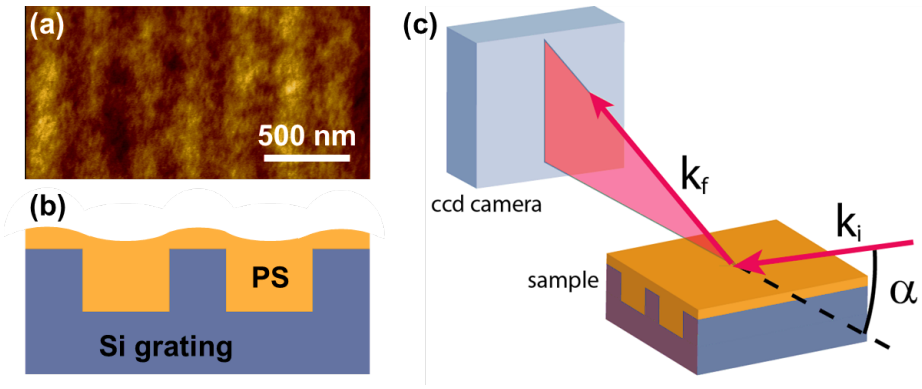

Figure 4.1: (a) AFM image of the annealed PS film over the submerged nanoscale grating. "Hills" and "valleys" correspond to the lines and channels, respectively. (b) Cross-section illustration of the sample. (c) XRR and XPCS geometry. Note that for XPCS, the sample was measured in both perpendicular (shown) and parallel (sample rotated in-plane 90°) configurations.

average electron density normal to the interface. Using the standard Parratt [23] formalism with a 3-layer model for electron density, combined with AFM data for linewidth and grating period, we extracted the film thickness profile from XRR fitting. The top two layers describe the PS above the nanoscale grating and the com- bination of polymer and grating, respectively. A third layer at the bottom of the channels, corresponding to bottom curvature of the channels, was required for good quality fitting. This bottom curvature was also observed with AFM and was likely an etching artifact. Slight deviations between the fit and the XRR data arise from nonzero sidewall angles and details of the curvature at the bottom of the channels that are not accounted for in the simple 3-layer model, which was primarily set up to determine PS film thickness across the sample.

The resultant 3-layer model fit (normalized to the silicon electron density, ρ_{inf}) is shown in Figure 4.2(b), with corresponding AFM data (averaged over several microns along the grating). The AFM line profile combines measurements from the bare grating and the PS film illustrated in Figure 4.1(b). For visual comparison, the AFM data were shifted in the z direction to align with the interfaces in the electron density profile. From XRR fitting, the PS film thickness over lines is approximately $21 \pm 5\ nm$ (All uncertainties denote $\pm 1\sigma$) and $130 \pm 5\ nm$ over the channels. From AFM, the root mean square roughness value is 0.3 nm and

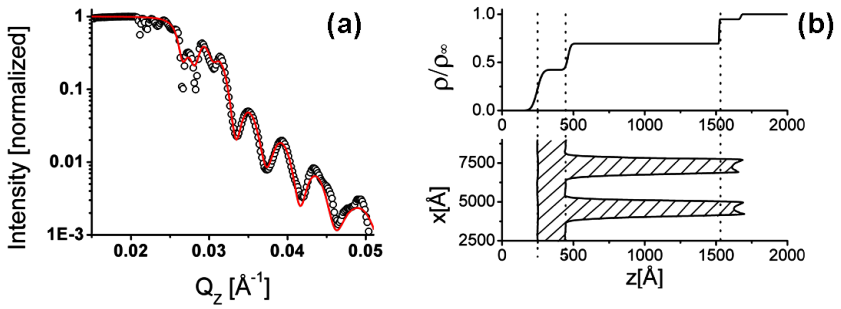

Figure 4.2: (a) XRR data and fit (solid line) based on 3-layer model for the PS-grating combination. [(b), top] Electron density fit, normalized to Si. [(b), bottom] Corresponding AFM averaged line-profile data for the PS film (indicated by crosshatching) and the bare grating have been plotted on the same scale for comparison. AFM line profiles have been shifted along z, to align with the electron density profile.

the height variation is 12 nm over the PS surface, with the larger XRR value of roughness due to variations in the PS film averaged over large areas not accounted for with local AFM measurements. Note that, as the coefficient of thermal expansion for PS is roughly $7.5 \times 10^{-4}/^{\circ}C$ and $5.5 \times 10^{-4}/^{\circ}C$ below and above T_g, respectively [24, 25], we expect that these thickness values will expand by no more than 5% as the temperature is increased to $180^{\circ}C$ and thermal expansion will have a negligible effect on our interpretation of the dynamics. The capillary wave relaxation dynamics [14, 26] were measured by XPCS on the 8-ID-I beam line of the APS, at 7.35 keV. Beam dimensions were defined with slits to be 20 $\mu m \times 20$ μm, comparable to the x-ray coherent lengths of 7 μm and 200 μm in the horizontal and vertical directions, respectively. The partially coherent x-ray beam scattered by the instantaneous arrangement of thermal capillary fluctuations produces "speckle" in the far-field scattering. By calculating the temporal autocorrelation function of the speckle intensities and fitting this with a single exponential decay function, we extracted the time-dependent relaxation of the capillary waves according to the procedure described in Refs. [16, 27] with additional detail given in the Supplemental Material. This single time-scale analysis represents the most straightforward approach to fitting the data. A more complex dual time-scale fitting analysis is described in the Supplemental Material. XPCS measurements were performed at

grazing angle with the x-ray beam either parallel or perpendicular to the grating lines as illustrated in Figure 4.1(c). These are referred to as the parallel and perpendicular configurations, respectively. The grazing angle of 0.14° was below the PS critical angle, to ensure that XPCS measurements only probed the polymer surface with a penetration depth of 9 nm. Thus, x-ray speckle contrast results from height fluctuations at the polymer-air interface; static contributions from underlying Si topography are negligible. Two-dimensional grazing incidence small angle x-ray scattering patterns were recorded on a 2D charge-coupled area detector 4 m downstream from the sample. Scattering over the wave vector Q range of $1 \times 10^{-4} \mathring{A}^{-1}$ to $1 \times 10^{-3} \mathring{A}^{-1}$ was collected with accessible time scales of 1 to 1000 s. XPCS data were collected under vacuum at sample temperatures between $140°C$ and $180°C$ where the PS behaves as a visco-elastic liquid.

4.4 XPCS experiments and results

The wave vector dependence of the capillary wave relaxation time scales are shown in Figure 4.3(a) for the parallel configuration at $140°C$, $150°C$, $170°C$ and $180°C$. XPCS measurements in this parallel configuration are dominated by capillary wave dynamics along the channels, while perpendicular measurements are dominated by dynamics perpendicular to the channels. Cross-correlation between the parallel and perpendicular modes is not assumed in this analysis. In the parallel direction, relaxation times were fit [Figure 4.3(a), solid lines] as a function of the in-plane wave vector Q, with the expression used for flat-film relaxations [15, 17]:

$$\tau[Q] = \frac{2\eta[\cosh(Qh)^2 + Q^2h^2]}{\gamma Q[\sinh(Qh)\cosh(Qh) - Qh]} \tag{4.1}$$

where η and γ are the bulk viscosity and surface tension, respectively. For this flat-film approximation, h represents an effective film thickness for the dynamics, which is affected by the relative interactions of the capillary waves with the channels. To determine h we assigned η/γ values interpolated from the literature for this molecular mass of PS as a function of temperature, leaving h as the only free fit parameter. From Refs. [25, 28] the values of η/γ are approximately $4.3 \times 10^{-2} s/nm$,

$7.8\times10^{-3}s/nm$, $5.9\times10^{-4}s/nm$ and $2.2\times10^{-4}s/nm$, for $T = 140°C$, $150°C$, $170°C$ and $180°C$, respectively. Fit values for the effective thickness are then $168 \pm 2\ nm$, $153 \pm 3\ nm$, $141 \pm 7\ nm$, and $104 \pm 6\ nm$, respectively, for$T = 140°C$, $150°C$, $170°C$ and $180°C$. These effective film thickness values are of the same order of magnitude as the thickness measurements over the channel of $130nm \ll 4R_g$. At $140°C$, h is approximately 130% the maximum thickness, decreasing to 80% at $180°C$. This cannot be accounted for by polymer thermal expansion (5% at $180°C$, with the opposite trend), but may be due in part to the assumption of bulk-like viscosity, as thin film confinement is known to affect this parameter [29]. Another issue arises from the first-order nature of our approximation of the nanostructured surface as an effective surface. The decrease in h with increasing temperature is indicative of a secondary effect. In particular, decreasing h may be caused by increased capillary wave amplitude and thus increased substrate interactions at elevated tempera- tures, leading to additional dynamics suppression at low Q.

4.5 Discussions

Relaxation time constants as a function of wave vector Q, measured in the perpendicular configuration, are shown in Figure 4.3(b) for temperatures of $140°C$, $150°C$ and $170°C$. Data at $180°C$ was not measured in this geometry due to the close similarity between the results observed in the parallel configuration between $170°C$ and $180°C$.

In this configuration, XPCS probes dynamics propagating perpendicular to the channels, across the submerged corrugations. It is apparent from the data that the relaxation dynamics in the perpendicular configuration are radically different from those in the parallel configuration. A striking cutoff is observed for all temperatures at low Q. Fits (solid lines) from the parallel configuration data for the three temperatures are shown superimposed over the perpendicular data without modification, in the high Q range with good agreement. However, for low Q values below approximately $4.3 \times 10^{-4}\mathring{A}^{-1}$ (a length scale of $\sim 1.45\mu m$), the time scales for all temperatures superimpose and indicate dramatically suppressed dy-

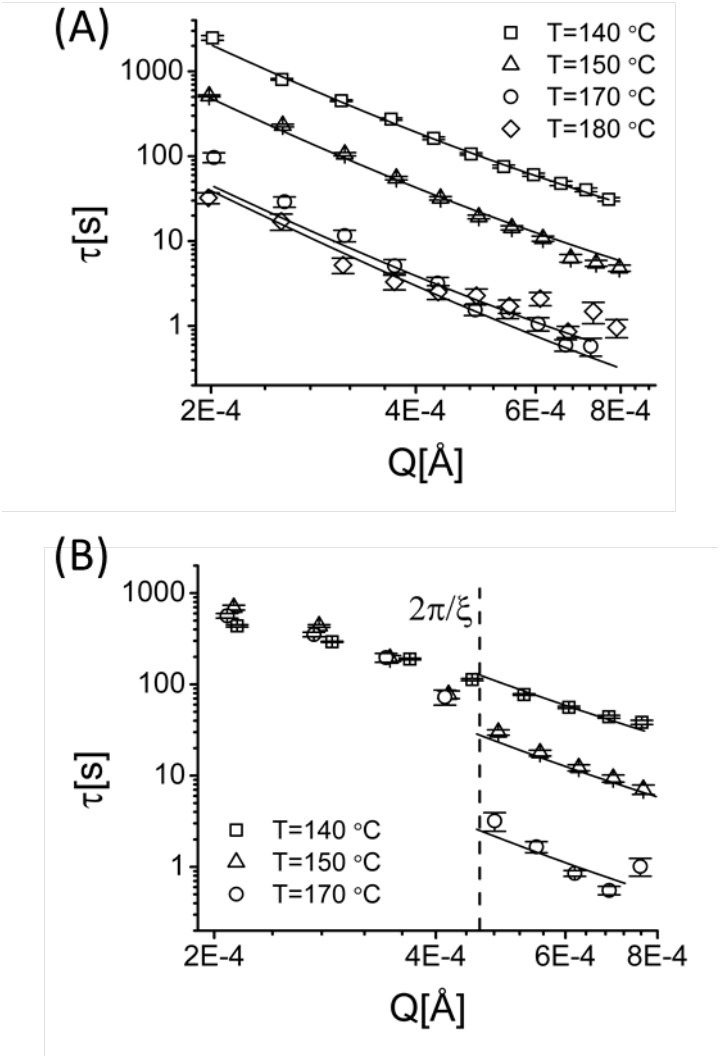

Figure 4.3: (a) Capillary relaxation time constants as a function of wave vector Q for temperatures $T = 140°C$, $150°C$, $170°C$ and $180°C$ in the parallel configuration. Solid lines are fits to the data based on the flat-film model. (b) Capillary relaxation time constants for temperatures $T = 140°C$, $150°C$ and $170°C$ in the perpendicular configuration. Solid lines are the fit curves from the parallel data. The vertical dashed line represents the cutoff wave vector Q_c calculated in the text.

namics. This transition is more pronounced at higher temperatures, though even the $140°C$ data does not agree well with the "flat-film" model at the low-Q values. Moreover, the temperature dependence in the low Q range is negligible, indicating static or pinned behavior of the polymer. The low Q data cannot be fit well with the flat-film capillary wave model with any value of effective thickness. Since pre-

vious XPCS studies [14] have observed significantly suppressed dynamics in films with thickness $1 - 3R_g$, we expect that dynamics at low Q (larger length-scales) are governed in part by regions over the lines where the thickness is $23R_g$. When the film thicknesses drop below $2R_g$, chain confinement effects become important. The chains in such thin films are highly confined and have much greater surface interactions, similar to those of a grafted polymer brush [14, 29]. In the case of grafted polymer brushes, long-wavelength ($\lambda \ll R_g$) fluctuations require relatively large lateral chain displacement to maintain monomer density and therefore have a high entropic penalty [30]. This penalty suppresses long-wavelength dynamics relative to R_g. A more complex treatment of the XPCS data for the perpendicular geometry using two time scales is given in the supplemental materials section. This alternate analysis suggests a possible combination of fast and slow dynamic behavior, where the slower dynamics dominate the behavior at low Q.

In our system, the nonuniform thickness introduces lateral anisotropy due to locally varying vertical confinement of the polymer. The nanoscale grating channel width is 129 nm, and yet we do not observe the transition to suppressed dynamics until much larger length-scales of $1.45\mu m$, which is roughly 5 periods of the underlying grating. This suggests that shorter wavelength modes may propagate across the ultra-thin regions with thick-film-like dynamics. Otherwise, a transition length scale of approximately 129 nm should be observed. This adds new insight to previous studies where all capillary wave dynamics were found to be significantly suppressed in ultra-thin polymer films with thicknesses of $1 - 3R_g$.

The interplay between surface tension and vdW polymer- substrate interactions may also contribute to the transition to suppressed dynamics along the perpendicular direction. This is evident by the sinusoidal surface undulations in the PS film measured with AFM and shown in Figure 4.1(a). Surface tension acts to smooth or flatten the PS film, as there is an energetic penalty for film curvature, while the vdW polymer-substrate interactions act to make the film nearly conformal to the underlying structure [18]. Thus, the meta-stable [31] equilibrium state of the PS film over the submerged nanoscale grating is not flat, but has the weak surface corrugation correlating with the substrate. At small length scales

and high Q, the surface tension dominates. At some value of $Q = Q_c$, however, there is a crossover to a vdW interaction dominated region at low Q. For $Q < Q_c$ the substrate interactions add additional penalty to surface height fluctuations. In the ultrathin region this Q_c corresponds to a cutoff length scale, $\xi = 2\pi/Q_c$, which is given by [11]:

$$\xi = d^2(\frac{2\pi\gamma}{A_{eff}})^{1/2} \tag{4.2}$$

where A_{eff} is the effective Hamaker constant for PS on silicon. The parameter d is the PS film thickness over the grating lines since the vdW effects from the channel bottoms are negligible. Based on an effective Hamaker constant [32] $A_{eff} = 1.8 \times 10^{-20}\ J$, surface tension $\gamma = 31\ mN/m$, and film thickness of 21 nm over the lines, $\xi \approx 1.45\ \mu m$ which agrees remarkably well with the observed transition from fast to slow dynamics. The corresponding Q_c is denoted in Figure 4.3(b) as a vertical dashed line. We point out that this is only a first-order approximation, and full analysis must include the systems periodic geometry. Nonetheless, this simple approximation elucidates fundamental physical behavior of the system.

4.6 Supplemental Materials

Example $g_2(\tau)$ relaxation curves and fits from the single timescale analysis presented in the paper are shown here from data taken at 150 $^\circ C$ in both the parallel and perpendicular configurations. Please see Figures 4.4 and 4.5.

In addition to the single timescale analysis shown in the paper, a dual time scales analysis was done to provide further details about the surface capillary wave dynamics of the overfilled thin film. The g_2 time-autocorrelation function was fit to a double exponential decay function:

$$g_2 = a_1 exp(-2\tau/\tau_1) + a_2 exp(-2\tau/\tau_2) + b \tag{4.3}$$

where a_1 and a_2 are the system contrasts and b is the fitting baseline which is very close to one. The parameters τ_1 and τ_2 give the relaxation time for different the capillary wave modes. An example is shown in Figures 4.6.

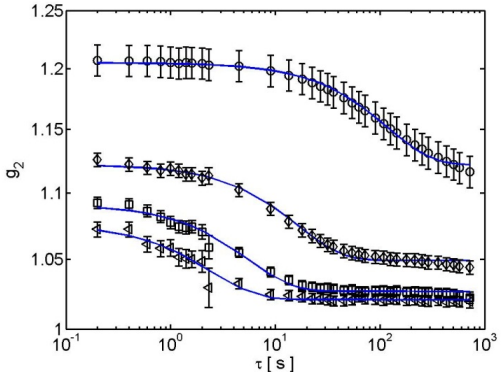

Figure 4.4: Time autocorrelation function $g_2(\tau)$ as measured from the sample in the parallel configuration for multiple wavevector transfer (Q) values. The values for Q from top to bottom respectively are 2.5×10^{-4} $\mathring{A}^{-1}$, 4.3×10^{-4} $\mathring{A}^{-1}$, 6.1×10^{-4} $\mathring{A}^{-1}$, and 8.0×10^{-4} $\mathring{A}^{-1}$. Solid lines are single timescale exponential fits to the data.

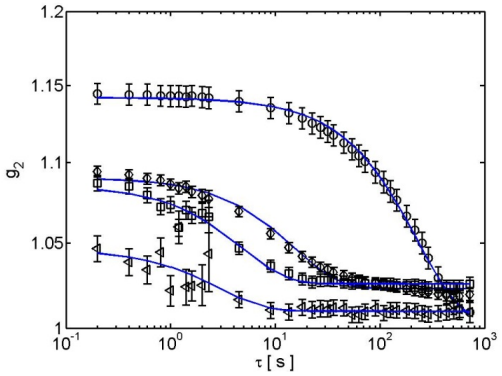

Figure 4.5: Time autocorrelation function $g_2(\tau)$ as measured from the sample in the perpendicular configuration for multiple wavevector transfer (Q) values. The values for Q from top to bottom respectively are 2.8×10^{-4} $\mathring{A}^{-1}$, 4.9×10^{-4} $\mathring{A}^{-1}$, 7.0×10^{-4} $\mathring{A}^{-1}$, and 9.1×10^{-4} $\mathring{A}^{-1}$. Solid lines are single timescale exponential fits to the data.

In Figure 4.7 and 4.8, we plot the double-exponential-decay fitting results together with the single exponential decay fitting for different temperatures. The single time scale seems sort of the 'averaged' result of the fast relaxation time and slow relaxation time indicating the 'combined' fluctuation effects of different capillary modes. The two time scales are likely related to the mixing of the two directions.

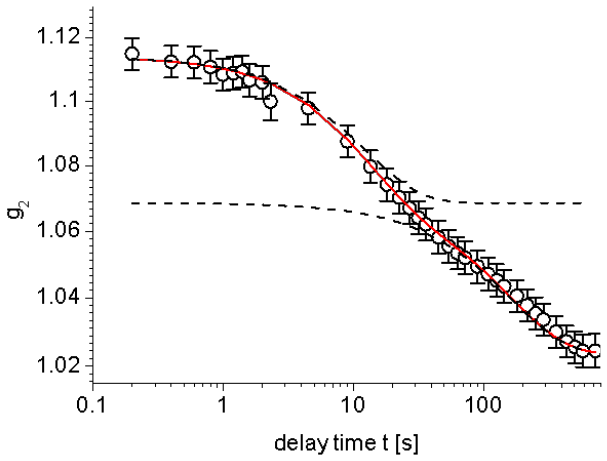

Figure 4.6: A typical g_2 function (symbols) with the fit (red line) to the double exponential decay function. The dashed lines show the double exponential decay curves.

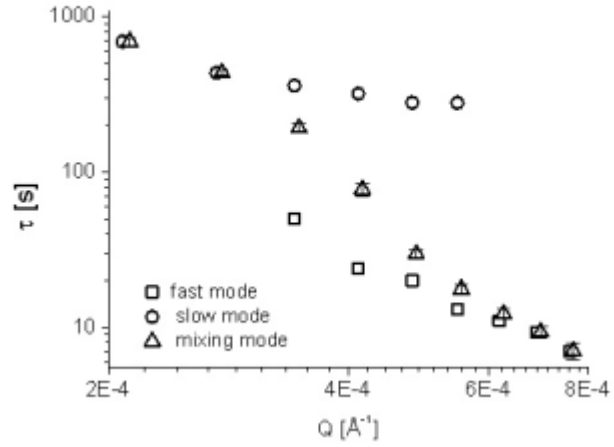

Figure 4.7: The dual timescale analysis results together with the single time scale analysis for perpendicular sample at 150 $^{\circ}C$. The relaxation times from double exponential decay fitting (circles for slow mode and squares for fast mode) and from single exponential decay (triangles) for mixing modes are shown.

4.7 Conclusion

We have used XPCS to investigate capillary wave dynamics of thin molten polymer films coated over submerged nano-structured gratings. This is a novel

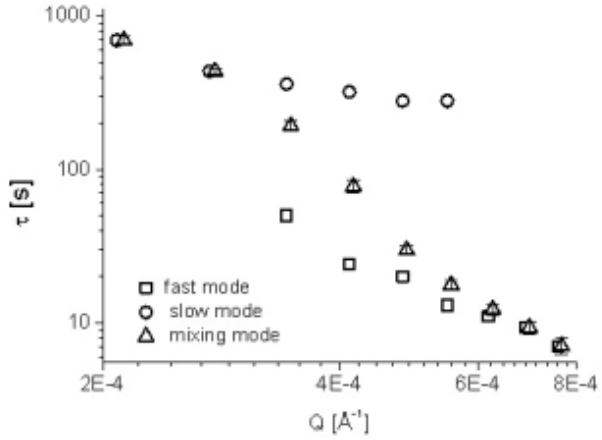

Figure 4.8: The dual timescale analysis results together with the single time scale analysis for perpendicular sample at 170 $^{\circ}C$. The relaxation times from double exponential decay fitting (circles for slow mode and squares for fast mode) and from single exponential decay (triangles) for mixing modes are shown.

area of investigation where the vertical confinement is no longer uniform. The polymer film thickness over the tops of the grating lines is $2 - 3R_g$, which is known to significantly suppress dynamics in the flat uniform-thickness films due to viscoelastic confinement effects [14]. Film thickness over the channel regions is considerably thicker, roughly 130 $nm16R_g$, where confinement effects and vdW substrate interactions are negligible. Capillary wave dynamics propagating parallel to the channels are in good agreement with the simple viscous film model, with an effective thickness close to the film depth over the channels. However, the capillary wave dynamics across the channels are dramatically different due to the combination of the PS film curvature and confinement effects arising from the vdW interactions with the substrate and the ultrathin nature of the PS film over the tops of the silicon lines. Below a cutoff length scale ($Q < Q_c$), dynamics are nearly identical to the parallel direction dynamics; above it, the dynamics are markedly suppressed and nearly temperature independent. The cutoff length-scale is remarkably well represented by the crossover from surface tension dominated to vdW dominated interactions between the PS and the substrate. This value is several times the periodicity of the grating, indicating that capillary waves may

propagate through ultra-thin regions of the polymer film, which has not been observed previously. These observations may have important impact on the design of nanoscale topography for template dewetting [4] of nanoscale patterns and on the understanding of the ultrathin polymer film physics.

4.8 Acknowledgements

The text of this chapter, in full, is a reprint of the material as it appears in:

K. J. Alvine, Y. Dai, H. Ro, C. L. Soles, S. Narayanan, A. R. Sandy and O. G. Shpyrko, "Capillary wave dynamics of thin polymer films over submerged nanostructures", *Phys. Rev. Lett.*, 109, 2012.

Bibliography

[1] Oleg Gang, Kyle J. Alvine, Masafumi Fukuto, Peter S. Pershan, Charles T. Black, and Benjamin M. Ocko. Liquids on topologically nanopatterned surfaces. *Phys. Rev. Lett.*, 95:217801, Nov 2005.

[2] Mark O. Robbins, David Andelman, and Jean-Fran çois Joanny. Thin liquid films on rough or heterogeneous solids. *Phys. Rev. A*, 43:4344–4354, Apr 1991.

[3] K. Y. Suh and Hong H. Lee. Anistropic hole formation in thin polymer films confined by walls. *The Journal of Chemical Physics*, 115(17):8204–8208, 2001.

[4] K. Y. Suh, Joonhyung Park, and Hong H. Lee. Controlled polymer dewetting by physical confinement. *The Journal of Chemical Physics*, 116(17):7714–7718, 2002.

[5] Kyle J. Alvine, Diego Pontoni, Oleg G. Shpyrko, Peter S. Pershan, David J. Cookson, Kyusoon Shin, Thomas P. Russell, Markus Brunnbauer, Francesco Stellacci, and Oleg Gang. Solvent mediated assembly of nanoparticles confined in mesoporous alumina. *Phys. Rev. B*, 73:125412, Mar 2006.

[6] Diego Pontoni, Kyle J. Alvine, Antonio Checco, Oleg Gang, Benjamin M. Ocko, and Peter S. Pershan. Equilibrating nanoparticle monolayers using wetting films. *Phys. Rev. Lett.*, 102:016101, Jan 2009.

[7] Sabrina D. Puckett, Erik Taylor, Theresa Raimondo, and Thomas J. Webster. The relationship between the nanostructure of titanium surfaces and bacterial attachment. *Biomaterials*, 31(4):706 – 713, 2010.

[8] Evelyn K.F. Yim, Ron M. Reano, Stella W. Pang, Albert F. Yee, Christopher S. Chen, and Kam W. Leong. Nanopattern-induced changes in morphology and motility of smooth muscle cells. *Biomaterials*, 26(26):5405 – 5413, 2005.

[9] Kyle J. Alvine, Oleg G. Shpyrko, Peter S. Pershan, Kyusoon Shin, and Thomas P. Russell. Capillary filling of anodized alumina nanopore arrays. *Phys. Rev. Lett.*, 97:175503, Oct 2006.

[10] A. Braslau, P. S. Pershan, G. Swislow, B. M. Ocko, and J. Als-Nielsen. Capillary waves on the surface of simple liquids measured by x-ray reflectivity. *Physical Review A*, 38(5):2457–2470, 1988.

[11] F. Brochard Wyart and J. Daillant. Drying of solids wetted by thin liquid films. *Canadian Journal of Physics*, 68(9):1084–1088, 1990.

[12] Kyle J. Alvine, Yifu Ding, Jack F. Douglas, Hyun Wook Ro, Brian C. Okerberg, Alamgir Karim, and Christopher L. Soles. Capillary instability in nanoimprinted polymer films. *Soft Matter*, 5:2913–2918, 2009.

[13] Kyle J. Alvine, Yifu Ding, Jack F. Douglas, Hyun Wook Ro, Brian C. Okerberg, Alamgir Karim, Kristopher A. Lavery, Sheng Lin-Gibson, and Christopher L. Soles. Effect of fluorosurfactant on capillary instabilities in nanoimprinted polymer patterns. *Journal of Polymer Science Part B: Polymer Physics*, 47(24):2591–2600, 2009.

[14] Zhang Jiang, Hyunjung Kim, X. Jiao, H. Lee, Y.-J. Lee, Y. Byun, S. Song, D. Eom, C. Li, M. H. Rafailovich, L. B. Lurio, and S. K. Sinha. Evidence for viscoelastic effects in surface capillary waves of molten polymer films. *Phys. Rev. Lett.*, 98:227801, May 2007.

[15] Hyunjung Kim, A. Rhm, L. B. Lurio, J. K. Basu, J. Lal, D. Lumma, S. G. J. Mochrie, and S. K. Sinha. Surface dynamics of polymer films. *Physical Review Letters*, 90(6):068302, February 2003.

[16] Hyunjung Kim, A Rhm, L.B Lurio, J.K Basu, J Lal, S.G.J Mochrie, and S.K Sinha. X-ray photon correlation spectroscopy on polymer films with molecular weight dependence. *Physica B: Condensed Matter*, 336(12):211–215, 2003.

[17] Josef Jckle. The spectrum of surface waves on viscoelastic liquids of arbitrary depth. *Journal of Physics: Condensed Matter*, 10(32):7121–7131, August 1998.

[18] M. Tolan, G. Vacca, J. Wang, S.K. Sinha, Z. Li, M.H. Rafailovich, J. Sokolov, A. Gibaud, H. Lorenz, and J.P. Kotthaus. Thin polymer films on rough surfaces. *Physica B: Condensed Matter*, 221(14):53 – 59, 1996. ¡ce:title¿Proceedings of the Fourth International Conference on Surface X-ray and Neutron Scatterin¡/ce:title¿.

[19] I. M. Tidswell, T. A. Rabedeau, P. S. Pershan, and S. D. Kosowsky. Complete wetting of a rough surface: An x-ray study. *Phys. Rev. Lett.*, 66:2108–2111, Apr 1991.

[20] S. G. J. Mochrie, A. M. Mayes, A. R. Sandy, M. Sutton, S. Brauer, G. B. Stephenson, D. L. Abernathy, and G. Grübel. Dynamics of block copolymer

micelles revealed by x-ray intensity fluctuation spectroscopy. *Phys. Rev. Lett.*, 78:1275–1278, Feb 1997.

[21] W. Kern. *Handbook of Semiconductor Wafer Cleaning Technology - Science, Technology, and Applications*.

[22] Hae-Jeong Lee, Christopher L. Soles, Hyun Wook Ro, Ronald L. Jones, Eric K. Lin, Wen li Wu, and Daniel R. Hines. Nanoimprint pattern transfer quality from specular x-ray reflectivity. *Applied Physics Letters*, 87(26):263111, 2005.

[23] L. G. Parratt. Surface studies of solids by total reflection of x-rays. *Phys. Rev.*, 95:359–369, Jul 1954.

[24] William J. Orts, John H. van Zanten, Wen-li Wu, and Sushil K. Satija. Observation of temperature dependent thicknesses in ultrathin polystyrene films on silicon. *Phys. Rev. Lett.*, 71:867–870, Aug 1993.

[25] Immergut E.H. Brandrup, J. and E.A. Grulke. *Polymer Handbook, 2 Volumes Set, 4th Edition*.

[26] Hyunjung Kim, A Rhm, L.B Lurio, J.K Basu, J Lal, S.G.J Mochrie, and S.K Sinha. Polymer film dynamics using x-ray photon correlation spectroscopy. *Materials Science and Engineering: C*, 24(12):11 – 14, 2004. ¡ce:title¿14th Molecular Electronics and Devices Symposium¡/ce:title¿.

[27] D. Lumma, L. B. Lurio, S. G. J. Mochrie, and M. Sutton. Area detector based photon correlation in the regime of short data batches: Data reduction for dynamic x-ray scattering. *Review of Scientific Instruments*, 71(9):3274–3289, September 2000.

[28] Jean-Charles Majeste, J.-P. Montfort, Ahmed Allal, and Grard Marin. Viscoelasticity of low molecular weight polymers and the transition to the entangled regime. *Rheologica Acta*, 37(5):486–499, 1998.

[29] Bulent Akgun, Gokce Ugur, Zhang Jiang, Suresh Narayanan, Sanghoon Song, Heeju Lee, William J. Brittain, Hyunjung Kim, Sunil K. Sinha, and Mark D. Foster. Surface dynamics of dry homopolymer brushes. *Macromolecules*, 42(3):737–741, 2009.

[30] Glenn H. Fredrickson, Armand Ajdari, Ludwik Leibler, and Jean Pierre Carton. Surface modes and deformation energy of a molten polymer brush. *Macromolecules*, 25(11):2882–2889, 1992.

[31] Guenter Reiter. Unstable thin polymer films: rupture and dewetting processes. *Langmuir*, 9(5):1344–1351, 1993.

[32] R. Seemann, S. Herminghaus, and K. Jacobs. Dewetting patterns and molecular forces: A reconciliation. *Phys. Rev. Lett.*, 86:5534–5537, Jun 2001.

5 Development of a Zig-Zag Capillary Instability in Nanoimprinted Polymer Gratings: A Time-Resolved GISAXS Study

The development of a novel collective type of zig-zag capillary instability has been recently observed upon annealing of line-space polymer patterns formed with nanoimprint lithography. We present here synchrotron based, time-resolved Grazing Incidence Small Angle X-ray Scattering (GISAXS) studies of the onset and development of this zig-zag instability that complement earlier Atomic Force Microscope (AFM) based studies. Time resolved GISAXS provides the in-situ measurement of the rapid formation of instability during annealing over large sample areas, a task that remains challenging for local scanning probes such as AFM. A relatively simple unit cell model has been applied to quantitatively interpret the GISAXS data.

5.1 Introduction

Thermal Embossing Nanoimprint Lithography is a simple, yet versatile nanofabrication technique capable of high throughput pattern replication with sub 10 nm resolution [1] into a variety of soft materials. These soft nanoscale patterns may be used either as sacrificial layers to transfer the pattern into a hard material or directly stamped into a functional soft material [2, 3]. This abil-

ity to directly pattern functional soft materials is one of the key advantages of the thermal embossing nanoimprint method over the more traditional UV cross-linking form of nanoimprint lithography [4, 5]. With this versatility also come unique challenges and opportunities that are not possible with the UV cross-linked nanoimprint method. One such challenge arises from thermal instability of patterned nanostructures in response to capillary forces upon annealing. The thermal instability of nanopatterned soft materials has been the topic of much recent research [6, 7, 8, 9, 10, 11]. In some cases these capillary forces can be beneficial in annealing out undesirable line edge roughness [12] or in forming desired unique and potentially useful new complex patterns from the decay of more regular structures. Examples of shape and structure changes due to capillary forces include the formation of lens like structures from pillars [13], a zig-zag and varicose formation from line-space gratings [14, 15] (see Fig 5.1 A,B for zig-zag formation), and chemically patterning from a two component line-space grating system [**?**]. These more complex patterns may have uses in high surface area conductors or chemical patterning of surfaces for self-assembly. Capillary forces can also lead to deformation, or even complete disappearance of the nanoscale pattern during thermal annealing. Previously thermally imprinted nanostructure changes upon annealing have been studied with scanning probe AFM providing local information on the deformation of the polymer grating lines. These studies have included both the height decay [7, 8] and the formation of the new zig-zag instability mentioned previously [14, 15].

Here we provide complementary synchrotron based GISAXS studies on the formation and development of the lateral zig-zag instability in a line-space polymer grating during thermal annealing of the structures at the polymer glass transition, T_g. GISAXS [16] can provide simultaneous information about the lateral deformation of the lines as well as the decay in height as a function of annealing time over large sample areas. This allows us for the first time to gather information on the complex interaction between the simple pattern height decay capillary instability (sometimes referred to as "slumping") and the lateral zig-zag capillary instability. We note that time-resolved studies are possible over small sample areas and with

low resolution with AFM but are complicated at the higher temperatures $> 100°C$, due to issues working with a heated substrate including drift, thermal expansion, and thermally dependent tip/substrate interactions.

5.2 Experimental

Polymer line-space gratings with a fluorosurfactant (FS) additive (Zonyl FSG, Dupont) were studied with time-resolved GISAXS during thermal annealing to investigate the development of the zig-zag capillary instability as in Alvine et al [**?**]. The FS additive acts to reduce the adhesion to the imprint mold and typically results in higher quality patterns. Polystyrene (PS) films with a fluorosurfactant (FS) at 3.2 weight % were spun-cast from toluene solutions onto UV ozone cleaned Si wafers. The polystyrene had a narrow molecular weight (Mw) distribution peaked around 19.3 kg/mol (Scientific Polymer Products, Inc). Previously it was found that the FS acted to reduce the surface tension of the polymer from 44 mN/m (pure PS) to 30 mN/m by preferential migration of the surfactant to the surface. Additionally the effective viscosity of the PS/FS system is reduced by a similar factor of 1.5 due to the small molecule nature of the FS additive indicating some partial mixing of excess FS into the PS[14]. At these FS concentrations, the shift in T_g is less than one degree.[14] Additionally, based on this partial mixing and the relatively low fluorine to hydrogen ratio of the FS we do not expect noticeable x-ray contrast between the FS and PS rich areas of the structures.

Line-space gratings (Fig 5.1 a) with a pitch (period) Λ of 424 nm were then formed by thermally embossing the polymer films as shown in Fig 5.1 c-e with a hard silicon oxide mold $40°C$ above the T_g ($\sim 100°C$) of the PS and at elevated pressure of 500 psi, followed by demolding at $55°C$. AFM and Scanning Electron Microscopy (SEM) confirmed the high quality transfer of one-dimensional periodic line-space grating patterns approximately 360 nm in height with nearly one to one line-to-space ratio. These nanoscale patterns offer a simple geometry with which to study the surprisingly complex interplay of capillary forces which can

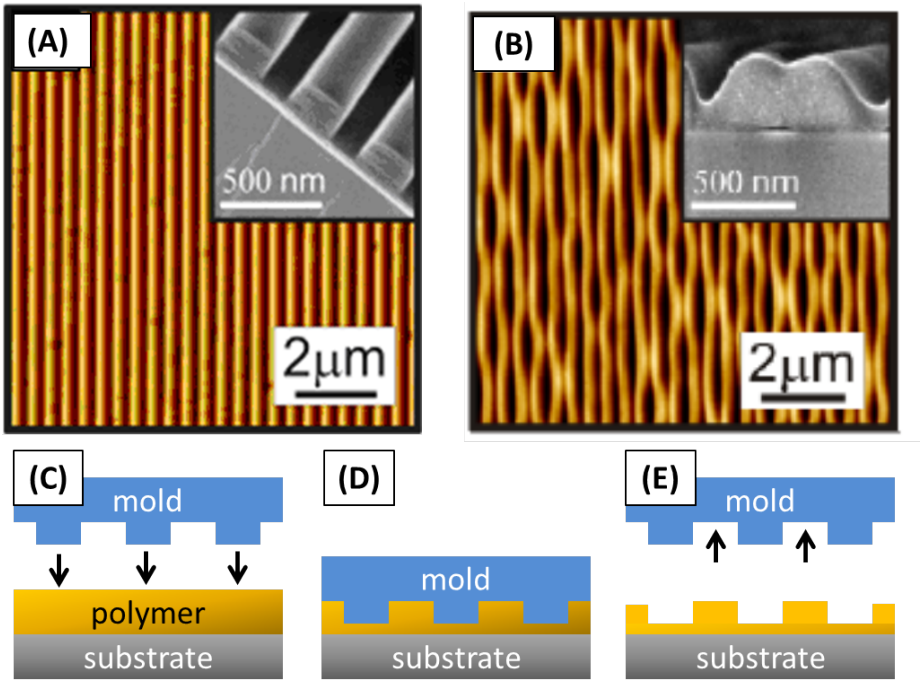

Figure 5.1: (A) AFM data of as-imprinted polystyrene with fluorosurfactant line-space grating. SEM (inset) shows the lines rectangular cross-section at a fractured edge. (B) After annealing the sample for X minutes at Y degrees C, a lateral zig-zag instablilty forms in the pattern. (C-E) Nanoimprint Lithography schematic. (C) a hard nanoscale line-space mold is pressed into the soft polystyrene thin film. (D) At elevated temperatures and applied pressures, the polymer fills the voids in the mold. (E) At ambient temperature and pressure the mold is removed from the polymer leaving the complementary nanoscale relief pattern.

include simple height decay, varicose local height undulations, and lateral zig-zag undulations.

Due to the initial thickness of the polymer thin film an approximately 90 nm thick residual layer of polymer is formed at the bottom of the pattern (see Fig 5.1 e) during imprinting. It is thought that the presence of this residual layer is critical to the formation of the more complex collective zig-zag and other capillary instabilities[14]. Without the residual layer we would expect that annealing leading to classical Raleigh thread break-up of the polymer lines as observed by H. Lee et al [11].

GISAXS experiments were performed at the 8-ID-E beamline [17] of the Advanced Photon Source, Argonne National Laboratory, using monochromatic

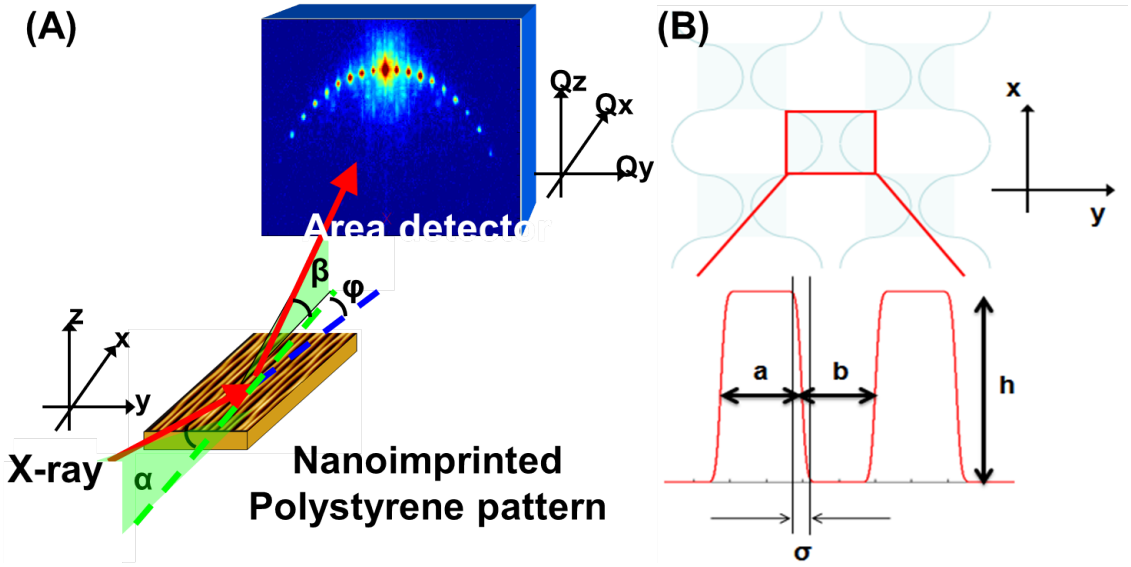

Figure 5.2: (A) Schematic of GISAXS experiemnts. The incident x-ray beam is directed in the plane parallel to the initial nanoscale polymer lines. The incident angle is slightly above the critical angle of the polystyrene to ensure the entire nanoimprinted PS pattern is probed. Time-resolved CCD images are collected during the anneling process. (B) Schematic of the 2-line unit cell analytical model used to fit the GISAXS data.

$(7.35keV)$ x-rays. Nanoimprinted samples were mounted in the reflection geometry with the polymer lines orientated parallel to the plane of the incident x-ray beam as shown illustrated schematically in Fig 5.2 A. The sample chamber was kept under high-vacuum during annealing and all sample measurements to reduce both potential oxidation and air scattering. The sample was placed directly on a Cu heater block for rapid thermal response. The grazing incidence angle, $\alpha = 0.23°$, was set below the critical angle for total external reflection from Si, of $0.24°$, and well above the critical angle for PS of $0.148°$ to insure that the x-ray scattering volume is collected from the entire polymer grating, including the residual layer. The parallel line orientation was confirmed by the observation of symmetric scattering pattern about the specular plane. If the orientation of the lines is misaligned at an angle ($> 0.05°$) with respect to the plane of the incident beam, the intersection of the scattering cone with the Ewald sphere produces a noticeably asymmetric pattern [18]. Thus the sample was aligned by rocking the sample in the horizontal

plane until a highly symmetric scattering pattern is achieved. GISAXS intensity was collected with an x-ray sensitive charge-couple device (CCD) area detector, located 1.72 meters downstream from the sample .

The principle features in the GISAXS are the intense periodic spots that appear due to Bragg-like scattering from the highly periodic line-space grating. Since the grating is quasi-2D, the scattering extends in q_z as a Bragg Truncation Rod (BTR). However, due to the non-zero incident angle, the intersection of the BTR with the Ewald sphere creates an intense arc of high intensity, though the extension of the BTR is still visible [18]. After preliminary alignment the sample was rapidly heated from ambient temperature to 10 degrees below the glass transition temperature T_g ($T_g \approx 100°C$ for this M_w PS) at which point an additional sample re-alignment was performed (whenever necessary) to compensate for rotational and translational misalignment caused by heating the sample. At 10 degrees below T_g, the polymer is still in the glassy state and flow is negligible over the time scales necessary to complete the realignment of the beam. After re-alignment, the sample temperature was then rapidly raised by another $15°C$, to the target temperature of $T_g + 5°C$ at a heating rate of $10°C/min$. Care was taken to minimize the thermal over-shoot of the sample heater, which was aided by the short dwell at $90°C$. Once the target temperature was reached, GISAXS patterns were recorded at the rate of 9 CCD frames/min to allow the collection of in-situ data during the development of the capillary instability (both height decay and zig-zag formation). It should be noted that the time scale of the development of the zig-zag instability and height decay should be highly temperature dependent due to significant decrease in viscosity above T_g. Due to this effect, we can tune, to some degree, the time scale of the capillary instability in order to optimize our measurements within the time resolution of the CCD detector.

5.3 Results and Discussion

A typical progression of the GISAXS intensity with annealing time is shown in Fig 5.3. Before annealing, the combination of the highly periodic nature of

the line-space grating pattern and the high electron density contrast (between the 360 nm tall lines and surrounding air) with low side-wall roughness results in 10 or more orders of the BTR being easily observed. As annealing progresses, long range order in the grating, monitored by the width of the BTR, is unchanged. However, the intensity of higher order peaks rapidly decreases with annealing time. This decrease is due to significant changes in the polymer grating cross-section, which provides a form factor or scattering intensity envelope modifying the intensity of all the diffraction peaks. Changes in form-factor are influenced by rounding of the corners of the pattern, height decay, and the development of the zig-zag pattern. In order to model the lateral motion of the lines during the zig-zag instability development it is necessary to adopt a non-standard unit cell that incorporates two grating lines rather than just one. Thus we model the development of the zig-zag pattern and the subsequent changes in the scattering intensity envelope (form factor) with a two-line unit cell that incorporates relative lateral line motion, roughness increases, and height decay. This relatively simple approach allows us to incorporate both height decay and zig-zag instabilities, including lateral line motion and coalescence. Details follow.

The electron density profile function that we use to model the two-line unit cell accounts for changes in line cross-section and relative lateral motion perpendicular to the lines. As can be seen in Fig 5.1 b, the zig-zag instability results in a quasi-periodic structure where locally two lines come together and coalesce with a corresponding gap opening up on either side. Specifically, the time dependent model is constructed by using two identical boxes of width '$a(t)$' and height '$h(t)$', separated by edge to edge distance $b(t)$, and an interface smearing parameter $\sigma(t)$ (as shown in Fig 5.2 b). The smearing function is applied symmetrically to all line side-walls. The analytical real space profile function is then defined by error functions, $Erf(x)$ as:

$$\rho(y) = \frac{h}{2}[Erf(\frac{y - b/2}{\sigma}) - Erf(\frac{y - b/2 - a}{\sigma}) - Erf(\frac{y + b/2}{\sigma}) + Erf(\frac{y + b/2 + a}{\sigma})] \tag{5.1}$$

The interface smearing parameter σ accounts for rounding of the lines,

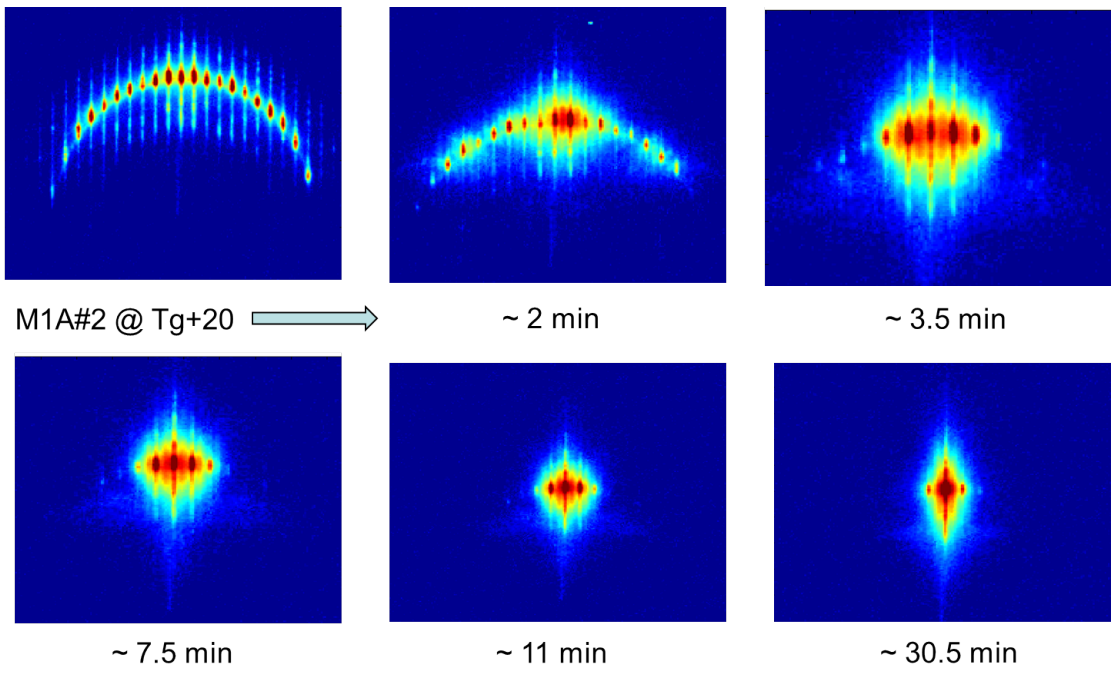

Figure 5.3: Selected points along the time evolution the GISAXS pattern indicating the thermal decay on the sample.

which occurs during annealing, as well as local coalescence of the adjacent lines as they move together. These parameters as a function of annealing time are then determined by fitting the diffraction pattern, the $I(q_y)$ generated from integrating each BTR data set. The diffraction pattern is determind both the form factor from the unit cell and the structure factor of the 1-D grating. The form factor from the electron density profile function of the unit cell can be derived by squaring the Fourier Transform of $\rho(y)$ as:

$$I(q_y)_{form} = \frac{2}{\pi}\frac{h^2 e^{-{q_y}^2\sigma^2/2}}{{q_y}^2\sigma^2}[sin(\frac{bq_y}{2}) - sin(\frac{(2a+b)q_y}{2})]^2 \tag{5.2}$$

Thus, the analytical expression for the diffraction pattern from nanoimprinted polymer grating is given by the product of the form factor and the 1-D grating structure factor:

$$I(q_y)_{diffraction} = I(q_y)_{form} \times \sum_{m=1}^{N/2} cos((2m-1)\Lambda q_y/2) \tag{5.3}$$

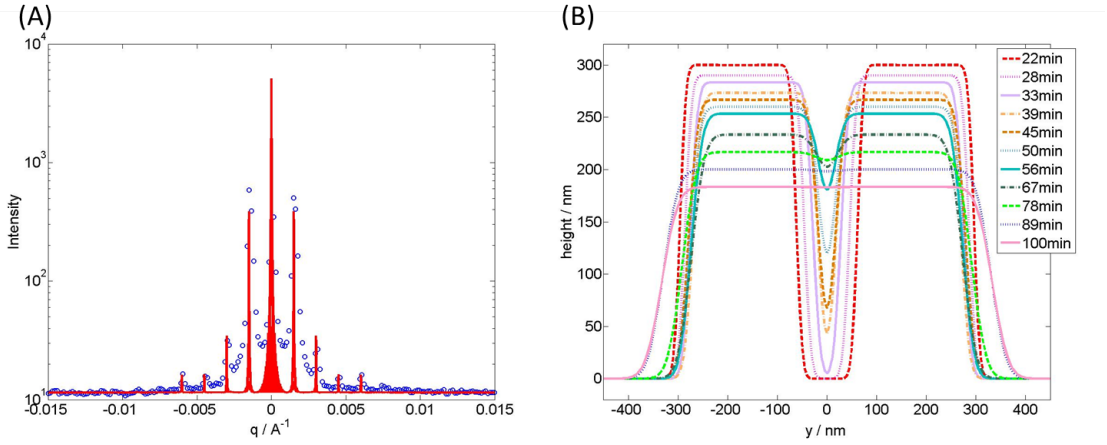

Figure 5.4: (A): an example of the diffraction data with its best fit. (B): the extracted cross-section of the model unit cell shows the thansition from two individual lines of the model unit cell to a locally coalesced unit as annealing progresses.

By fitting the measured diffraction patterns taken during the annealing with this analytical expression I(qy)diffraction, we extract the structural information about the two-line unit cell as a function of annealing time t. Fig 5.4 shows the evolution of the extracted density profile of a model unit cell during the annealing, which confirms that at approximately 20 minutes the zig-zag undulation starts to develop in the sample by the slight periodicly local bending of polymer lines as evidenced by the boxes moving together. After two lines in the unit cell begin moving towards each other, the local coalescing by filling in of the gap between the lines with material. The development of the zigzag instability takes about one hour to complete at this annealing temperature.

To further analyze the fitting results, we plot the fitting parameters, the line width a, line separation b, smearing parameter σ at each stage of the annealing process, as a function of annealing time t, shown in Fig 5.5. It can be seen that the width of the nanoimprinted polymer lines expands from $\sim 220\ nm$ at the beginning of the annealing to $\sim 330\ nm$ when two adjacent lines in one unit cell coalesce and remains relatively stable after the coalescence finish. The constantly increasing of the smearing parameter and the decreasing of the pattern height, as observed and discussed previously [9, 19], may be ascribed to the capillary instability effect which rounds the structure edges and reduces the pattern amplitudes. The separation

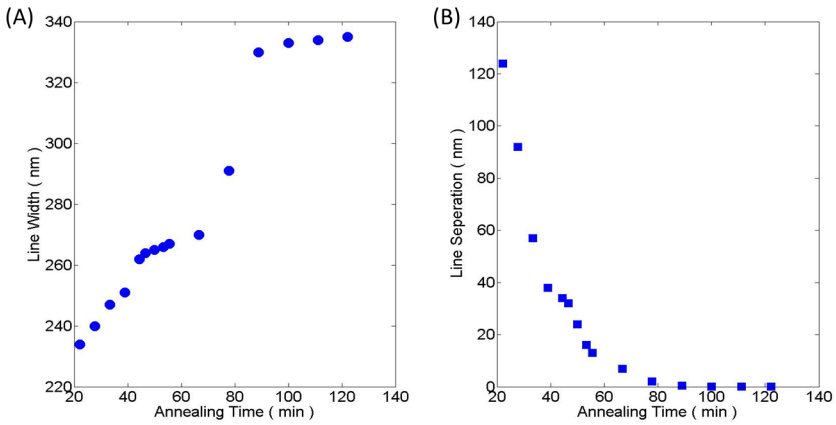

Figure 5.5: (A): the line width a vs.annealing time plot. (B): the line separation b vs.annealing time plot.

between two polymer line shrinks from the original $\sim$ 210 nm to 0 indicating the formation of zig-zag capillary instability and the locally coallescensing of the adjacent lines. Note that the collallescence of two adjacent polymer lines only happens locally not two entire lines connect together all the way through which may doubles the period of the structure, this is suggested by the absence of possible new diffraction peak in between the original orders of diffraction peaks due to the doubling of the period. This can also be seen by the fact that two neighboring lines moving together implies that a gap has developed on either side. After local line coalesceance has occurred and the zig-zag pattern developed, the whole pattern proceeds to decay in height as conventional thermal instability.

5.4 Conclusions

We utilize GISAXS measurements to study the development of a novel instabily on the nano-imprinted pattern. Our measurement provides complimentary information to the previous AFM results about the globle surface structure change of an evolving system with better special and temporal resolution. It is important to extend to this measurement to some smaller lengthscale structures or faster evolving systems. The unit cell model should be modified for different system to be more suitable for describing the structure.

5.5 Acknowledgements

The text of this chapter, in part, is a reprint of the material as it appears in:

Y. Dai, K. J. Alvine, H. Ro, C. L. Soles, J. Strzalka, O.G. Shpyrko, "Development of a Zig-Zag Capillary Instability in Nanoimprinted Polymer Gratings: A Time-Resolved GISAXS Study", in preparation,(2013).

Bibliography

[1] JinKui Chu, FanTao Meng, ZhiTao Han, and Qing Guo. Large area mold fabrication for the nanoimprint lithography using electron beam lithography. *Science in China Series E: Technological Sciences*, 53(1):248–252, January 2010.

[2] Stephen Y. Chou, Peter R. Krauss, and Preston J. Renstrom. Nanoimprint lithography. In *The 40th international conference on electron, ion, and photon beam technology and nanofabrication*, volume 14, pages 4129–4133, Atlanta, Georgia (USA), 1996. AVS.

[3] L. J. Guo. Nanoimprint lithography: Methods and material requirements. *Advanced Materials*, 19(4):495513, 2007.

[4] Heidi B. Cao, Paul F. Nealey, and Wolf-Dieter Domke. Comparison of resist collapse properties for deep ultraviolet and 193 nm resist platforms. In *Papers from the 44th international conference on electron, ion, and photon beam technology and nanofabrication*, volume 18, pages 3303–3307, Rancho Mirage, California, (USA), 2000. AVS.

[5] M.p. Stoykovich, H.b. Cao, K. Yoshimoto, L.e. Ocola, and P.f. Nealey. Deformation of nanoscopic polymer structures in response to well-defined capillary forces. *Advanced Materials*, 15(14):11801184, 2003.

[6] Kyle J. Alvine, Yifu Ding, Jack F. Douglas, Hyun Wook Ro, Brian C. Okerberg, Alamgir Karim, and Christopher L. Soles. Capillary instability in nanoimprinted polymer films. *Soft Matter*, 5:2913–2918, 2009.

[7] Yifu Ding, Hyun Wook Ro, Kyle J. Alvine, Brian C. Okerberg, Jing Zhou, Jack F. Douglas, Alamgir Karim, and Christopher L. Soles. Nanoimprint lithography and the role of viscoelasticity in the generation of residual stress in model polystyrene patterns. *Advanced Functional Materials*, 18(12):18541862, 2008.

[8] Yifu Ding, H. Jerry Qi, Kyle J. Alvine, Hyun Wook Ro, Dae Up Ahn, Sheng Lin-Gibson, Jack F. Douglas, and Christopher L. Soles. Stability and surface

topography evolution in nanoimprinted polymer patterns under a thermal gradient. *Macromolecules*, 43(19):8191–8201, October 2010.

[9] Y. Ding, H. W. Ro, J. F. Douglas, R. L. Jones, D. R. Hine, A. Karim, and C. L. Soles. Polymer viscoelasticity and residual stress effects on nanoimprint lithography. *Advanced Materials*, 19(10):13771382, 2007.

[10] Hyun Wook Ro, Yifu Ding, Hae-Jeong Lee, Daniel R. Hines, Ronald L. Jones, Eric K. Lin, Alamgir Karim, Wen-li Wu, and Christopher L. Soles. Evidence for internal stresses induced by nanoimprint lithography. volume 24, pages 2973–2978. AVS, 2006.

[11] Jeong-yong Park, Kahp Y Suh, Soon-min Seo, and Hong H Lee. Anisotropic rupture of polymer strips driven by rayleigh instability. *The Journal of chemical physics*, 124(21):214710, June 2006. PMID: 16774434.

[12] Chung-Yen Chao and L.J. Guo. Reduction of surface scattering loss in polymer microrings using thermal-reflow technique. *IEEE Photonics Technology Letters*, 16(6):1498–1500, 2004.

[13] R.K. Dutta, J.A. van Kan, A.A. Bettiol, and F. Watt. Polymer microlens replication by nanoimprint lithography using proton beam fabricated ni stamp. *Nuclear Instruments and Methods in Physics Research Section B: Beam Interactions with Materials and Atoms*, 260(1):464–467, July 2007.

[14] K. J. Alvine, Y. Dai, H. W. Ro, S. Narayanan, A. R. Sandy, C. L. Soles, and O. G. Shpyrko. Capillary wave dynamics of thin polymer films over submerged nanostructures. *Phys. Rev. Lett.*, 109:207801, Nov 2012.

[15] Kyle J. Alvine, Yifu Ding, Jack F. Douglas, Hyun Wook Ro, Brian C. Okerberg, Alamgir Karim, Kristopher A. Lavery, Sheng Lin-Gibson, and Christopher L. Soles. Effect of fluorosurfactant on capillary instabilities in nanoimprinted polymer patterns. *Journal of Polymer Science Part B: Polymer Physics*, 47(24):2591–2600, 2009.

[16] J. R. Levine Parrill, P. Georgopoulos, Y.-W. Chung, and J. B. Cohen. GISAXS - glancing incidence small angle x-ray scattering. *Le Journal de Physique IV*, 03(C8):C8–411–C8–417, December 1993.

[17] Alec R. Sandy, L. B. Lurio, S. G. J. Mochrie, A. Malik, G. Brian Stephenson, and Mark Sutton. Production and characterization of x-ray speckle at sector 8 of the advanced photon source. volume 3154, pages 27–38, 1997.

[18] Minhao Yan and Alain Gibaud. On the intersection of grating truncation rods with the ewald sphere studied by grazing-incidence small-angle x-ray scattering. *Journal of Applied Crystallography*, 40(6):1050–1055, November 2007.

[19] Ronald L Jones, Tengjiao Hu, Christopher L Soles, Eric K Lin, Ronald M Reano, Stella W Pang, and Diego M Casa. Real-time shape evolution of nanoimprinted polymer structures during thermal annealing. *Nano letters*, 6(8):1723–1728, August 2006. PMID: 16895363.

6 A comparative study of Langmuir Surfactant Films: Grazing Incidence X-ray Off-Specular Scattering vs. X-ray Specular Reflectivity

Surface monolayers assembled on liquid sub-phase represent a class of systems that is of great interest for studies of phase transitions in quasi-2D systems, chemical self-assembly, surfactant behavior and biologically relevant monolayers and membranes. X-ray scattering is ideal for studying structural, dynamic and mechanical properties of these surface monolayers at nanoscale due to penetrating ability and short wavelength of x rays. We show here that Grazing Incidence X-ray Off-Specular (GIXOS) scattering provides rapid access to in-plane and out-of-plane nanoscale structure, surface fluctuating modes, and potentially bending stiffness. We show that analysis of GIXOS data is highly sensitive to resolution effects. We further present detailed analysis of GIXOS from phospholipid 1,2-dipalmitoyl-phosphatidyl-choline $C_{40}H_{80}NO_8P$ (DPPC) and obtain quantitative, Ångström-resolution details of electron density profile normal to the surface that is comparable to those that are obtained from specular x-ray reflectivity measurements. We compare these GIXOS results to X-ray Reflectivity measurements performed on the same samples. While electron density and main structural char-

acteristics (such as monolayer thickness) obtained by GIXOS agree with X-ray reflectivity results, the interfaces of GIXOS-derived density profiles are found to be systematically sharper than those obtained with X-ray reflectivity. The possible reasons for these differences are discussed.

6.1 Introduction

From the physics point of view, the liquid-air interfaces represent a quasi-2D system with a rich phase diagram and often unusual properties not observed in the bulk. From the chemistry viewpoint, liquid-air interfaces present a unique playground for chemical self-assembly of surfactant molecules or nanoscale objects. Finally, from the biology perspective, the Langmuir monolayers [1] represent an idealized model of biological systems, such as lung surfactants and biomembranes [2, 3, 4]. Synchrotron-based x-ray scattering techniques are ideally suited for studies of liquid-air interfaces due to the penetrating ability of x ray photons and the ability to couple to structural and dynamic properties of the interfaces with nanoscale, or often even Angstrom-level resolution [5].

X-ray specular reflectivity is directly related to the electron density distribution of the interface along the surface normal. X-ray Reflectivity (XR) measurement involves simultaneous varying both incident and reflection angles while preserving the specular condition ($\alpha = \beta$, $\theta = 0$, see Figure 6.1) [6, 7, 8]. Because the free liquid surface must remain horizontal during the measurement XR scan must involve lowering and raising the sample, possibly disturbing the surface. During the motion of the Bragg steering crystal that is used to deflect the beam downward, the sample and detector arm both have to also move laterally during XR scan. Since XR signal even from ideally flat surface (Fresnel reflectivity law) falls off as the inverse of the fourth power of the wavevector transfer, the measurements extending out to large wavevector transfers often require long counting time, and careful background subtraction of bulk scattered signal. As a result, a typical XR scan takes a fairly long period of time - on the order of an hour or more, disturbs the monolayer due to vertical and lateral motion of the sample,

and includes substantial changes in the x-ray footprint on the sample, therefore probing different regions of the surface. Additionally, since any x-ray reflectivity measurement includes diffuse scattering from thermally excited capillary waves decorating the free surface of any liquid, a quantitative understanding of the intrinsic structural properties of the monolayer from XR scan requires additional diffuse scattering measurements performed in off-specular geometry, making these measurements even more painstaking.

Grazing incidence X-ray off-specular scattering (GIXOS) [9] has been recently proposed as an attractive alternative to XR for structural characterization of interfaces along surface-normal with sub-nanometer resolution [10, 11]. Due to grazing incidence geometry, GIXOS is highly sensitive to surface roughness induced by the thermally excited capillary fluctuations at interface and the structure within the x-ray penetration depth defined by the evanescent x-ray wave, typically on the order of 3 nm. In contrast to the complex motions of sample, steering crystal and detector arms required for XR scan, GIXOS data can be collected during a single exposure with an area detector in a fixed geometry, with no motion of steering crystal, sample or detector required. Additionally, the use of the grazing incidence geometry minimizes the x-ray induced sample damage effect. This makes GIXOS an ideal technique for in-situ studies of the structural and dynamic properties of liquid-air interfaces during, for example, adsorption isotherms or other phase transitions. Previously GIXOS was used to provide semi-qualitative results about typical thickness of the monolayer. A quantitative approach requires isolating the diffuse scattering diffuse scattering arising from thermally induced capillary fluctuations, convolved with experimental resolution function. Here we demonstrate that such detailed analysis of GIXOS is capable of providing quantitative, Angstrom-resolution details of intrinsic electron density profile normal to the surface with the quality that is comparable to what can be routinely obtained through a more lengthy XR measurement.

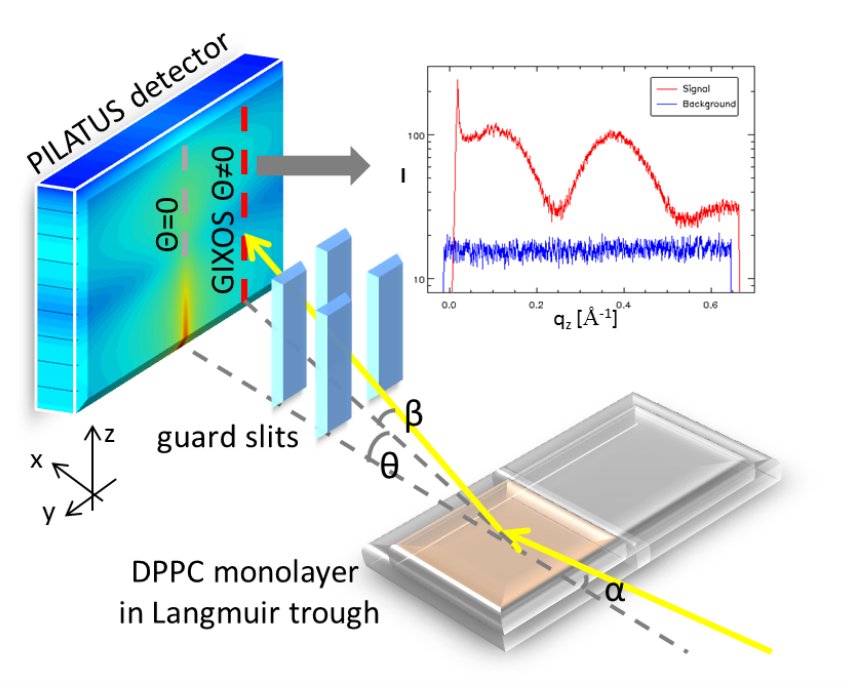

Figure 6.1: Schematic view of the scattering geometry with the Langmuir trough. X-rays are incident at the liquid-air interface at grazing incidence α. Off-specular scattering is detected by PILATUS area detector simultaneously for a wide range of β at a specific azimuthal angle θ, along the trajectory indicated with red dashed line. An inset shows a typical intensity profile(red), together with measured background(blue), plotted as function of wavevector transfer normal to the surface, q_z.

6.2 Experimental Details

The x-ray scattering experiments were carried out at ChemMATCARS beamline [12] 15-ID at Advanced Photon Source (APS), Argonne National Laboratory, using monochromatic x-rays of energy 10 keV. The GIXOS experimental geometry is illustrated schematically in Figure 6.1. X-ray incidence angle was below the critical angle ($\alpha = 0.1°$) for total external reflection, thus making the scattering from the bulk water substrate negligible. The scattering patterns were collected in fixed geometry for a wide range of output angles β (0° to 7.3°), covering q_z from -0.055 $\AA^{-1}$ to 0.647 $\AA^{-1}$, for an azimuthal angle $\theta = 0.4°$ with a two-dimensional hybrid pixel array x-ray detector, Pixel Apparatus for the Swiss Light Source (PI-

LATUS 100K) [13], which operates in single-photon counting mode. The pixel size of the PILATUS is 172 $\mu m \times 172$ μm, and the active area of the detector is 33.5 mm (horizontally) $\times$ 83.8 mm (vertically). The detector was located 570 mm downstream from the sample. In order to reduce the small-angle scattering from the specular reflection of the surface and the background scattering from the upstream Kapton window of the Langmuir trough, two sets of guard slits were placed 300 mm downstream from the sample and directly against the PILATUS, respectively. Both sets of the slits were open at 0.12 mm horizontally and 100 mm (wide open) vertically, limiting the azimuthal acceptance to $\Delta\theta = 0.03°$. The scattering signal detected by a pixel on the area detector corresponds to a specific spot on the Ewald's sphere in the reciprocal,q, space, because the q value for each pixel can be determined from the scattering geometry.

The lipid monolayers were prepared by spreading phospholipid 1,2-dipalmitoyl-phosphatidyl-choline $C_{40}H_{80}NO_8P$ (DPPC) chloroform solution onto the ultrapure water surface in a Langmuir trough and compressing the monolayer with the motorized barrier to a target surface pressure of 30 mN/m. The density distribution of the DPPC monolayer formed by this process is considered isotropic and fairly homogeneous within the x-y plane across the whole sample. The surface pressure was monitored in-situ with Wilhelmy plate. During the x-ray measurements, the Langmuir trough was periodically translated horizontally, normal to the plane of incidence, in order to minimize long-term radiation damage due to overexposing the same spot on the sample. The typical timescale on which degradation of the monolayer has become noticeable with x-ray scattering was on the order of 5 minutes. The typical GIXOS data together with the measured background for our DPPC monolayer sample is shown in the inset of the Figure 6.1. In data analysis, GIXOS data were normalized to the intensity I_n at first minimum. This normalization was chosen because the GIXOS data are often unreliable near/below critical angle due to glancing incidence geometry, and thus normalization of GIXOS is best performed at the first minimum, a region that is highly reproducible. The corresponding XR data were taken back to back with the GIXOS measurements on the same sample.

We measured the residual scattering background from the small angle scattering and the trough windows by lowering the trough, so that the x-ray beam passed above the liquid surface, and, at the meantime, lowering the PILATUS detector correspondingly by 2α, so that the pixel that was measuring the specular reflection (i.e. $\beta = \alpha$) when the sample was in place was measuring the direct beam (i.e. $\beta = -\alpha$) when the trough was out of the direct beam path. This background was subtracted from all the data shown here.

6.3 Results and Discussion

Off-specular x-ray scattering from liquid-air interfaces is typically dominated by the diffuse scattering due to thermally excited capillary wave fluctuations14-16. These excitations effectively roughen the surface and result in off-specular diffuse x-ray scattering. The height fluctuations of surface can be characterized by their statistical average and Sinha et al. [14] have shown that integration over these height fluctuations yields the following dependence of the scattering on the in-plane and surface-normal components of the wavevector transfer $\mathbf{q}_{xy}$ and q_z:

$$\int_{|\mathbf{r}_{xy}|>a} d^2\mathbf{r}_{xy} exp\{\frac{{q_z}^2}{2}\langle[z(\mathbf{r}_{xy}) - z(0)]^2\rangle\} exp[i\mathbf{q}_{xy}\cdot\mathbf{r}_{xy}] = \frac{1}{{q_{max}}^{\eta}}\frac{4\pi^2}{{\mathbf{q}_{xy}}^{2-\eta}} \qquad (6.1)$$

where $\eta = \frac{k_B T}{2\pi\gamma}{q_z}^2$ is the capillary exponent and q_{max} is the upper wavevector cutoff related to atomic size a ($q_{max} = \pi/a$). Therefore, unlike the specular signal obtained from a flat solid surface, which is dominated by the delta functions and is not sensitive to the angular acceptance of the resolution function, the specular signal from a liquid surface will generally depend on the resolution function. For diffuse scattering from the liquid surface, the off-specular signal falls off as $1/{q_{xy}}^{2-\eta}$, which gives liquid diffuse scattering a strong resolution effect. Incorporating the resolution effects thus especially crucial for the study of liquid surfaces [15]. Equation 6.1 leads us to the expression of the scattering differential cross-section: the intensity measured at a specific scattering vector is obtained by integrating the differential cross-section over the solid angle $d\Omega$ defined by the detector acceptance of the measurement:

$$\frac{I}{I_0} = \frac{1}{A_0}\int_{res}\frac{d\sigma}{d\Omega}d\Omega = \frac{1}{k^2\sin\alpha\sin\beta}(\frac{q_c}{2q_z})^4\frac{\eta {q_z}^2}{8\pi}|\Phi(q_z)|^2|t^{in}|^2|t^{sc}|^2\int_{res}\frac{1}{{\mathbf{q}_{||}}^2}(\frac{\mathbf{q}_{||}}{q_{max}})^{\eta}d^2\mathbf{q}_{||} \tag{6.2}$$

where wavevector transfer $k = 2\pi/\lambda$, I_0 and A_0 are the intensity and the illumination area of the incident x-ray beam, α and β is the incident and scattering angle, q_c and q_{max} are the critical wavevector and upper wavevector cutoff, γ is the surface tension of the sample, while t^{in} and t^{sc} are the Fresnel transmission coefficient between air and water, t^{sc} is responsible for the low angle scattering peak (the so-called Yoneda peak). The structure factor $|\Phi(q_z)|^2$ is defined by the in-plane average of the intrinsic electron ρ density along the surface normal:

$$|\Phi(q_z)|^2 = \frac{1}{\rho_\infty}\int dz\frac{\rho(z)}{dz}exp(iq_z z) \tag{6.3}$$

The models that use differential scattering cross-section predicted by the thermal capillary wave theory [16, 17] have been previously shown to be highly successful for a wide range of liquid surfaces [18, 19].

Even though during GIXOS measurements both in-plane ($\mathbf{q}_{xy}$) and surface-normal (q_z) components of the wavevector transfer are varied, the $\mathbf{q}_{xy}$-dependence of the scattering cross-section is encoded in contributions from thermal capillary waves contained under the integral in Equation 7.1. If the liquid surface can be treated as homogeneous and isotropic, and if we were to neglect any variations in in-plane structure factor over the generally small range of $\mathbf{q}_{xy}$ values involved in the GIXOS scan, then the structure factor squared, $|\Phi(q_z)|^2$, can be unambiguously determined from the GIXOS analysis.

One approach to analysis of x-ray surface scattering data is to not separate the capillary contributions from the specular reflection, producing effectively smeared out interfacial electron density profiles due to thermal capillary fluctuations. However, since the degree of the thermal roughening depends on the experimental resolution function, measurements on identical samples using different resolution settings are bound to produce different density profiles. If the effect of thermal capillary wave fluctuation is considered separately, as is done here, the resulting electron density profile is the intrinsic property of the sample, independent

of experimental details such as detector resolution [18, 19].

The measured x-ray scattering intensity at a specific value of scattering wavevector transfer $\mathbf{q}$ ($q_x = \frac{2\pi}{\lambda}(\cos\beta\cos\theta - \cos\alpha)$, $q_y = \frac{2\pi}{\lambda}\cos\beta\sin\theta$, $q_z = \frac{2\pi}{\lambda}(\sin\alpha+\sin\beta)$) is then proportional to the integration of differential cross-section over resolution function.

In calculating the experimental resolution effects we assume that the x-ray beam incident on the liquid surface is essentially monochromatic and highly collimated vertically, which is a reasonable assumption for x-ray generated at third generation synchrotron sources such as APS ($\Delta E/E \approx 10^{-4}$, $\Delta\alpha \approx 2\times10^{-5}\ rad$). The resolution function is primarily defined by the footprint projection of the x-ray beam and the detector pixel size. The projection of the detector resolution onto the x-y plane can be approximated by a rectangular shape and the integral of the scattering cross-section over the rectangular resolution area is typically done numerically in our analysis. We make the simplification to assume the intensity of the x-ray beam is sharply terminated at the boundary of the resolution function, however, the resolution function could also be in principle described by "soft edge" boundary with intensity falling off gradually as the boundary is crossed.

A rectangular detector resolution is defined by pairs of horizontal and vertical slits. A pair of vertical slits with an opening of $2V$ (electronic slit V = 0.94 mm for XR measurement) and horizontal slits with an opening of $2H$ (electronic slit H=1.98 mm for XR measurement and guard slits H = 0.06 mm for GIXOS) would accept scattering angles ranging from $\beta - \Delta\beta$ to $\beta + \Delta\beta$ vertically and $\theta - \Delta\theta$ to $\theta + \Delta\theta$ horizontally, where $\Delta\beta$ and $\Delta\theta$ are defined in small angle approximation ($\Delta\beta, \Delta\theta \ll 1$) as $\Delta\theta = V/L$, $\Delta\theta = H/L$. Here L = 0.57 m is the distance from the center of the sample to the position of the detector. The projection of resolution function in q_xy space is the rectangle of the size $2\Delta Q'_x$ by $2\Delta Q'_y$, with sides along Q'_x and Q'_y axis which are rotated by angle θ with respect to q_x and q_y. The dimensions of the rectangular resolution function projected onto horizontal plane are given by:

$$\Delta Q_x = \frac{2\pi}{\lambda}\Delta\beta\sin\beta = \frac{2\pi}{\lambda}\frac{V}{L}\sin\beta,\ \Delta Q_y = \frac{2\pi}{\lambda}\Delta\theta\cos\beta = \frac{2\pi}{\lambda}\frac{H}{L}\cos\beta \qquad (6.4)$$

Note that $\Delta Q'_x\Delta Q'_y/(k^2\sin\beta)$ recovers the solid-angle acceptance $\Delta\beta\Delta\theta\cos\beta$. If

we assume that the detector accepts all radiation for which q_{xy} falls within this rectangular shape and rejects all that falls outside, scattering intensity can be calculated by integrating differential cross section over this rectangular area in **q** space. Since in practice beam-defining slits also contribute for defining resolution function, corrections to the calculation of $\Delta\beta$ and $\Delta\theta$ need to be made to obtain effective opening range of angles. The footprint effect has also been carefully taken into account. The scattering from each point of the sample within the footprint of the x-ray beam contributes to the intensity at every solid angle accepted by the detector, but at different values of output angle β for various points on the sample. An integration of intensity over the footprint area needs to be calculated to obtain the overall scattering intensity.

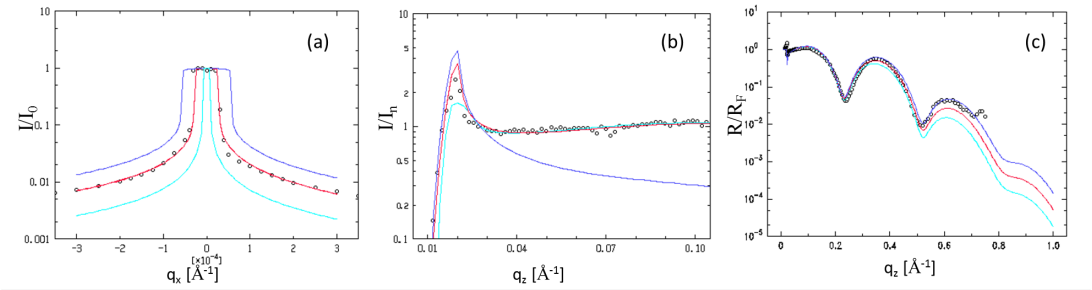

Figure 6.2: Effects of detector resolution in simulated (a) diffuse scattering (K-scan), normalized to the specular reflection intensity I_0; (b) GIXOS scan, normalized to the intensity In at the first minimum at $q_z \approx 0.03$ $\mathring{A}^1$; and (c) XR scan, normalized to the Fresnel Reflectivity R_F. Error bars are smaller than symbol size.

The simulated resolution effects for three different kinds of surface-scattering measurements for DPPC monolayer are illustrated in Figure 6.2 with experimental data (shown as black dots) taken with the same slits setting as that of red simulation curve. The left panel of the Figure 6.2 shows rocking scans (K-scan), obtained by varying both α and β to scan q_y while keeping both q_x and q_z constant at $q_x = 0$ and $q_z = 0.33$ $\mathring{A}^{-1}$. The simulations are shown for three sets of detector slits (horizontal vertical) = (1.89 $mm \times 1.04$ mm) - blue line, (1.89 $mm \times 0.52$ mm) - red line and (1.89 $mm \times 0.172$ mm) cyan. This plot illustrates that due to the integration of the function $1/q_{xy}^{2-\eta}$ over the region that does not contain singularity at $q_{xy} = 0$, the measured diffuse scattering profile is highly sensitive to the dimensions

resolution function. Note that the slit size roughly define the width of the specular reflectivity peak (central peak at $q_y = 0$). The middle panel shows the GIXOS data for three sets of beam slits (horizontal vertical) = ($0.3\ mm \times 0.012\ mm$) - blue line, ($0.3\ mm \times 0.12\ mm$) - red line and ($0.3\ mm \times 1.2\ mm$) cyan. Coarser resolution function defined by wide open slits causes the smearing of details of the features of scattering signal. In the case of GIXOS smearing of detailed features of scattering intensity around critical angle is more pronounced, making GIXOS scattering at low q_z more sensitive to resolution function, while the opposite is true for XR measurements, which become more sensitive to resolution at large q_z. The right panel shows XR measurements and simulations for three sets of detector slits (horizontal $\times$ vertical) = ($3.89\ mm \times 5.67\ mm$) - blue line, ($3.89\ mm \times 1.89\ mm$) - red line and ($3.89\ mm \times 0.63\ mm$) - cyan. The XR at low q_z doesnt depend strongly on slit sizes, since at small q_z the singularity of function $1/q_{xy}^{2-\eta}$ within the integrated area dominates the scattering intensity. At large q_z the capillary exponent increases, reducing the relative contribution of singularity at $q_{xy} = 0$, compared to the off-specular scattering, therefore making the total integral more strongly dependent on the size of the resolution function.

Since many x-ray reflectivity routines do not consider capillary contributions separately and therefore result in convolution of the intrinsic density profile with capillary roughening, we have performed the comparison with our code by turning off resolution effects (by setting temperature to zero or surface tension to infinity). The resulting thermally roughened (and generally speaking, resolution-dependent) density profile agrees with the profiles obtained from model-independent fitting routines, an indication that our reflectivity fitting routine is valid.

To establish the quantitative viability of GIXOS measurement, GIXOS and XR measurement was first done on bare water surface which presents the ideal, simplest structureless liquid-air interface. In Figure 6.3(a) we present the R/R_F and GIXOS results simulated from electron density for water surface (Figure 6.3(b)). A simple structureless density profile was used to fit the experimental data for both XR and GIXOS exceptionally well.

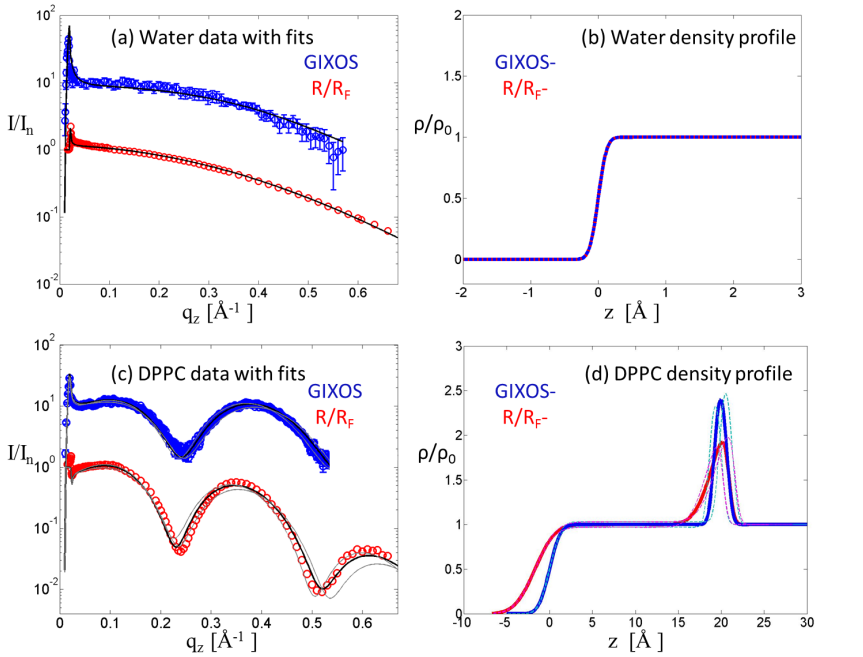

Figure 6.3: (a) R/R_F from XR measurement and GIXOS from raw GIXOS data with background subtraction for bare water surface and the respective fits. (b) Corresponding electron density profiles obtained from the theoretical fits for water surface. (c) R/R_F and GIXOS for DPPC monolayer and the respective fits. (d) Corresponding electron density profiles obtained from the theoretical fits for DPPC monolayer. Error bars are smaller than the symbol size for R/RF data. GIXOS data was normalized to the intensity In at first minimum and GIXOS curve is shifted in intensity for clarity. Gray lines in (c) correspond to the XR/GIXOS fits resulting from varying the fitting parameters by $\pm 3\%$. Dashed lines in (d) are the density profiles corresponding to gray lines fitting in (c).

The XR data for DPPC on water was fitted to the simple two-box density model routinely used to describe the layers for the lipid head-groups and tails. The extracted electron density profile confirmed that DPPC monolayer film was formed at the air-water interface. To refine the fits, the density of the first box was fixed to the known density of DPPC tails. The experimental XR data and the best fits are shown in the Figure 6.3(d): the density profile clearly shows the high electron density part representing the head groups of DPPC lipid molecules and relatively low electron density of the molecular tails, as has been demonstrated previously. We demonstrate the sensitivity of the fitting in Figure 6.3(c) by plotting

the XR/GIXOS fits resulting from varying all the fitting parameters by ±3% in grey lines. However, it is worth noting that several of the 7 fitting parameters (2 for density, 2 for thickness and 3 for roughness) are coupled and the fit is generally found to be most sensitive to the interfacial roughness parameters.

As shown in Figure 6.3(c)-(d) analysis of our GIXOS data done on the same DPPC monolayer sample indicates that GIXOS can provide similar electron density profile along the surface normal. However, each interface (air/lipid-tails, lipid-tails/lipid-head-group, and lipid-head-group/water) obtained from GIXOS analysis is significantly sharper than that obtained from XR analysis.

We stipulate several possible reasons for the discrepancy in the sharpness of the electron density interfaces obtained from the two techniques. Since XR measures the scattering signal over a small resolution-defined region near $q_{xy} = 0$, while GIXOS is taken at finite q_{xy}, the two techniques access differently averaged surface-normal profiles XR corresponds to density profile averaged over length-scales defined by the inverse of the resolution function, in our case roughly defined as $1/\Delta Q_y \approx 110\ nm$ along y-direction and $1/\Delta Q_x \approx 10\ nm$ along x-directions along the surface, while GIXOS couples to the electron density profile average over $1/q_{xy} \approx 3\ nm$. While laterally homogeneous samples should produce identical averaging results, a film consisting of domains or other types of lateral inhomogeneities would produce different electron density profiles for XR and GIXOS.

6.4 Conclusion

We have demonstrated that properly accounting for the contribution from thermal capillary waves allows for quantitative analysis for GIXOS measurements. This analysis result in density profile that is comparable to those that are obtained from XR measurements. However, the interfaces of GIXOS-derived density profiles are found to be systematically sharper than those obtained from widely accepted analysis of XR measurements performed on the same samples. These differences could be related to lateral inhomogeneity of the interfacial monolayers, and could also be potentially a signature of bending stiffness of the monolayer that effectively

suppresses the capillary fluctuations on the short-wavelength end of the spectrum. While GIXOS employed in parallel data collection mode using an area detector provides a rapid appealing alternative to often painstakingly slow XR measurements, the differences in interfacial roughness discussed in this paper may need to be addressed before quantitative GIXOS measurements become widely accepted.

6.5 Acknowledgements

The text of this chapter, in full, is a reprint of the material as it appears in:

Y. Dai, B. Lin, M. Meron, K. Kim, B. D. Leahy and O. G. Shpyrko, "A comparative study of Langmuir Surfactant Films: Grazing Incidence X-ray Off-Specular Scattering vs. X-ray Specular Reflectivity", *J. Appl. Phys.*, 110, 2011.

Bibliography

[1] H Möhwald. Surfactant layers at water surfaces. *Reports on Progress in Physics*, 56(5):653, 1993.

[2] Vladimir M. Kaganer, Helmuth Möhwald, and Pulak Dutta. Structure and phase transitions in langmuir monolayers. *Rev. Mod. Phys.*, 71:779–819, Apr 1999.

[3] Luka Pocivavsek, Shelli L. Frey, Kapilanjan Krishan, Kseniya Gavrilov, Piotr Ruchala, Alan J. Waring, Frans J. Walther, Michael Dennin, Thomas A. Witten, and Ka Yee C. Lee. Lateral stress relaxation and collapse in lipid monolayers. *Soft Matter*, 4:2019–2029, 2008.

[4] Jan Kmetko, Alokmay Datta, Guennadi Evmenenko, Mary K. Durbin, Andrew G. Richter, and Pulak Dutta. Ordering in the subphase of a langmuir monolayer: x-ray diffraction and anomalous scattering studies. *Langmuir*, 17(16):4697–4700, 2001.

[5] Jens Als-Nielsen, Didier Jacquemain, Kristian Kjaer, Franck Leveiller, Meir Lahav, and Leslie Leiserowitz. Principles and applications of grazing incidence x-ray and neutron scattering from ordered molecular monolayers at the air-water interface. *Physics Reports*, 246(5):251–313, October 1994.

[6] L. Bosio, J.J. Benattar, and F. Rieutord. X-ray reflectivity of a langmuir monolayer on water. *Revue de Physique Applique*, 22(8):4, 1987.

[7] C. A Helm, H Mhwald, K Kjr, and J Als-Nielsen. Phospholipid monolayer density distribution perpendicular to the water surface. a synchrotron x-ray reflectivity study. *Europhysics Letters (EPL)*, 4(6):697–703, 1987.

[8] S. Mora, J. Daillant, D. Luzet, and B. Struth. X-ray surface scattering investigation of langmuir films: Phase transitions and elastic properties. *Europhys. Lett.*, 66(5):694–700, 2004.

[9] Robert Dalgliesh. Application of off-specular scattering of x-rays and neutrons to the study of soft matter. *Current Opinion in Colloid & Interface Science*, 7(3-4):244–248, 2002.

[10] L. Wiegart, S. M. O'Flaherty, P. Terech, and B. Struth. Observation of the desorption of mineral nanoparticles from a hybrid langmuir monolayer: an in situ grazing incidence x-ray (GIXOS) study. *Soft Matter*, 2(1):54, 2006.

[11] Sen M. O'Flaherty, Lutz Wiegart, Oleg Konovalov, and Bernd Struth. Observation of zinc phthalocyanine aggregates on a water surface using grazing incidence x-ray scattering. *Langmuir*, 21(24):11161–11166, November 2005.

[12] The liquid surface/interface spectrometer at chemmatcars synchrotron facility at the advanced photon source. *Physica B: Condensed Matter*, 336(12):75 – 80, 2003. ¡ce:title¿Proceedings of the Seventh International Conference on Surface X-ray and Neutron Scattering¡/ce:title¿.

[13] M. Meron, J. Gebhardt, H. Brewer, J. P. Viccaro, and B. Lin. Following transient phases at the air/water interface. *The European Physical Journal Special Topics*, 167(1):137–142, 2009.

[14] S. K. Sinha, E. B. Sirota, S. Garoff, and H. B. Stanley. X-ray and neutron scattering from rough surfaces. *Physical Review B*, 38(4):2297–2311, August 1988.

[15] P. S. Pershan. X-ray scattering from liquid surfaces: Effect of resolution. *The Journal of Physical Chemistry B*, 113(12):3639–3646, March 2009.

[16] A. Braslau, P. S. Pershan, G. Swislow, B. M. Ocko, and J. Als-Nielsen. Capillary waves on the surface of simple liquids measured by x-ray reflectivity. *Physical Review A*, 38(5):2457–2470, 1988.

[17] P. S. Pershan. Effects of thermal roughness on x-ray studies of liquid surfaces. *Colloids and Surfaces A: Physicochemical and Engineering Aspects*, 171(1-3):149–157, October 2000.

[18] Oleg Shpyrko, Patrick Huber, Alexei Grigoriev, Peter Pershan, Ben Ocko, Holger Tostmann, and Moshe Deutsch. X-ray study of the liquid potassium surface:structure and capillary wave excitations. *Physical Review B*, 67(11):115405, March 2003.

[19] Oleg Shpyrko, Masafumi Fukuto, Peter Pershan, Ben Ocko, Ivan Kuzmenko, Thomas Gog, and Moshe Deutsch. Surface layering of liquids: The role of surface tension. *Physical Review B*, 69(24), 2004.

7 Synchrotron X-ray studies of Rapidly Evolving Morphology of Self-assembled Nanoparticle Films under Lateral Compression

Interfacial nanostructures represent a class of systems that are highly relevant to the studies of quasi-2D phases, chemical self-assembly, surfactant behavior and biologically relevant membranes. Previous studies have shown that under lateral stress a Langmuir film of gold (Au) nanoparticles assembled at liquid-air interface exhibits rich mechanical behavior: it undergoes a rapid structural and morphological evolution from a monolayer to a trilayer via an intermediate hash-like phase. We report the results of studying this structural evolution using Grazing Incidence X-ray Off-Specular scattering (GIXOS). We utilize GIXOS to obtain a quantitative mapping of electron density profile normal to the liquid surface with a sub-nanometer resolution and follow the structural evolution of the Au nanoparticle film under lateral compression with a sub-minute temporal resolution. As the surface pressure is increased, the self-assembled nanoparticle monolayer first crinkles into a double-layer phase before forming a trilayer. This study reveals the existence of a transient bilayer phase and provides microscopic picture of the particle-level crinkling phenomena of ultrathin films. These studies were previously impossible due to relatively short time scales involved in crinkling formation of these transient phases and their intrinsically inhomogeneous nature.

7.1 Introduction

Interfacial films assembled at liquid-air interface are of great interest for the studies of quasi-2D phases, chemistry self-assembly and biological membranes [1, 2, 3, 4, 5, 6]. The solvent evaporation and Langmuir-Blodgett (LB) techniques have been widely used to create 2D self-assembled lipid or nanoparticle films on liquid surfaces [7, 8, 9, 10]. When compressed by the Langmuir trough barrier(s), the lipid/nanoparticle films self-assembled at liquid-air interface exhibit rich elastic and mechanical behaviors [11, 12, 13, 14, 15], determined by the mechanical properties of the molecules/nanoparticles as well as the thermodynamic properties of the interface. The structural evolution of 2D self-assembled gold (Au) and silver (Ag) nanoparticle LB films on liquid interface upon lateral compression has been previously studied using optical microscopy, Atomic Force Microscopy (AFM) and liquid surface X-ray scattering [16, 17, 18, 19]. It was previously reported that many factors, such as the particle sizes, size distributions, compression rates and the type of the ligands of the nanoparticles, affect the kinetics of the films collapsing into multilayers when compressed beyond its monolayer surface pressure [20, 21, 22]. Upon lateral compression, films of Au nanoparticles ($d \sim 2\ nm$, $\sim 25\%$ polydispersed) were found to undergo a continuous phase transition from a homogeneous monolayer phase to a "buckled" bilayer phase [23]. In the investigation of the monolayer of Ag nanoparticles ($d \sim 3.6\ nm$, $\sim 40\%$ polydispersed) [16], the film forms a fully covered bi-layer from homogeneous monolayer via an intermediate "hash" phase (a morphology full of crisscross inhomogeneous stripes of higher density at characteristic angles relative to the compression direction), followed by the formation of wrinkles and folds from the homogeneous bi-layer. The hash phase was identified with AFM to be a coexistent phase of monolayer and bi-layer phases before the film completes its bi-layer surface coverage. However, the mechanism of the bilayer formation was not clear. In the case of much more monodispersed (8% in size distribution) 6 nm Au nanoparticles,19 the film evolves from homogeneous monolayer into homogeneous tri-layer at higher surface pressures through an intermediate phase with similar morphology of hash-like strips. Both X-ray scattering and AFM results suggested that Au nanoparticle monolayer and trilayer coexist

at hash phase. Due to the lack of evidence of Au nanoparticle bilayer existing in the hash phase, a mechanism of S-folding (monolayer folds sideways) was proposed (Fig 7.1 left). However, because the formations of hash lines are dynamical, the conventional X-ray Reflectivity (XR) may be too slow to adequately capture the details of this rapidly evolving intermediate phase, the fundamental mechanism for the morphological phase transition as a function of increasing surface pressure is still not well understood.

Figure 7.1: The trilayer folding morphologies discussed in the text: left, S-fold of width w; right, crinkle fold.

A recently developed liquid surface scattering technique, known as Grazing Incidence X-ray Off-Specular scattering (GIXOS), has been shown to be an attractive alternative to conventional XR [24, 25, 26, 27]. Compared to conventional XR, GIXOS provides much faster temporal resolution. This allows us to probe non-equilibrium compression phases which can only be observed during a continuous Langmuir film compression and are not observed under steady-state conditions. Moreover, in grazing incidence geometry, x-rays sample a large and constant area of the film, as opposed to XR measurements during which the footprint of the X-ray beam varies continuously. High surface roughness of a typical nanoparticle film severely limits the range of the XR measurements, but surface roughness is not a major limitation of GIXOS measurements. Additionally, due to the large beam footprint (typically 10 *cm* lengthwise), GIXOS measurements are less sensitive to both lateral film inhomogeneity and radiation damage. In an XR measurement these effects are more prominent, since the X-ray footprint on the film varies from about 2 *cm* to about 0.1 *cm* lengthwise during the entire measurement due the changes in the incident angle of the X-ray beam. These salient features make GIXOS an ideal technique for capturing the transient structures in the intermediate "hash" phase.

We have previously reported [28] the first study comparing XR and GIXOS

measurements on the same samples. We demonstrated that properly accounting for the contributions of thermal capillary wave fluctuations and instrumental resolution effects allows for the quantitative analysis of GIXOS measurements that can provide Angstrom-resolution details of the surface-normal electron density profile. The results obtained from such GIXOS data analysis are comparable to those obtained from XR measurements [28].

Here we report the results of applying GIXOS to study the rapid structural phase evolution of self-assembled Au nanoparticle films as the films are being continuously compressed. With GIXOS technique, we observed that, upon compression, the Au nanoparticle monolayer first forms a non-equilibrium, partially-covered second layer on top of the homogeneous first layer, before entering its trilayer phase under further compression. Our studies reveal the existence of a transient bilayer phase in the hash phase that leads to a new buckling mechanism - individual-nanoparticle-level crinkling (Fig 7.1 right) - instead of our previously suggested "S-folding" mechanism (Fig 7.1 left), which cannot account for bilayer phase formation.

7.2 Experiments and Data Analysis

The x-ray scattering experiments were performed at the ChemMatCARS 15-ID beamline [29] at the Argonne National Laboratory, Advanced Photon Source (APS), using monochromatic x-rays with wavelength of 1.24 $\mathring{A}$. The GIXOS experimental geometry is illustrated schematically in Fig 7.2. The x-ray beam incidence angle ($\alpha = 0.1^{\circ}$) was set below the critical angle for total external reflection, thus rendering the scattering from the bulk water substrate negligible (see Fig 7.2 inset). The scattering patterns were collected in a fixed geometry for a wide range of out-of-plane angles β (0° to 7.3°), corresponding to surface-normal wavevector transfer component q_z ranging from -0.055 $\mathring{A}^{-1}$ to 0.647 $\mathring{A}^{-1}$, for an azimuthal angle $\theta = 0.4^{\circ}$, with a two-dimensional hybrid pixel array x-ray detector, Pixel Apparatus for the Swiss Light Source (PILATUS 100K) [30] operating in single-photon counting mode. The detector was located 977 mm downstream from the

sample. Two sets of guard slits were used, one 300 mm downstream from the sample and the other directly in front of the PILATUS to reduce the small-angle scattering from the specular reflection of the surface, as well as the background scattering from the upstream Kapton window of the Langmuir trough. Details of the GIXOS measurement setup and the background measurement were described in our previous paper [28]. A typical original GIXOS data from an Au nanoparticle Langmuir film is shown as the red curve in Fig 7.2. All the data shown in the data analysis part are net scattering from the samples, with their background subtracted.

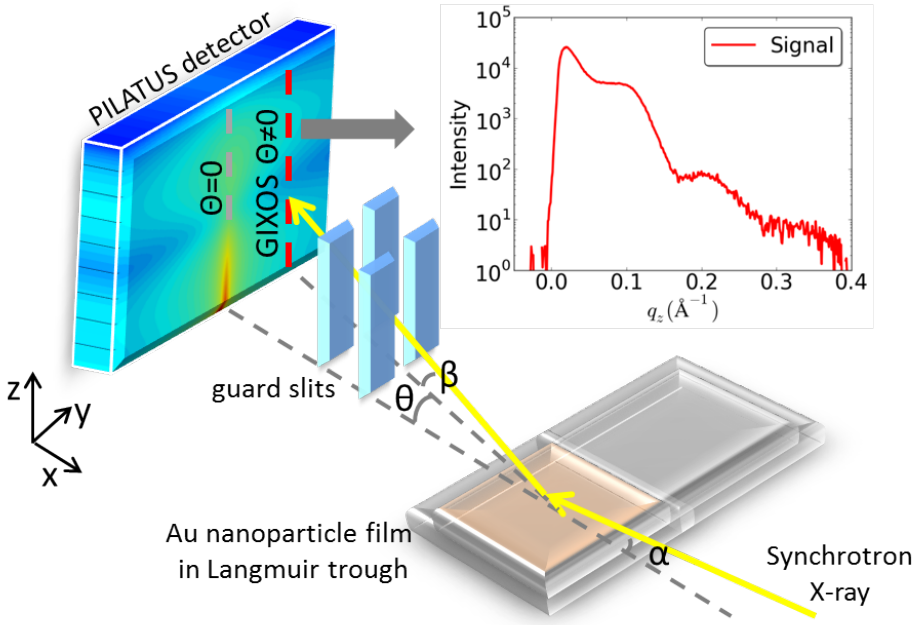

Figure 7.2: Schematic view of the scattering geometry with the Langmuir trough. An x-ray beam is incident at the liquid-air interface at grazing incidence α. Off-specular scattering is detected by PILATUS area detector simultaneously for a wide range of β at a specific azimuthal angle θ, along the trajectory indicated with red dashed line. An inset shows a typical intensity profile from an Au nanoparticle monolayer film (red curve), plotted as function of wavevector transfer normal to the surface, q_z.

We spread a solution of diameter $d \sim 5.5\ nm$ thiolated Au nanoparticles (Ocean Nanotech) in chloroform onto the ultra-pure water surface in a Langmuir

trough to form a self-assembled monolayers; the sizes of the Au cores and the dodecanethiol ligands of the NPs are roughly 5 nm and 1 nm, respectively. Observed under an optical microscope, the resulting monolayer film was reasonably isotropic and homogeneous across the entire sample.19 The monolayer was then compressed with a motorized barrier at a rate of 6 cm^2/min from a surface area of 343.5 cm^2 corresponding to initial surface pressure of 0 mN/m, with surface pressure monitored in situ by a Wilhelmy plate. A minimum surface area of 60 cm^2 was set by the instrumental setup of the scattering. The structure evolution of the nanoparticle film during the compression was discussed as a function of surface area instead of as a function of time. A series of GIXOS data, as shown in Fig 7.3 A, were measured consecutively as the film was being compressed and the exposure time for each GIXOS dataset was 30 seconds long. The full compression process took about half an hour to complete. Typical timescales during which the Au nanoparticle film was noticeably damaged by x-ray radiation was on the order of 5 minutes. However, the barrier was constantly shifting a fresh area of the Au nanoparticle film into the fixed x-ray illumination area (0.3 mm wide) during the GIXOS measurements, and therefore, beam damage of the sample was negligible.

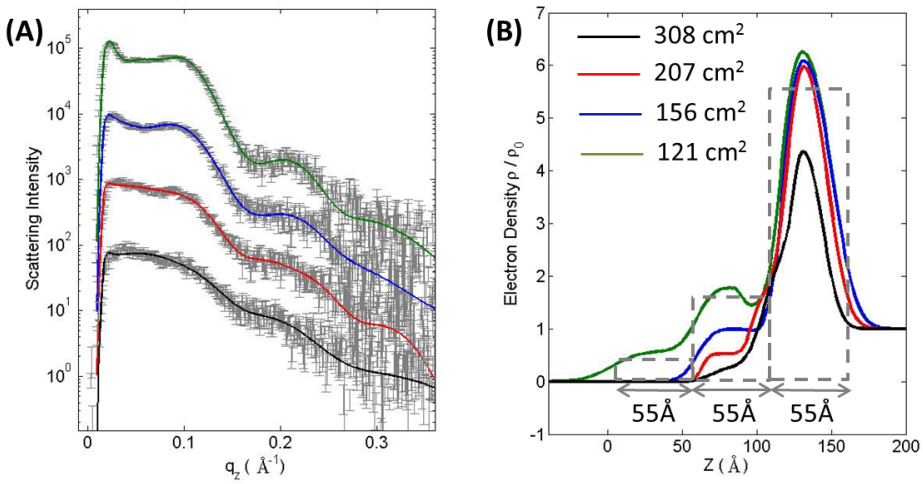

Figure 7.3: A: Fits of GIXOS data from Au nanoparticle film taken at different surface pressures during the compression. The data and fits for 207, 156, 121 cm^2 were vertically offset by factors of 10, 100, 1000 for clarity. B: the extracted corresponding electron density profiles.

The GIXOS data were analyzed using the Born Approximation as described by us previously [28] to obtain the electron density profiles of the Au nanoparticle film along the surface-normal of the film. As can be seen in Fig 7.3 A, the raw GIXOS data exhibit substantial changes upon compression. In order to extract real-space structural information of the Au nanoparticle self-assembled films normal to its surface, the GIXOS data at different compression stages (i.e. different surface pressures) were fitted to the following expression, utilizing the known differential cross section for scattering off liquid surfaces:

$$\frac{I}{I_0} = \frac{1}{A_0}\int_{res}\frac{d\sigma}{d\Omega}d\Omega = \frac{1}{k^2\sin\alpha\sin\beta}(\frac{q_c}{2q_z})^4\frac{\eta {q_z}^2}{8\pi}|\Phi(q_z)|^2|t^{in}|^2|t^{sc}|^2\int_{res}\frac{1}{{\mathbf{q}_{xy}}^2}(\frac{\mathbf{q}_{xy}}{q_{max}})^{\eta}d^2\mathbf{q}_{xy} \tag{7.1}$$

where $k = 2\pi/\lambda$ is magnitude of the wavevector, $I = I(q_z)$ is the intensity measured at given wavevector transfer q_z, I_0 and A_0 are the intensity and the illumination area of the incident x-ray beam, q_c and q_{max} are the critical wavevector and upper wavevector cutoff, while t^{in} and t^{sc} are the Fresnel transmission coefficients between air and water, t^{sc} is responsible for the low angle scattering peak (the so-called Yoneda peak). The structure factor $|\Phi(q_z)|^2$ is defined by the in-plane average of the intrinsic electron ρ density along the surface normal. The function $\eta = k_B T q_z^2/2\pi\gamma$ provides a measure of the magnitude of smearing due to thermally induced capillary waves, here γ is the surface tension of the sample (measured in-situ by a Wilhelmy plate). As shown in Eq 7.1, the intensity measured at a specific scattering vector is obtained by integrating the differential cross-section over a solid angle defined by the detector resolution. Moreover, once the integral is simplified, the detector resolution dependent integration is over a capillary smearing dependent expression.

With thermal capillary smearing and resolution function effects carefully taken into account [28], the extracted electron density profiles (see Fig 7.3 B) are the intrinsic layered structural property of the Au nanoparticle film normal to the film, independent of experimental details such as the detector resolution or the temperature [31, 32]. Note that the electron density ρ obtained here is the averaged result over the area of the nanoparticle film within the x-ray illumination

area and is normalized to the electron density of water ρ_0, with air phase ($\rho = 0$) on the left side and water phase ($\rho = 1$) on the right side in Fig 7.3 B.

In order to further confirm the quantitative viability of the GIXOS analysis, we calculated the total electron density per unit area, averaged over the X-ray illumination area, by integrating the extracted electron density along the surface-normal z and plotted it as a function of $1/area$. Due to the conservation of the total number of Au nanoparticles at the water-air interface, the total surface-normal-integrated electron density per unit area (ρ/A) of the Au nanoparticle film should be inversely proportional to the surface area. As shown in Fig 7.4, the total surface-normal-integrated electron density vs. $1/surfacearea$ plot follows a straight line (dashed line in Fig 7.4). The deviation of the electron density from the line is possibly caused by the density inhomogeneity in the film due to local multilayer islands vs. monolayer coverage at large surface area (low $1/area$).

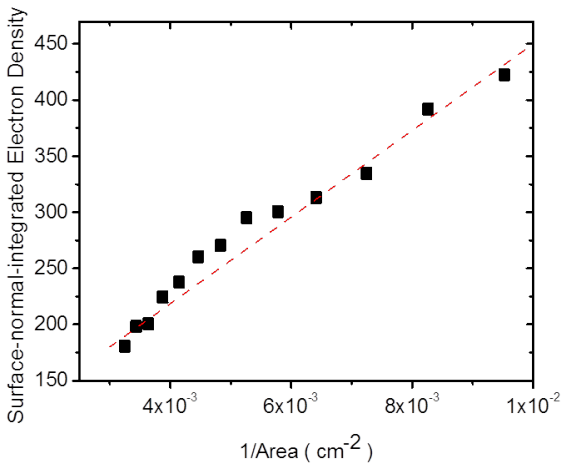

Figure 7.4: The measured surface-normal-integrated electron density vs. 1/surface area (solid points). The dotted line represents the expected electron density due to the conservation of the number of Au nanoparticles.

7.3 Results and Discussion

Fig 7.5 shows the isotherm of the Au nanoparticle film taken during the GIXOS measurements (the GIXOS measurements stopped at surface area of 100 cm^2

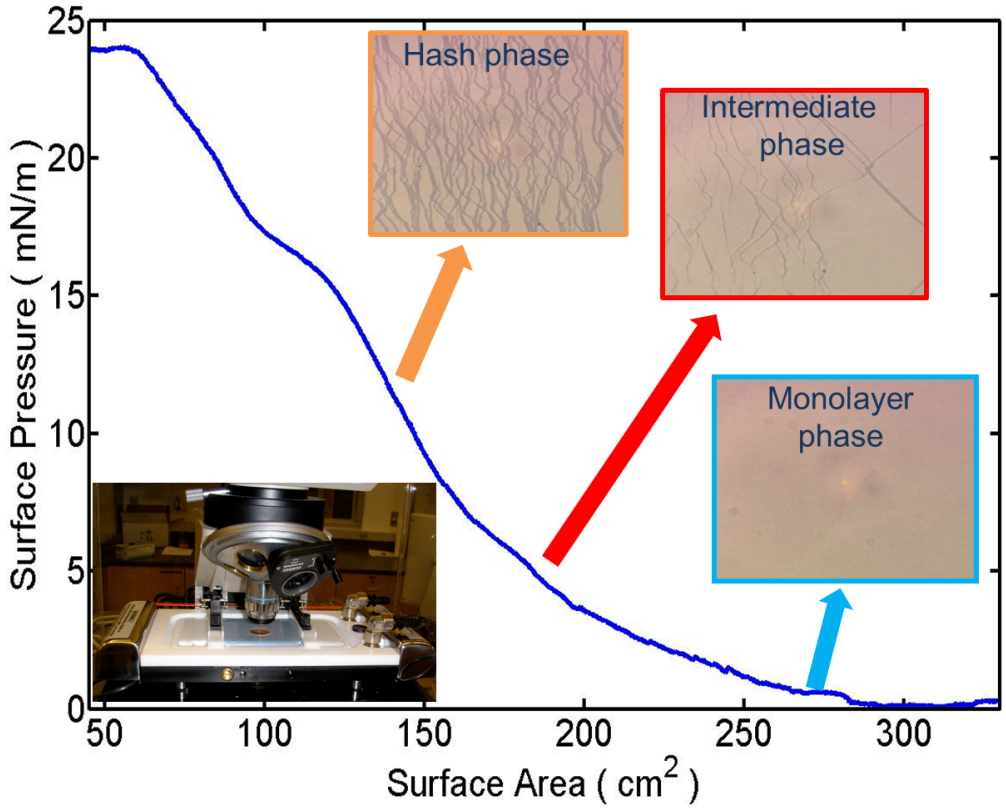

Figure 7.5: An isotherm of Au nanoparticle film and optical microscopy images (insets) of the pure monolayer phase, intermediate phase and hash phase.

when the trough barrier blocked the X-ray incident beam). Even though exact values of the transition points along the isotherm may vary slightly from sample to sample due to size variation between different batches of the Au nanoparticles and the inhomogeneity of the Au nanoparticle films, the general features of the isotherms measured for different films are similar qualitatively.

In our previous studies using optical microscopy, AFM and conventional X-ray Reflectivity (XR), we found that Au nanoparticles formed islands of monolayer before the surface pressure lifted off (around surface area of $\sim 280\ cm^2$ in Fig 7.5), and the islands gradually merged into a homogeneous monolayer as the surface area was reduced. The transition between homogeneous monolayer and the hash phase, though, was not clearly correlated to the changes on the isotherm; patches of hashes would locally emerge at different location across the sample. Because of

the dynamic nature in this inhomogeneity region, XR measurements were somewhat inconsistent. However, those XR measurements indicate an inhomogeneous trilayer structure at this stage [33]. The hash phase was fully developed only when the surface pressure was near the transition point (surface area of $\sim 120\ cm^2$ in Fig 7.5). While XR measurements still show an inhomogeneous trilayer structure at this stage, the AFM measurements show a coexisting phase between monolayer patches and trilayer ones [16, 33]. Above the transition point, the morphology of the film became uniform again but the film color was darker than that of the monolayer phase, and both AFM and XR confirmed a uniform trilayer film structure. Due to lack of the observation of a bilayer film structure in the previous experiments, we speculated that the Au nanoparticle monolayer S-folded into a trilayer, much like how a piece of carpet would fold over when pushed sideways (as shown in Fig 7.1 left). Nevertheless, a question remains about this folding mechanism. It appears kinetically costly for the nanoparticle monolayer to S-fold extensively since it requires two adjacent layers to slide/shear over each other as the S-folding expands, much like sliding/shearing two pieces of Velcro fasteners along their adhesive surfaces. In addition, the S-fold mechanism does not apply to the bilayer folding observed in smaller or more polydispersed Ag and Au nanoparticle films, implying that multiple folding mechanisms exist for seemingly similar nanoparticle films.

The results from this work present a drastic different folding sequence, and, thereby, a new paradigm of folding. Using GIXOS, we are able to follow the kinetics of the Au nanoparticle ($d \sim 5.5\ nm$) monolayer folding sequence in this transitional phase when the hash patches have just appeared. In Fig 7.3 B, we show the progression of the extracted electron density profile exhibiting the layered structure of the Au nanoparticle film as the film was continuously compressed. The progression of the electron density profile illustrates an entirely different but more kinetically plausible folding mechanism (shown schematically in Fig 7.6 B) compared to the S-folding mechanism described above - upon compression the Au nanoparticle film first closes up the voids between self-assembled monolayer islands to form a "close-packed" homogeneous monolayer, then some individual particles

at weakly-interacting areas of the monolayer (possibly related to the island boundaries, self-assembly defects, or film inhomogeneity due to the polydispersity of the particle size) are pushed up into the surface-normal direction z to form double-layer islands and then tri-layer islands upon further compression. In response to the lateral stress, the film continuously evolves from partial monolayer first to a homogeneous monolayer, then a partially covered bilayer, followed by a partial tri-layer and finally to a homogeneous trilayer (not shown with GIXOS data) after the trilayer islands finish expansion over the entire film. Each layer is roughly one Au nanoparticle-size thick (55 $\mathring{A}$), as marked on Fig 7.3 B,indicating that the binding of this stabilizer to the nanoparticle is sufficiently strong that the ligands are not is not depleted at the contact between two nanoparticles. Instead, the spacing between the nanoparticles indicates that the nanoparticle surfaces remain separated by about the length of the thiol chains, agreed with our earlier measurements. The electron density of the bottom layer, is much higher than that of the middle layer and the top layer, suggesting that the bilayer or trilayer forms only locally (partial coverage), consistent with crisscross morphology of the hash phase, as shown in the optical microscopy images in Fig 7.5. The area coverage of bi-layer/trilayer islands can be obtained from the ratio of electron density of first (bottom) layer peak and second/third layer peak.

The evolution of the layered structure manifests itself in the dependence of the total film thickness, h, and the peak value of electron density for each layer as a function of the surface area shown in Fig 7.6, all extracted from Fig 7.3 B. The thickness variation falls into three distinct regimes along the isotherm with average film thickness values of 63.0 ± 1.0 $\mathring{A}$, 108.9 ± 4.1 $\mathring{A}$ and 167.0 ± 1.0 $\mathring{A}$, respectively. These values agree well with the expected close-packing values for a layer thickness h of a monolayer, a bilayer and a trilayer of spheres of diameter of d: $h = d * [1 + \sqrt{6/3}(n-1)]$, where $d \sim 5.5$ nm and n is the layer number.

With the new result from this work that the larger monodisperse Au nanoparticle ($d \sim 5.5$ nm) monolayer first buckles into an transient bilayer phase before forming a stable trilayer phase (Fig 7.6 A), as well as the previous results that smaller and rather polydisperse Au and Ag nanoparticle films fold into stable

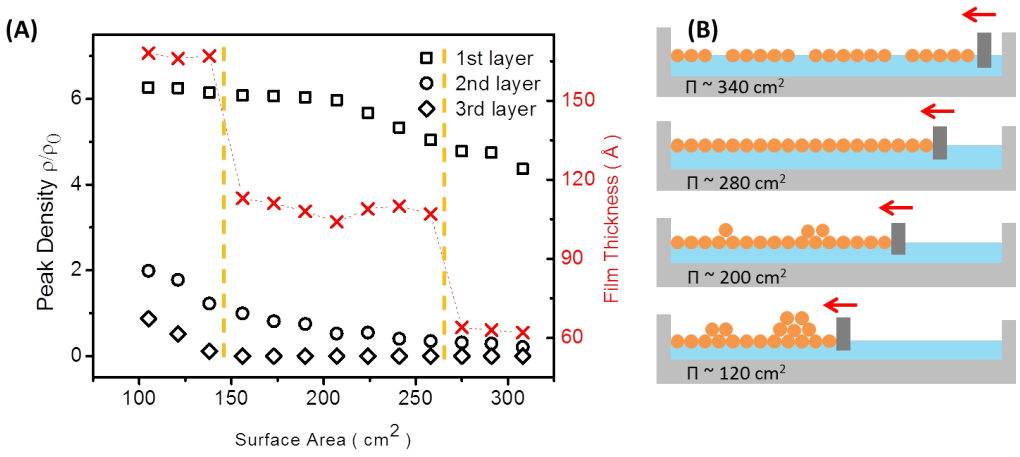

Figure 7.6: Red crosses: extracted total film thickness (right axis) vs. surface area. Black symbols: extracted peak value of electron density (left axis) for each layer vs. surface area. The vertical lines are guides to the eyes, separating the distinct transitions in the film thickness from monolayer to bilayer and bilayer to trilayer morphology. B: The schematic of different evolution stages of the Au nanoparticle film.

bilayers, we propose a new folding scheme, illustrated in Fig 7.7, for all three nanoparticle monolayers mentioned here. Upon buckling, these nanoparticle films crinkle locally on a characteristic length scales comparable to the particle size. The local particle crinkling forces nanoparticles to enter the third dimension; this can be considered as the nucleation of a bilayer (Fig 7.7 step 1). Bilayer islands can be expanded via nucleating more bilayer units nearby or folding bilayer units over onto the original monolayer to form trilayer islands (i.e. Fig 7.7 steps 2-8). This process is accomplished without nanoparticle shearing in the x-y plane. The trilayer configuration is more energetically-favorable, since it allows more particle-particle contacts than in a monolayer or bi-layer. Conversely, for the polydispersed smaller nanoparticle monolayer, the nucleation of bilayer islands is more plausible due to the weaker bonding between particles with different size. Thus, the nanoparticle monolayers fold via creating more and more bilayer islands across the entire surface before the film reaches its uniform bilayer state.

Our justification of the crinkling mechanism is based on a kinetic model for the buckling motions required. In contrast to continuum pictures of monolayer

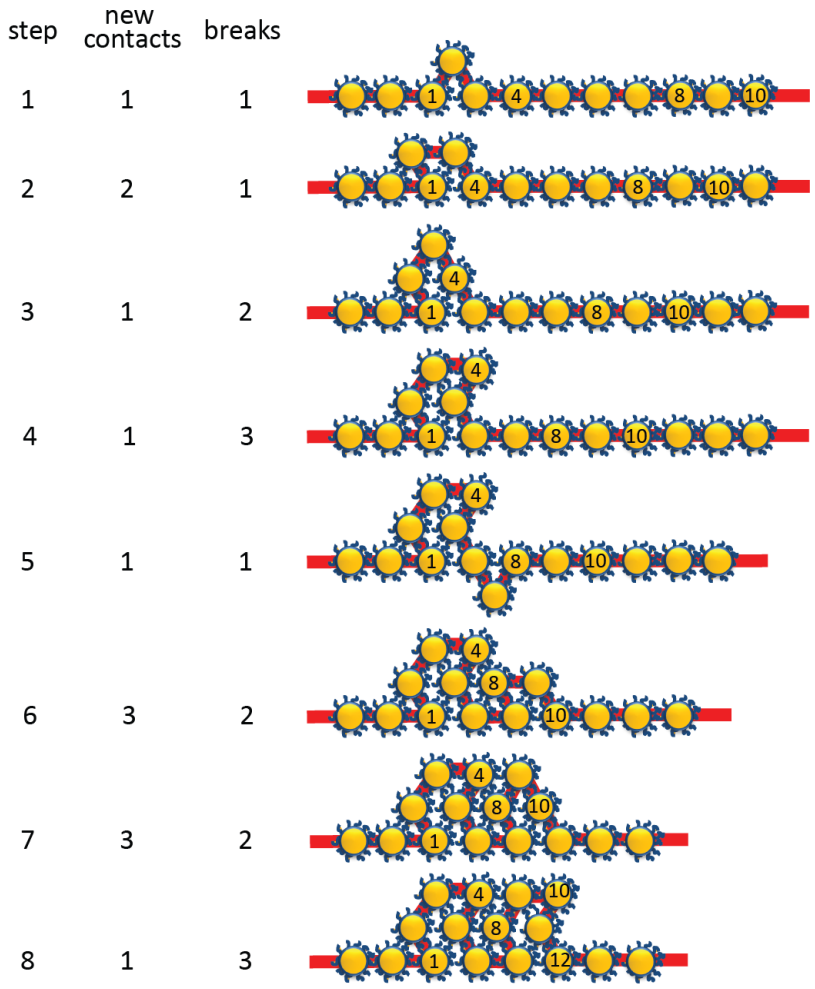

Figure 7.7: Steps in a hypothetical crinkle-folding mechanism. Row 1: monolayer viewed in cross section after one buckling event. Horizontal direction is the compression direction; vertical direction is the normal to the liquid surface. Particles 1, 4, 8, 10 and 12 along the monolayer are labeled. Rows 2-8: subsequent steps in the trilayer formation. Colored stripe follows the original sequence of particles in the monolayer. Columns at left indicate the number of new particle-particle contacts formed in the step and total number of contacts that must be broken or weakened to make the step move, including interfacial contacts. Further folding after step 78 proceeds as in step 5.

folding we view the particle junctions as freely-sliding links with no associated bending energy [19]. The entire interaction is a short-range attraction u between each pair of adjacent particles. In addition, we assume a weaker attraction v owing to the attraction of particles to the water subphase. The surface pressure

adds an external energy proportional to the compression of the layer. We denote this external energy to move one particle width as s. For simplicity we initially view the monolayer as a simple line of particles in two dimensions. The transition between a monolayer and an incipient bilayer fold (Fig 7.7 step 1) results in a new particle-particle contact and a compression by one particle width. In Fig 7.7 step 1, particle 3 has gained a new particle-particle contact (with particle 1). However, particle 2 has lost one particle-water contact. Thus the change in free energy is $-u - s + v$. For sufficiently large s, the move is clearly favorable. However, since the buckling is observed to occur by nucleation, the passage from the monolayer to the buckled state must impose an activation barrier, in which the water energy v is lost but the inter-particle energy u has not been gained. We denote this activation energy as b. It is this barrier that determines the rate of nucleation of bilayer folds. Once the initial fold has formed (particles 1, 2 and 3 in Fig 7.7), further processes to lower the energy are possible. In step 2, particle 2 moves a step to the left, carrying particles 3 and 4 with it, particle 1 and 2 gain one additional contact (0-2, 1-4) while particle 3 loses its contact with water. The net energy gain is $2u - s + v$. As before, the sliding motion involves states of incomplete particle contact, so we also expect an activation energy for this motion as well as for the initial bilayer buckling. We suppose that the energy cost of an incomplete or "broken" contact to be a fraction α of the contact energy u. This contact breaking energy is experienced by all the particles that must slide over others. With n sliding particles, the energy cost is proportional to n. Evidently this cost favors moves involving only a small number of particles. The cost for the sliding move of particles 2 and 3 is $(u + b)$, since particle 3 loses a water contact and a contact with particle 1.

Further moves of this sort can enable trilayer formation without large activation barriers. One scenario is illustrated in steps 3-8 of Fig 7.7. Each of the steps in this scenario results in a compression by one particle width, and thus gives a gain s in free energy. Moreover each step increases the number of particle contacts, giving a gain in the contact energy u. All of the steps require some sliding and thus some contact breaking energy. No contact from the original monolayer is broken.

All steps but step 4 have fewer than three broken contacts, including interfacial contacts. The tally of added contacts and transiently broken contacts is listed in the figure next to each step.

It is clear from this crude picture that the kinetically-favored morphology may change if these parts of the energy are altered. For example, if the cost of breaking a contact is increased, trilayer formation is suppressed in favor of bilayers. Clearly the actual kinetics is more complicated than this model describes. It is meant only to justify the plausibility of the formation of trilayers by the "crinkling" moves of Fig 7.7.

The trilayer phase is the bulk state in which particles need to overcome higher kinetic barriers to move relatively to each other. Expanding the trilayer islands is more energetically favorable than raising particles up to the 4th layer. For example, further crinkling in Fig 7.7 after step 8 proceeds as in step 5, instead of proceeding to any 4-layer configuration. Once the film forms a fully-covered trilayer, pushing any particle up to the 4th layer would cost very high energy since it involves shearing/sliding moves of many particles that significantly increase the kinetic barriers. Thus the transition from a trilayer to 4-layer is suppressed. The film can only be bended as a continuous thick film which is consistent to our observation of macroscopic folds under further compression.

The layer number of the stable state depends on the properties of nanoparticles and the interactions between them. In general, the Van de Waals interaction between two nanoparticles with larger size is stronger than that between smaller ones and two same size particles have stronger bonding than two different size ones with similar average size [34, 35, 36]. In addition, monodispersity is an important requirement for forming high quality single crystal grains [34]. Therefore, the monodispersed larger Au nanoparticles used in this work form a monolayer of well-ordered close-packing crystallites with long range positional orders, determined by Grazing Incident X-ray diffraction (GIXD) [16, 33], whereas monolayers of Ag nanoparticles and the smaller Au nanoparticles appeared to form a jammed liquid, showing no long range order under GIXD. Thus, in the case of monodispersed Au nanoparticle monolayers with long range order, the local nanoparticle-level crin-

kling is more kinetically favorable at relative weakly-interacting areas, such as near crystalline defects or "single-crystal" grain boundaries, as the single-crystal grains preserve their ordered structures.

7.4 Conclusion

The newly developed GIXOS technique facilitates the study of the rapid evolution (tens of seconds) and inhomogeneous buckling of Langmuir monolayers of Au nanoparticles under lateral compression. With GIXOSs capability of taking snapshots of rapidly evolving systems, we are able to obtain a more consistent nanoscopic picture of the film structure, which provides insights into the fundamental folding mechanisms of ultrathin self-assembled nanoparticle films under compression. Our results show the formation of a double-layer, in the transition region where hash patches first appear locally after the monolayer of Au nanoparticle reaches full coverage and before it proceeds to form a third layer. Our observation of the transient double-layer phase implies a nanoparticle-level crinkling mechanism of the nanoparticle film folding phenomena. The crinkling model also holds promise to explain the oblique angles of the folding leading to the oblique stripes seen in the hash phase. The events shown in Fig 7.7 would in general involve transverse displacements out of the plane of the figure, in order to maximize particle-particle contact. These transverse displacements may favor oblique folding. This picture can be extended to shed light into the understanding of other molecular film buckling/folding and lipid membrane collapsing phenomena which develop on short time scales and usually contain inhomogeneity.

7.5 Acknowledgements

The text of this chapter, in part, is a reprint of the material as it appears in:

Y. Dai, B. Lin, M. Meron, K. Kim, B. D. Leahy and O. G. Shpyrko, "Synchrotron X-ray studies of Rapidly Evolving Morphology of Self-assembled Nanopar-

ticle Films under Stress", submitted to *Langmuir*, 2013.

Bibliography

[1] Wenlong Cheng, Michael J. Campolongo, Judy J. Cha, Shawn J. Tan, Christopher C. Umbach, David A. Muller, and Dan Luo. Free-standing nanoparticle superlattice sheets controlled by DNA. *Nature Materials*, 8(6):519–525, June 2009.

[2] Angang Dong, Jun Chen, Patrick M. Vora, James M. Kikkawa, and Christopher B. Murray. Binary nanocrystal superlattice membranes self-assembled at the liquid-air interface. *Nature*, 466(7305):474–477, July 2010.

[3] Andrea Tao, Prasert Sinsermsuksakul, and Peidong Yang. Tunable plasmonic lattices of silver nanocrystals. *Nature Nanotechnology*, 2(7):435–440, July 2007.

[4] Alexander Bker, Jinbo He, Todd Emrick, and Thomas P. Russell. Self-assembly of nanoparticles at interfaces. *Soft Matter*, 3(10):1231–1248, September 2007.

[5] Siddique J. Khan, F. Pierce, C. M. Sorensen, and A. Chakrabarti. Self-assembly of ligated gold nanoparticles: Phenomenological modeling and computer simulations. *Langmuir*, 25(24):13861–13868, December 2009.

[6] Sachin Kinge, Mercedes Crego-Calama, and David N. Reinhoudt. Self-assembling nanoparticles at surfaces and interfaces. *ChemPhysChem*, 9(1):2042, 2008.

[7] Jinbo He, Pongsakorn Kanjanaboos, N. Laszlo Frazer, Adam Weis, Xiao-Min Lin, and Heinrich M. Jaeger. Fabrication and mechanical properties of large-scale freestanding nanoparticle membranes. *Small*, 6(13):14491456, 2010.

[8] Don Keun Lee, Young Hwan Kim, Chang Woo Kim, Hyun Gil Cha, and Young Soo Kang. Vast magnetic monolayer film with surfactant-stabilized Fe3O4 nanoparticles using langmuir-blodgett technique. *The journal of physical chemistry. B*, 111(31):9288–9293, August 2007. PMID: 17636981.

[9] S. Paul, C. Pearson, A. Molloy, M. A. Cousins, M. Green, S. Kolliopoulou, P. Dimitrakis, P. Normand, D. Tsoukalas, and M. C. Petty. LangmuirBlodgett

film deposition of metallic nanoparticles and their application to electronic memory structures. *Nano Letters*, 3(4):533–536, April 2003.

[10] Suresh Narayanan, Jin Wang, and Xiao-Min Lin. Dynamical self-assembly of nanocrystal superlattices during colloidal droplet evaporation by in situ small angle x-ray scattering. *Physical Review Letters*, 93(13):135503, September 2004.

[11] Luka Pocivavsek, Robert Dellsy, Andrew Kern, Sebastian Johnson, Binhua Lin, Ka Yee C. Lee, and Enrique Cerda. Stress and fold localization in thin elastic membranes. *Science*, 320(5878):912–916, May 2008.

[12] Ka Yee C. Lee. Collapse mechanisms of langmuir monolayers. *Annual Review of Physical Chemistry*, 59(1):771–791, 2008. PMID: 18393683.

[13] D. Vella, P. Aussillous, and L. Mahadevan. Elasticity of an interfacial particle raft. *EPL (Europhysics Letters)*, 68(2):212, October 2004.

[14] Christophe Ybert, Weixing Lu, Gunter Mller, and Charles M. Knobler. Collapse of a monolayer by three mechanisms. *The Journal of Physical Chemistry B*, 106(8):2004–2008, February 2002.

[15] S. T. Milner, J. F. Joanny, and P. Pincus. Buckling of langmuir monolayers. *EPL (Europhysics Letters)*, 9(5):495, July 1989.

[16] Kyungil Kim, Brian D Leahy, Yeling Dai, Oleg Shpyrko, Janet S Soltau, Matthew Pelton, Mati Meron, and Binhua Lin. Governing factors in stress response of nanoparticle films on water surface. *Journal of Applied Physics*, 110(10):102218–102218–7, November 2011.

[17] K. Vegso, P. Siffalovic, M. Jergel, M. Weis, M. Benkovicova, E. Majkova, S. Luby, T. Kocsis, and I. Capek. Silver nanoparticle monolayer-to-bilayer transition at the Air/Water interface as studied by the GISAXS technique: Application of a new paracrystal model. *Langmuir*, 28(25):9395–9404, June 2012.

[18] Sarathi Kundu. Layer-by-layer assembly of thiol-capped au nanoparticles on a water surface and their deposition on h-terminated si(001) by the Langmuir-Blodgett method. *Langmuir*, 27(7):3930–3936, April 2011.

[19] Brian D. Leahy, Luka Pocivavsek, Mati Meron, Kin Lok Lam, Desiree Salas, P. James Viccaro, Ka Yee C. Lee, and Binhua Lin. Geometric stability and elastic response of a supported nanoparticle film. *Physical Review Letters*, 105(5):058301, July 2010.

[20] James R. Heath, Charles M. Knobler, and Daniel V. Leff. Pressure/Temperature phase diagrams and superlattices of organically functionalized metal nanocrystal monolayers: the influence of particle size, size distribution, and surface passivant. *The Journal of Physical Chemistry B*, 101(2):189–197, January 1997.

[21] Stephan Kubowicz, Markus A. Hartmann, Jean Daillant, Milan K. Sanyal, Ved V. Agrawal, Christian Blot, Oleg Konovalov, and Helmuth Mohwald. Gold nanoparticles at the LiquidLiquid interface: X-ray study and monte carlo simulation. *Langmuir*, 25(2):952–958, January 2009.

[22] J. Daillant C. Gourier. Bending energy of amphiphilic films at the nanometer scale. *Physical Review Letters*, 78(16):31573160, 1997.

[23] M. K. Sanyal M. K. Bera. Reversible buckling in monolayer of gold nanoparticles on water surface. *EPL (Europhysics Letters)*, 78(5):56003, 2007.

[24] Robert Dalgliesh. Application of off-specular scattering of x-rays and neutrons to the study of soft matter. *Current Opinion in Colloid & Interface Science*, 7(3-4):244–248, 2002.

[25] Sen M. O'Flaherty, Lutz Wiegart, Oleg Konovalov, and Bernd Struth. Observation of zinc phthalocyanine aggregates on a water surface using grazing incidence x-ray scattering. *Langmuir*, 21(24):11161–11166, November 2005.

[26] L. Wiegart, S. M. O'Flaherty, P. Terech, and B. Struth. Observation of the desorption of mineral nanoparticles from a hybrid langmuir monolayer: an in situ grazing incidence x-ray (GIXOS) study. *Soft Matter*, 2(1):54, 2006.

[27] Jean Daillant, Jeremy Pignat, Sophie Cantin, Francoise Perrot, Serge Mora, and Oleg Konovalov. Elasticity of two-dimensional crystalline monolayers of fatty acid salts at an air-water surface. *Soft Matter*, 5(1):203–207, 2009.

[28] Yeling Dai, Binhua Lin, Mati Meron, Kyungil Kim, Brian Leahy, and Oleg G. Shpyrko. A comparative study of langmuir surfactant films: Grazing incidence x-ray off-specular scattering vs. x-ray specular reflectivity. *Journal of Applied Physics*, 110(10):102213, 2011.

[29] The liquid surface/interface spectrometer at chemmatcars synchrotron facility at the advanced photon source. *Physica B: Condensed Matter*, 336(12):75 – 80, 2003. ¡ce:title¿Proceedings of the Seventh International Conference on Surface X-ray and Neutron Scattering¡/ce:title¿.

[30] M. Meron, J. Gebhardt, H. Brewer, J. P. Viccaro, and B. Lin. Following transient phases at the air/water interface. *The European Physical Journal Special Topics*, 167(1):137–142, 2009.

[31] Oleg Shpyrko, Patrick Huber, Alexei Grigoriev, Peter Pershan, Ben Ocko, Holger Tostmann, and Moshe Deutsch. X-ray study of the liquid potassium surface:structure and capillary wave excitations. *Physical Review B*, 67(11):115405, March 2003.

[32] P. S. Pershan. X-ray scattering from liquid surfaces: Effect of resolution. *The Journal of Physical Chemistry B*, 113(12):3639–3646, March 2009.

[33] David G. Schultz, Xiao-Min Lin, Dongxu Li, Jeff Gebhardt, Mati Meron, James Viccaro, and Binhua Lin. Structure, wrinkling, and reversibility of langmuir monolayers of gold nanoparticles. *J. Phys. Chem. B*, 110(48):24522–24529, 2006.

[34] W. B. Russel, D. A. Saville, and W. R. Schowalter. *Colloidal Dispersions*. Cambridge University Press, March 1992.

[35] Thomas A. Witten. *Structured Fluids: Polymers, Colloids, Surfactants*. OUP Oxford, January 2010.

[36] Jacob N Israelachvili. *Intermolecular and surface forces*. Academic Press, Burlington, MA, 2011.

8 Conclusions

In this thesis, the structural and dynamical properties of rapidly evolving nanoscale interfacial systems have been studied, mainly by x-ray scattering techniques, including x-ray photon correlation spectroscopy (XPCS), x-ray reflectivity (XRR) and grazing incidence x-ray scattering (GISAXS and GIXOS).

In chapter 3, We have investigated the capillary dynamics of molten polymer films laterally confined within narrow (140 nm to 300 μm) channels using XPCS. We discovered three distinct regimes of the surface dynamics behavior for the confined polymer surfaces. First, when the channel width is smaller than ~ 30 μm, the surface capillary dynamics are completely suppressed within our accessible length range. Second, when the channel width is larger than 150 μm, the surface dynamics is indistinguishable from that of a thin film. Third, if the polymer is confined in the channels of width between 50 μm and 150 μm, the surface dynamics exhibit a strong confinement-size dependence. The surface capillary fluctuations at polymer surface are found to be slower in the narrower channels. In addition to the size dependence, we found that the measured surface capillary dynamics is dramatically different in the two orthogonal direction relative to the long axis of channels implying an anisotropic effect. These confinement effects on the surface fluctuations are discussed in context of wall-pinning and meniscus effects.

In chapter 4, We have used XPCS to investigate capillary wave dynamics of thin molten polymer films supported by nano-structured gratings, where the vertical confinement is no longer uniform. The polymer film thickness over the tops of the grating lines is only $2 - 3R_g$, which is known to significantly suppress dynamics in the flat uniform-thickness films due to viscoelastic confinement effects, while the film thickness over the channel regions is considerably thicker, roughly

130 $nm16R_g$, where confinement effects and vdW substrate interactions are negligible. We found that the surface capillary dynamics over such nanostructures exhibit directional anisotropy. Capillary wave dynamics propagating parallel to the channels are in good agreement with the simple viscous flat film model, with an effective thickness close to the film depth over the channels. However, the capillary wave dynamics across the channels are dramatically different due to the combination of the PS film curvature and confinement effects arising from the vdW interactions with the substrate and the ultrathin nature of the PS film over the tops of the silicon lines. Below a cutoff length scale ($Q < Q_c$), dynamics are nearly identical to the parallel direction dynamics; above it, the dynamics are markedly suppressed and nearly temperature independent. This cutoff length-scale is related to the crossover from surface tension dominated to vdW dominated interactions between the PS and the substrate. This value is several times the periodicity of the grating, indicating that capillary waves may propagate through ultra-thin regions of the polymer film, which has not been observed previously.

These findings reported in chapter 3 and 4 may have important impact on the study of nanoscale polymer patterned structures, on the design of nanoscale topography for template dewetting of nanoscale patterns and on the understanding of the ultrathin polymer film physics.

In chapter 5, the development of zig-zag capillary instability has been studied *in-situ* with time-resolved GISAXS. Our measurement provides the global but detailed information about the structure evolution of polymer pattern during annealing, which is complimentary to those provided by conventional local probes such as AFM. The data analysis needs to be improved for better results. It is important to extend this measurement to some smaller lengthscale structures or faster evolving systems.

In chapter 6 and 7, a young member from the family of surface scattering techniques has been explored and demonstrated to give sub-nanometer details about the out-of-plane structure that is comparable to those are obtained from conventional specular XRR measurement but with much better temporal resolution. We showed that it's crucial to take into account the resolution effect and

capillary effect for quantitative GIXOS analysis. We utilized this newly developed technique to take snapshots of the rapidly structural evolution of interfacial nanostructures, specifically, the Au nanoparticle film self-assembled at liquid-air interface. We obtained a consistent nanoscopic picture of the film structure, which provides insights into the fundamental folding mechanisms of ultrathin self-assembled nanoparticle films under compression. Our results reveal the existence of a transient bilayer phase in the transition region where hash patches first appear locally after the monolayer of Au nanoparticle reaches full coverage and before it proceeds to form a third layer. The observation of the transient double-layer phase implies a nanoparticle-level crinkling mechanism of the nanoparticle film folding phenomena. The crinkling model also holds promise to explain the oblique angles of the folding leading to the oblique stripes seen in the hash phase. This picture can be extended to shed light into the understanding of other molecular film buckling/folding and lipid membrane collapsing phenomena which develop on short time scales and usually contain inhomogeneity.